

Wing and Fuselage Structural Optimization Considering Alternative Material
Systems

By

Jonathan Lusk

B.S.A.E., University of Kansas, 2006

Submitted to the Department of Aerospace Engineering and the Faculty of the
Graduate School of the University of Kansas in partial fulfillment of the requirements
for the degree of Masters of Engineering.

Professor in Charge-Dr. Mark Ewing

Dr. Richard Hale

Dr. Stan Rolfe

Date Project Accepted

The Thesis Committee for Jonathan Lusk Certifies
that this is the approved Version of the following thesis:

Wing and Fuselage Optimization Considering Alternative Material Systems

Committee:

Professor in Charge-Dr. Mark Ewing

Dr. Richard Hale

Dr. Stan Rolfe

Date defended

Abstract

This study is a sensitivity analysis to compare weight benefits for a transport aircraft airframe from potential mechanical property enhancements of CFRP (Carbon Fiber Reinforced Plastic) Laminate and Aluminum Alloy. The computational framework is based on a simplified skin-stringer-frame/rib configuration to model the fuselage and the wings of a generic narrow and wide body jet transport. Simple (Strength of Materials) mechanics were used to predict the stresses in the skin and stringers. Strength allowables and panel buckling equations are used in conjunction with an iterative optimizer to calculate the structural airframe weight. The baseline materials include 7075-T6 Aluminum Alloy and a fictitious intermediate modulus carbon epoxy. For the CFRP material, the optimized weight results show Open Hole compression enhancement produces the most weight benefit. The Fatigue strength is the most sensitive material property for the baseline Aluminum Alloy structure. The results also indicate that the current CFRP laminate minimum gauge limits weight reduction from potential material property enhancements especially on the small jet transport.

Acknowledgements

First of all I would like to thank my academic advisor Dr. Mark Ewing for his guidance, assistance, advice, and support throughout my project. I would also like to thank Dr. Mark Ewing for teaching me the fundamentals of structural optimization and introducing me to computational resources to conduct my analysis. I'd like to thank Dr. Abdel Abusafieh and Cytec Engineering Materials for providing funding for my research and also providing me their time, information, and resources for me to carryout my analysis. I would also like to acknowledge Dr. Abdel Abusafieh for taking the time to review my documentation and results and discussing as well as enlightening me on the interest and concerns of the industry.

I'd like to thank Dr. Richard Hale for teaching me the mechanics and design of composite materials and making me aware of details that should be considered in this type of analysis. I'd like to thank Dr. Stan Rolfe for teaching me the factors that pertain to a complete fatigue analysis and for kindly participating in my examination board committee.

Table of Contents

Abstract	ii
Acknowledgements	iii
List of Figure	vii
List of Tables	xii
Nomenclature	xiv
1 Introduction	1
1.1 Objective	1
1.2 Prior Work	2
2 Methodology	4
2.1 Geometry.....	4
2.1.1 Wing	4
2.1.2 Fuselage	10
2.2 Stiffened Panel Geometry	11
2.2.1 Wing	12
2.2.2 Fuselage	15
2.3 Loads.....	18
2.3.1 Wing	18
2.3.2 Fuselage	27
2.4 Stress Analysis	33
2.4.1 Thin Walled Idealized Beam Theory (Ref 2)	33
2.4.2 Hoop and Longitudinal Stress (Ref 5)	35

2.4.3	Buckling Analysis	36
2.5	Materials	51
2.5.1	CFRP	51
2.5.2	CFRP Lamination Scheme of Aircraft Structure	52
2.5.3	Aluminum	54
2.5.4	Material Enhancement Analysis Cases	55
2.6	Failure Modes and Criteria	57
2.6.1	CFRP	57
2.6.2	Aluminum Alloy	60
2.7	Optimization	61
2.7.1	Optimized Variables	61
2.7.2	Fixed Variables	61
2.7.3	Concept of Minimum Gauge	63
2.7.4	Discretization	63
2.7.5	Optimization	70
3	Verification	78
3.1	Regression Analysis	78
3.1.1	Wing	80
3.1.2	Fuselage	83
3.2	Finite Element	86
3.2.1	Wing	86
3.2.2	Fuselage	89

4	Results and Discussion.....	92
5	Conclusions.....	109
6	Recommendations.....	110
	References.....	112
A	Appendix.....	A.1
B	Appendix.....	B.1
C	Appendix.....	C.1
D	Appendix.....	D.1

List of Figure

Figure 2.1: Wing Plan form with Kick	4
Figure 2.2: Wing Chord Distribution.....	6
Figure 2.3 Wingbox and Wing Planform.....	7
Figure 2.4: Illustration of Wingbox Thickness Taper (this in not a configuration concept illustration and there is no rib geometry displayed in this figure).....	8
Figure 2.5: Fuselage Geometry	10
Figure 2.6: "I" beam Section Stiffened Panel	12
Figure 2.7: Geometry of an "I"-Beam Section Stiffener.....	13
Figure 2.8: "Hat"-Section Stiffened Panel	15
Figure 2.9:Geometry of a Hat Stiffener	16
Figure 2.10: Generic Load Profile for 2.5g Positive Maneuver	18
Figure 2.11: Generic Load Profile for Negative 1.0g Gust.....	19
Figure 2.12: Trapezoidal Lift Distribution (1g Steady Level Flight)	20
Figure 2.13: Elliptical Lift Distribution (1g Steady Level Flight).....	20
Figure 2.14: Plot of Trapezoid and Elliptic Chord Distribution	21
Figure 2.15: Lift Distribution.....	21
Figure 2.16: Wing Structural Weight Distribution	23
Figure 2.17: Fuel in Wing Weight Distribution.....	24
Figure 2.18: Distributed Load Summary Profile of Positive 2.5g maneuver (does not include engine point load).....	25

Figure 2.19: Shear and Moment Diagram (Positive 2.5g maneuver)	26
Figure 2.20: Correction for Wing Sweep Illustration	27
Figure 2.21: Fuselage Structure Loading Modeled as Cantilever Beam	29
Figure 2.22: Shear and Moment Distribution for Fuselage Load Case 1 (Positive 2.5g Maneuver)	31
Figure 2.23: Shear and Moment Distribution for Fuselage Load Case 2 (Negative 2.0g Hard Landing)	32
Figure 2.24: Stiffened Panels on the Wing Box Skin	37
Figure 2.25: Principal Stress Components of Pure Shear Buckling (Ref 2)	39
Figure 2.26: Bending Buckling Illustration (Ref 7)	40
Figure 2.27: Compression Shear Buckling Interaction (Ref 7)	42
Figure 2.28: One Edge Free Crippling (logarithmic scale) (Ref 4)	45
Figure 2.29: No Edge Free Crippling (logarithmic scale) (Ref 4)	45
Figure 2.30: Crippling Curves	46
Figure 2.31: Skin Buckled Stiffened Panel and Effective Width Illustration	49
Figure 2.32: Lumping Areas on the Wing Box	65
Figure 2.33: Generic Axial Stress and Skin Thickness Relationship	73
Figure 2.34: Generic Buckling Stability and Axial Stress vs Skin Thickness Relationship	75
Figure 2.35: Optimization Flow Chart (example for fuselage)	77
Figure 3.1: Linear Regression Correlation between PDCYL and Calculated Results	81

Figure 3.2: :Linear Regression Correlation between Actual Load Bearing Weight and Calculated Results.....	81
Figure 3.3: Linear Regression Correlation between Actual Primary Weight and Calculated Results.....	82
Figure 3.4: : Linear Regression Correlation between Actual Total Structural Weight and Calculated Results.....	82
Figure 3.5: Linear Regression Correlation between PDCYL and Calculated Model Results.....	83
Figure 3.6: Linear Regression Correlation between Actual Load Bearing Weight and Calculated Model Results	84
Figure 3.7: Linear Regression Correlation between Actual Primary Weight and Calculated Model Results	84
Figure 3.8: Linear Regression Correlation between Actual Total Structural Weight and Calculated Model Results	85
Figure 3.9: Wing Finite Element Geometry	86
Figure 3.10: Axial Stress in Skin	87
Figure 3.11: Top Skin Element ID Numbers	87
Figure 3.12: Axial and Shear Stresses in Elements 4213 and 4214 (“F06 file”).....	88
Figure 3.13: Axial and Shear Stress from Model	88
Figure 3.14: Axial Stress.....	89
Figure 3.15: Axial Stress from Model	90
Figure 3.16: Shear Stress	91

Figure 3.17: Shear Stress Calculated in Model.....	91
Figure 4.1: Percent Load Bearing Structural Weight Benifit of CFRP over Aluminum for a Range of Potential Fatigue Performance	96
Figure 4.2: Skin Thickness Design Stress Relationship	98
Figure 4.3: Failure Mode Distribution on Wing Structure for Wide and Narrow body (CFRP Baseline and all cases except for narrow body Improved Composite 1).....	99
Figure 4.4: Failure Mode Distribution for Narrow Body Wing (CFRP Improved Composite 1).....	100
Figure 4.5: Failure Mode Distribution on Wide Body Fuselage (CFRP)	101
Figure 4.6: Failure Mode Distribution on Narrow Body Fuselage (CFRP)	102
Figure 4.7: Failure Mode Distribution for Wide Body and Narrow Body Wing (Aluminum).....	105
Figure 4.8: Failure Mode Distribution for Wide Body Fuselage (Aluminum).....	107
Figure 4.9: : Failure Mode Distribution for Narrow Body Fuselage (Aluminum) ...	108
Figure A.1: Medium Body Jet Transport.....	A.1
Figure A.2: V-N Diagram Specifications for Military Airplanes (Ref 6).....	A.2
Figure B.1:WB Wing Running Loads	B.5
Figure B.2: NB Wing Running Loads	B.5
Figure B.3: Crippling of CFRP Laminate "I"-Section Beam With $E_x=14.5\text{Msi}$	B.6
Figure B.4: Euler Column Buckling of CFRP Laminate $E_x=14.5\text{Msi}$	B.7
Figure B.5: Radius of Gyration for Euler Buckling Calculation with Contribution of Effective Width.....	B.8

Figure C.1: 7075 Aluminum Alloy Mechanical Properties (Ref 4).....	C.1
Figure C.2: "K" Values for Compression and Shear Panel Buckling (Ref 7)	C.2
Figure C.3: Stiffness Correction	C.3
Figure D.1: Illustration of Fuselage Modeled as Idealized Tube.....	D.1
Figure D.2: Optimized Thicknesses for Fuselage Section 46.....	D.1
Figure D.3: Lateral Cut of Fuselage as a Idealized Tube	D.3
Figure D.4: Center of Mass (in).....	D.4
Figure D.5: Second Moment of Area (in ⁴).....	D.5
Figure D.6: Internal Loads (shear(lbs), moment(lbs*in)).....	D.6
Figure D.7: Maximum and Minimum Principle Stress in Crown (psi)	D.7
Figure D.8: Minimum Principle Stress in Belly (psi)	D.8
Figure D.9: Max In-plane Shear Stress (psi)	D.10
Figure D.10: Idealized Stringer Section.....	D.11
Figure D.11: Crippling Stress of Belly Stringer	D.13
Figure D.12: Geometry of Hat Stiffener	D.13
Figure D.13: Hat Stiffener Including Effective Width	D.16
Figure D.14: Belly Stringer Buckling Strength	D.17
Figure D.15: Output for WB CFRP Baseline	D.19

List of Tables

Table 2.1: Wing Model Geometry Values	9
Table 2.2: Fuselage Model Geometry Values.....	11
Table 2.3: Wing Stiffened Panel Geometry Values (CFRP)	12
Table 2.4: Wing Striffened Panel Geometry Values (Aluminum)	12
Table 2.5: Wing Stringer Geometry (CFRP)	14
Table 2.6: Wing Stringer Geometry (Aluminum).....	14
Table 2.7: Fuselage Stiffened Panel Geometry Values (CFRP).....	15
Table 2.8: Fuselage Stiffened Panel Geometry Values (Aluminum)	15
Table 2.9:Fuselage Stringer Geometry (CFRP).....	17
Table 2.10: Fuselage Stringer Geometry (Aluminum)	17
Table 2.11: Fuel Weight Breakdown	24
Table 2.12: CFRP Lamina Properties	51
Table 2.13: CFRP Laminate Properties	52
Table 2.14: 7075-T6 Aluminum Alloy Properties	55
Table 3.1: Wing Regression Analysis Data	80
Table 3.2: Fuselage Regression Analysis Data.....	83
Table 4.1: CFRP Baseline and Enhanced Material Weights (% Structural Weight Reduction).....	93
Table 4.2: Aluminum Baseline and Enhanced Material Weights (% Structural Weight Reduction).....	94

Table 4.3: Stiffened and Un-stiffened Structural Weights.....	95
---	----

Nomenclature

English

Symbol	Description	Units
[A]	Linear Inequality Constraint Matrix	~
[C]	Non-Linear Constraint Matrix	~
[D]	Laminate Flexure Stiffness Matrix	in-lb
[LB]	Optimization Lower Bound	~
[UB]	Optimization Upper Bound	~
{b}	Non-linear Inequality Limit	~
a	Stiffened Panel Length	in.
A	Cross Section Area	in ²
a _i	Discrete Lumped Area	in ²
b	Wing Span	ft
b _c	Stiffener Cap Panel Width	in
b _f	Stiffener Flange Width	in
b _w	Stiffener Web Width	in
c	Wing Chord	ft
D	Fuselage Diameter	ft
D _{mn}	Flexural Stiffness Matrix Term	in-lb
E	Elastic Modulus	psi
F	Stress (Military Handbook Notation)	psi

f	Optimization Cost Function	in ²
g	Inequality Constraint	~
I	Second Moment of Area	in ⁴
	Distance to Wing Kick (in percent% wing half	
k	span)	~
l	Fuselage Length	ft
L	Length of Longitudinal Stiffener	in.
L'	Distributed Lift	lb/in
M	Internal Moment Load	lb-in
n	Load Factor	~
p	Net Distributed Load	lb/in
q	Shear Flow	lb/in
Q	First Moment of Area	in ³
R	Critical Buckling Stress Ratio	~
S	Wing Planform Surface Area	ft ²
T	Gross Engine Thrust	lb
t	Thickness	in
V	Internal Shear Load	lb
W	Weight	lb
w	Thin Plate Deflection	in.
x	Structure Axial Coordinate	ft
y	Structure Lateral Coordinate	in.

Acronyms	Description	
AR	Wing Aspect Ratio	~
M.S.	Margin of Safety	~
OHC	Open Hole Compression Strength	psi
OHT	Open Hole Tension Strength	psi
S.F.	Safety Factor	~
W.S.	Wing Station	ft
PDCYL	NASA's Structural Weight Estimate	

Greek Symbol	Description	
$\Delta\sigma$	Change in Stress Allowable	psi
Δt	Change in Thickness	in.
λ	Taper Ratio	~
Λ	Sweep Angle	Degrees
ν	Poisson's Ratio	~
θ	Stiffener Web Inclination Angle	Degrees
ρ	Radius of Gyration	in.
σ	Axial or Transverse Stress	psi
τ	Shear Stress	psi

Subscript	Description
0	Initial Value
1	Maximum Principal Direction/Fiber Direction
2	Minimum Principal Direction/Transverse Direction
	Laminate Flexural Stiffness Response to In-Plane Bending
11	Strain
	Laminate Flexural Stiffness Response to Transverse
12	Bending Strain
	Laminate Transverse Flexural Response to Transverse
22	Bending Strain
	Laminate Torsional Flexure Response to In-Plane Torsional
66	Strain
1,2i	Principal Stress of a Discrete Lumped Area
12su	Lamina Ultimate Shear Strength
1cu	Lamina Ultimate Compression Strength in Fiber Direction
1tu	Lamina Ultimate Tensile Strength in Fiber Direction
	Lamina Ultimate Compression Strength Transverse to Fiber
2cu	Direction
	Lamina Ultimate Tensile Strength Transverse to Fiber
2tu	Direction
All	Allowable Stress
b	Bending Stress

c	Compression Stress
cc	Crippling Strength
CL	Wing Center Line
cr	Critical Buckling Strength
cr_stiff	Critical Buckling Strength of Stiffener
cu	Ultimate Compression Strength
Design	Design Stress
e	Effective Length
engine/pylon	Engine and Pylon Weight
exp	Exposed Wing Area
	Fracture Margin of Safety/Flange Width/ Forward Fuselage
f	Location/Fiber Volume
fi	Final Thickness of Discrete Structural Area
Fract_sk_Bottom	Critical Fracture of Bottom Skin
Fract_sk_Top	Critical Fracture of Top Skin
Fract_st_Bottom	Critical Fracture of Bottom Stiffener
Fract_st_Top	Critical Fracture of Top Stiffener
Fracture_Allowable	Fracture Strength
fuselage	Fuselage Cross Sectional Area
G	Center of Area
GTO	Gross Takeoff Weight
h	High Relative Stress Range

Subscript	Description
kick	Wing Thickness/Depth at Wing Kick
l	Low Relative Stress Range
L	Longitudinal Stress Ratio
LE	Leading Edge Sweep/ Swept Span
Limit	Stress at Limit Load
Linear	Linear Inequality Constraint
MGTO	Maximum Gross Takeoff Weight
Non-Linear	Non-Linear Inequality Constraint
OHC	Open Hole Compression Strength
OHT	Open Hole Tension Strength
oi	Initial Thickness of Discrete Lumped Structure
p	Panel Geometry
r	Root Chord/Thickness
r_wb	Root Chord of Wing Box
ref	Reference
s	Shear Stress Ratio
skin	Fuselage Cross Section Skin Area
Spar_Caps	Wing Cross Section Spar Caps Area
Spar_Webs	Wing Cross Section Spar Web Area
stiff	Stress in Stiffener

stringers	Wing/Fuselage Cross Section Stringer Area
su	Shear Ultimate
t	Tip Chord/Thickness
t_wb	Tip Chord of Wing Box
tu	Tensile Ultimate
wing	Wing Cross Section Area
x	In-Plane Axial Mechanical Properties/Stress
	In-Plane Axial Mechanical Properties/Stress of Discrete
xi	Structure
xy	In-Plane Shear Mechanical Properties/Stress
	In-Plane Shear Mechanical Properties/Stress of Discrete
xyi	Structure
y	Transverse Axial Mechanical Properties/Stress
	Lateral First/Second Moment of Area (Referenced Text
z	Notation)
z_LC1	Vertical Load Factor for Load Case 1
z_LC2	Vertical Load Factor for Load Case 2
	Lateral First/Second Moment of Area (Referenced Text
zz	Notation)

1 Introduction

1.1 Objective

The main objective of this study is to determine if potential mechanical property enhancements of CFRP material would lend themselves to the application on smaller transport aircraft, referred to as the narrow body aircraft. This is determined by identifying and comparing critical failure modes of CFRP and Aluminum Alloys on medium and small commercial jet transport. It is currently known that CFRP materials show benefits over Aluminum Alloys for current medium jet transport aircraft, referred to as the wide body aircraft. This study is a weight sensitivity analysis only and does not take into account factors such as Acquisition and Life Cycle cost and is not intended to compare Aluminum Alloy to CFRP Laminate materials. The general questions that this analysis addresses are:

How does the weight performance benefits from the application of CFRP and Aluminum Alloy on a medium transport aircraft compare with that on a small transport aircraft?

What CFRP material enhancements offer the most weight benefit on the wide and narrow body aircraft and what are the critical failure modes?

What Aluminum Alloy material enhancements offer the most weight benefit on the wide and narrow body aircraft and what are the critical failure modes?

This study presents a method of estimating the wing box and fuselage geometry from fundamental preliminary design parameters. Also presented is an analytical method using optimization to evaluate the weight benefits of altering the material properties of the structure. This optimization model will be useful in studying the effects and limitations of enhancing aspect of a unidirectional material on the wing and fuselage structure. This method determines the primary load bearing structural mass by sizing the skin and the stringers, but not the fuselage frames or wing ribs. The only input parameters in this analysis are mechanical properties of the material. Therefore there is not a configuration trade study included and the configuration concept is fixed, though the dimensions of the structural concept are optimized for the specific baseline material and transport aircraft size.

1.2 *Prior Work*

A parallel study was found in a NASA Technical Memorandum Titled: *Analytical Fuselage and Wing Weight Estimation of Transport Aircraft*. The document presents an methodical procedure in defining the structure geometry, loads, and failure criteria in order to estimate the structural load, similar to the procedure presented in this document. Unlike this study, the procedure does not include

compression and shear buckling interaction, sub-structure of different in-plane stiffness, and did not study “I”-beam and “Hat”-section stiffened concepts. It does include, unlike this study, curvature of fuselage geometry, deflection analysis, the sizing and weight of fuselage frames and wing ribs, and the study of “Z” –section and Sandwich Honeycomb stiffened configurations.

The technical memorandum tabulates the actual structural weights of eight **Aluminum Alloy** transport aircrafts and compares the weights with the calculated structural weight of their model. This study uses those published weights to verify the optimized weight calculations for the eight transport aircraft using the optimized model documented in this study. The results are presented in the verification section.

Figure 2.1 illustrates the geometry for the wing for the wide body jet transport. The known wing geometry includes the Aspect ratio AR , span b , and leading edge sweep Λ_{LE} . The wing reference surface area S_{ref} is determined from the aspect ratio and span in Equation 1. The span, reference surface area, and the chord distribution for the wide body, presented in Figure 2.2, is used to calculate the mean geometric chord \bar{c} . The formula used to calculate mean geometric chord is shown in Equation 2. This chord distribution is determined from Figure A.1 in Appendix A. Since the chord distribution is known the root chord c_r and the tip chord c_t are known. Figure 2.1 shows that the leading edge has a constant sweep. The quarter chord sweep $\Lambda_{c/4}$ is determined by Equation 3. The exposed wing reference area S_{exp} is equal to the reference wing area minus the referenced wing area within the fuselage diameter (or fuselage wall) shown in Figure 2.2.

(1)

$$AR = \frac{b^2}{S_{ref}}$$

(2)

$$\bar{c} = \frac{2}{S_{ref}} \int_0^{\frac{b}{2}} c^2 dy$$

(3)

$$\tan \Lambda_{c/4} = \frac{3}{4} \tan \Lambda_{LE}$$

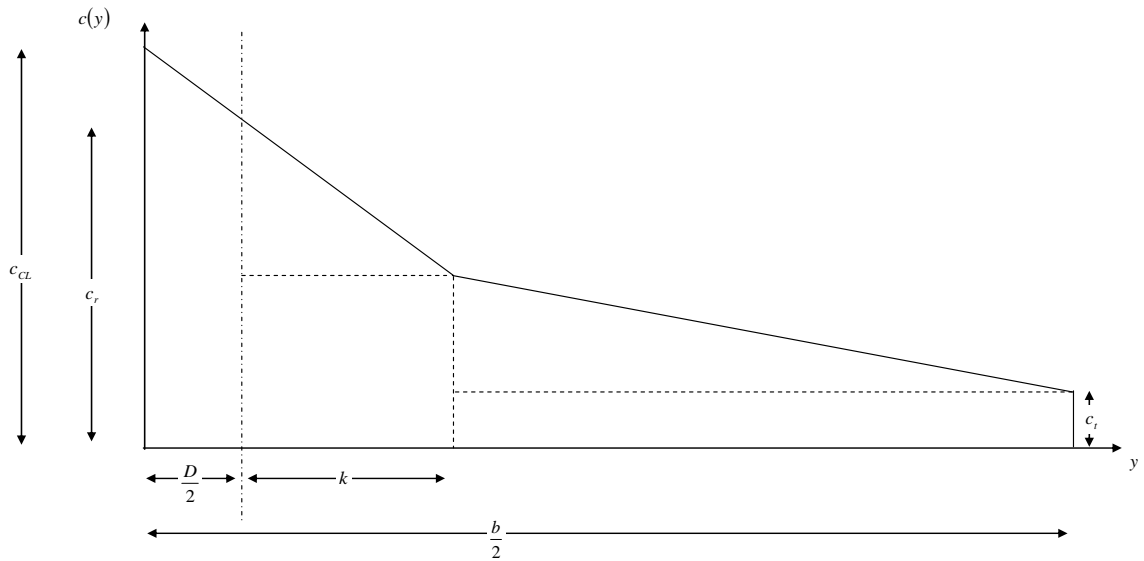


Figure 2.2: Wing Chord Distribution

The wing box structure extends the span of the wing and the width of the wing box is a fraction of the chord for a specific wing station. The wing box is shown within the geometry of the wing planform in Figure 2.3. It is assumed for simplicity of analysis that the center of the wing box is located at the quarter chord of the wing planform which is also assumed to be the location of the aerodynamic center and center of pressure. This implied that the aerodynamic resultant force is located at the center of the wing box and that there is no pitching moment on the wing. The configurations for the wide and narrow body transport structures are both two spar concepts with rib spacing indicated by the stiffened panel geometry length.

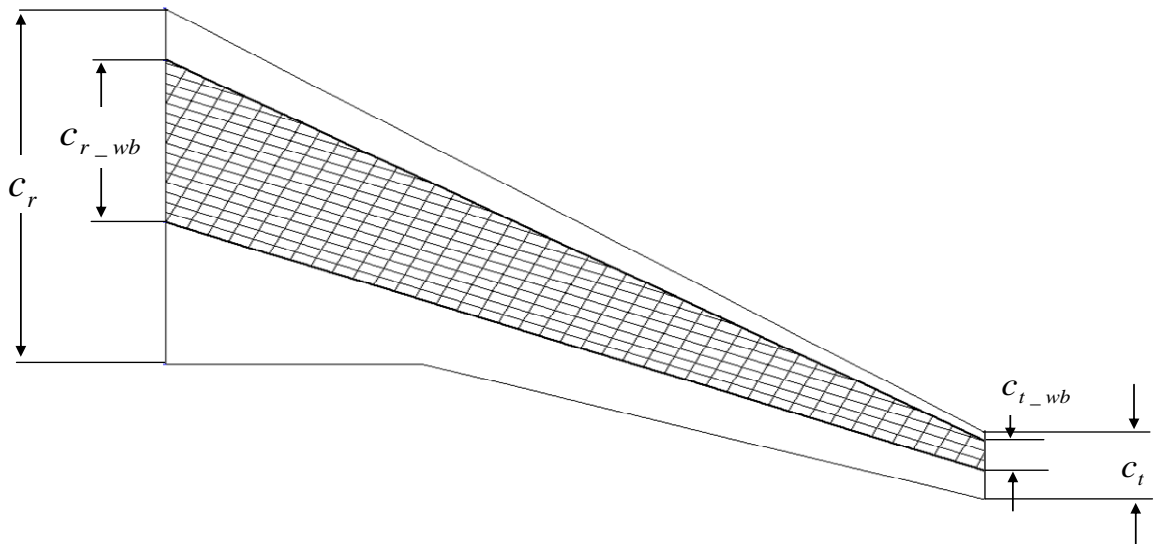


Figure 2.3 Wingbox and Wing Planform

The wing-box thickness (not to be confused with skin thickness) and wing box with taper transition at the “kick” is illustrated in Figure 2.4. This is an important detail to recognize because there is a large thickness taper from the root to the “kick” and a subtle thickness taper from the “kick” to the tip, which has a large effect on the running load profile distribution over the wing span. There is a beam that runs behind the rear landing gear, from the reference wing planform centerline to the “kick” this beam is neglected in this analysis because the details needed to size this beam were not readily available. The geometry parameters of the wing are presented in Table 2.1.

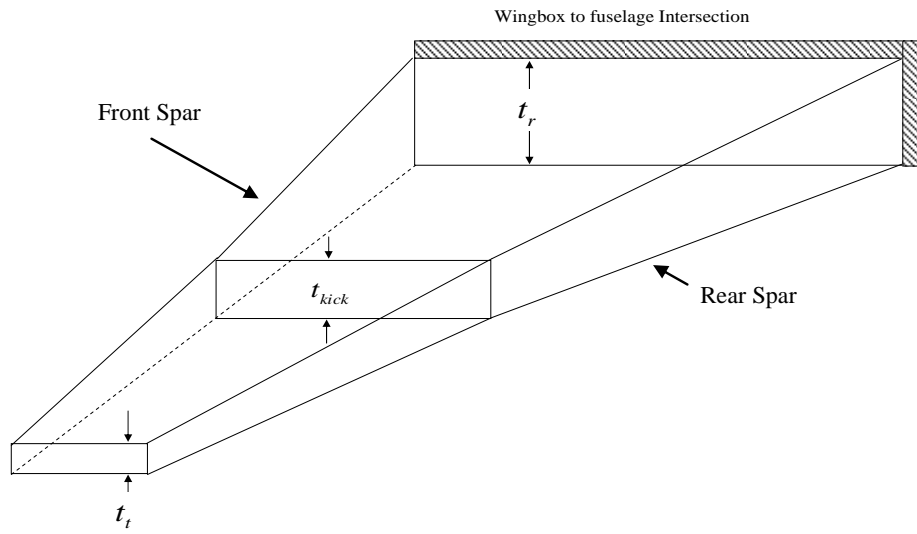


Figure 2.4: Illustration of Wingbox Thickness Taper (this is not a configuration concept illustration and there is no rib geometry displayed in this figure)

Table 2.1: Wing Model Geometry Values

Parameter Designation	Parameter Name and Description	Units	Narrow Body (NB) Value	Wide Body (WB) Value
WGTO	Maximum Gross Takeoff Weight	lbs	123,675	453,000
b	Wing Span	ft	112	170
D	Fuselage Diameter	ft	13	19
AR	Aspect Ratio, $AR=b^2/S_{ref}$	~	9.55	9.55
Λ_{LE}	Leading Edge Sweep	degrees	40	40
λ_{ref}	Reference Chord Taper Ratio, $\lambda_{ref}=c_t/c_{CL}$	~	NA	NA
λ_{exp}	Exposed Chord Taper Ratio, $\lambda_{exp}=c_t/c_r$	~	0.1875	0.1875
$\left(\frac{t}{c}\right)_r$	Thickness to Chord Ratio at Wing Root, $(t/c)_r = t_r/c_r$	~	0.10	0.10
τ_{exp}	Exposed Thickness Ratio, $\tau_{exp} = t_t/t_r$	~	0.1883	0.1883
r_r	Wingbox to Wing Planform Chord Ratio at Root, $r_r = c_{r_wb}/c_r$	~	0.41	0.41
r_t	Wingbox to Wing Planform Chord Ratio at Tip, $r_t = c_{t_wb}/c_t$	~	0.31	0.31
kick	Distance to Kick from Wing Root (as fraction of wing half span), $kick = k/(b/2)$	~	0.254	0.254
$\left(\frac{t}{c}\right)_k$	Thickness to Chord Ratio kick, $(t/c)_k = t_{kick}/c_{kick}$	~	0.10	0.10

2.1.2 Fuselage

The Fuselage is modeled as an un-tapered cylinder neglecting wing and empennage attachment structure. The maximum diameter of the actual fuselage structure is used for the diameter of the cylinder. The length of the cylinder extends from the nose to the tail cone.

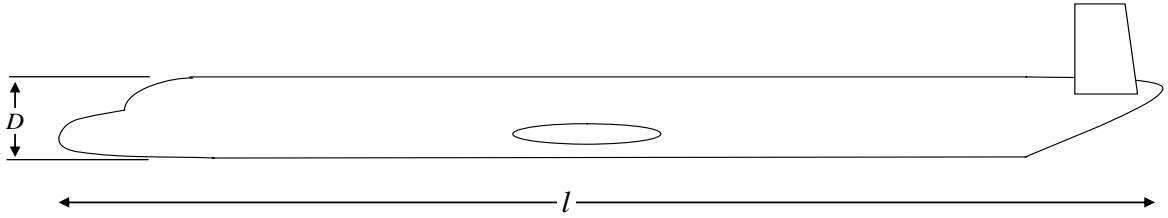


Figure 2.5: Fuselage Geometry

(4)

$$l = 0.67W_{GTO}^{0.43} \text{ (Ref 2)}$$

The fuselage geometry is defined in terms of the fineness ratio l/D , and the maximum gross takeoff weight. The length and diameter of the fuselage are illustrated in Figure 2.5. The Gross Takeoff Weight and fuselage slenderness ratio for the wide and narrow body aircraft is given in Table 2.2. Equation 4 estimates the fuselage length from the gross takeoff weight.

Table 2.2: Fuselage Model Geometry Values

Parameter Designation	Parameter Name and Description	Units	Narrow Body (NB) Value	Wide Body (WB) Value
W_{GTO}	Gross Takeoff Weight	lb	123,675	453,000
l/D	Fuselage Length to Diameter Ratio	(~)	7.8	9.6

2.2 Stiffened Panel Geometry

In order to compare the stability of the stiffened panels at the proper stress level the stiffener spacing and geometry is found using an iterative process presented in Appendix B. The “T”-beam section is used to stiffen the wing skin panels and the “Hat”-section stiffener is used on the fuselage. Figure 2.6 shows an “T” beam stiffened panel using a finite element modeling software. Figure 2.8 shows a solid model of a hat stiffened panel with the panel width b and panel length a defined.

Tables 2.3 and 2.4 give the wing stiffened panel geometry values for CFRP and Aluminum Alloy respectively. Tables 2.7 and 2.8 give the stiffened panel geometry for the CFRP and Aluminum Alloy fuselage. The stiffened panel geometry is compared for CFRP and Aluminum Alloy for the specific wide or narrow body wing or fuselage structural with the un-stiffened structural weight in the results. The b/t stiffener spacing to panel thickness ratio is a function of material stiffness E , stress in the panel σ_x , Poisson’s ratio ν , and boundary conditions. The panel width to skin

thickness ratio b/t should be similar for every like material geometry combination
(i.e. The Aluminum Alloy narrow and wide body wing structure).

2.2.1 Wing

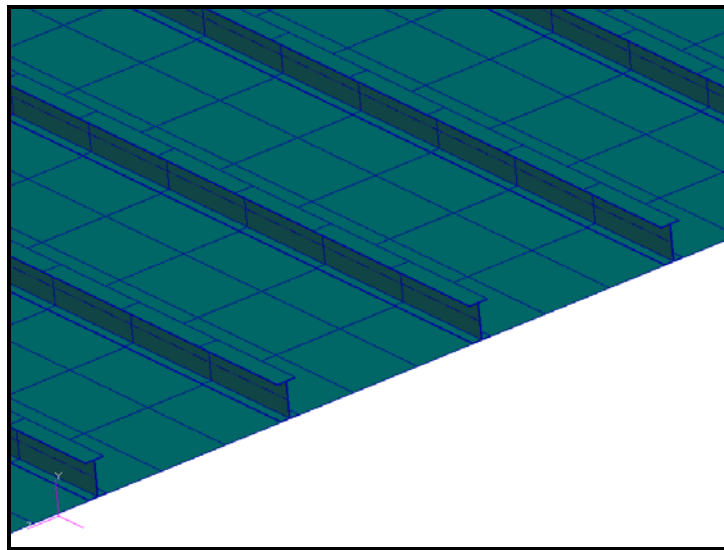


Figure 2.6: "I" beam Section Stiffened Panel

Table 2.3: Wing Stiffened Panel Geometry Values (CFRP)

Parameter Designation	Parameter Name and Description	Units	Narrow Body (NB) Value	Wide Body (WB) Value
b	Panel Width	in	7.0	17.0
a	Panel Length	in	14.0	34.0

Table 2.4: Wing Striffened Panel Geometry Values (Aluminum)

Parameter Designation	Parameter Name and Description	Units	Narrow Body (NB) Value	Wide Body (WB) Value
b	Panel Width	in	2.3	5.7
a	Panel Length	in	4.6	11.4

Figure 2.7 shows the geometry of the “I”-section stiffener. The y_i displacements are used as inputs in determining the radius of gyration and effective width in the model, there values are not tabulated in this section. Table 2.5 and 2.6 give the geometry values of the CFRP and Aluminum Alloy stiffeners for the wing respectively. The stiffener is assumed to be bonded to the wing skin. The “I” beam stiffener configuration is chosen because it is what is currently being used in industry on a medium transport aircraft with CFRP as its primary load bearing material.

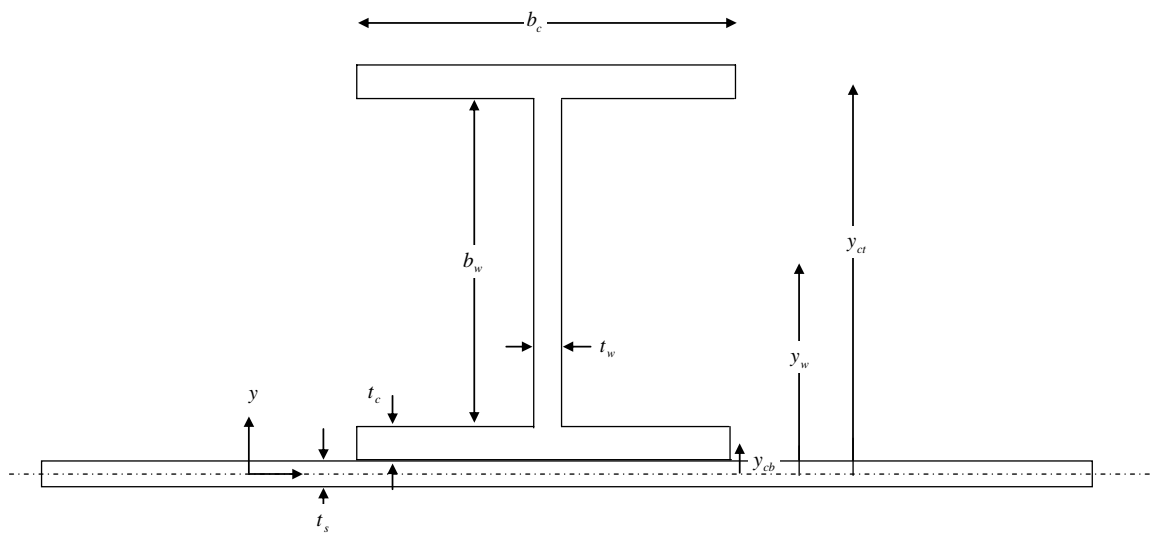


Figure 2.7: Geometry of an "I"-Beam Section Stiffener

Table 2.5: Wing Stringer Geometry (CFRP)

Parameter Designation	Parameter Name and Description	Units	Narrow Body (NB) Value	Wide Body (WB) Value
b_w	Stiffener I-Section Web Width	in.	1.00	2.00
b_f	Stiffener I-Section Flange Width	in.	0.55	1.30

Table 2.6: Wing Stringer Geometry (Aluminum)

Parameter Designation	Parameter Name and Description	Units	Narrow Body (NB) Value	Wide Body (WB) Value
b_w	Stiffener I-Section Web Width	in.	0.40	1.00
b_f	Stiffener I-Section Flange Width	in.	0.25	0.65

2.2.2 Fuselage

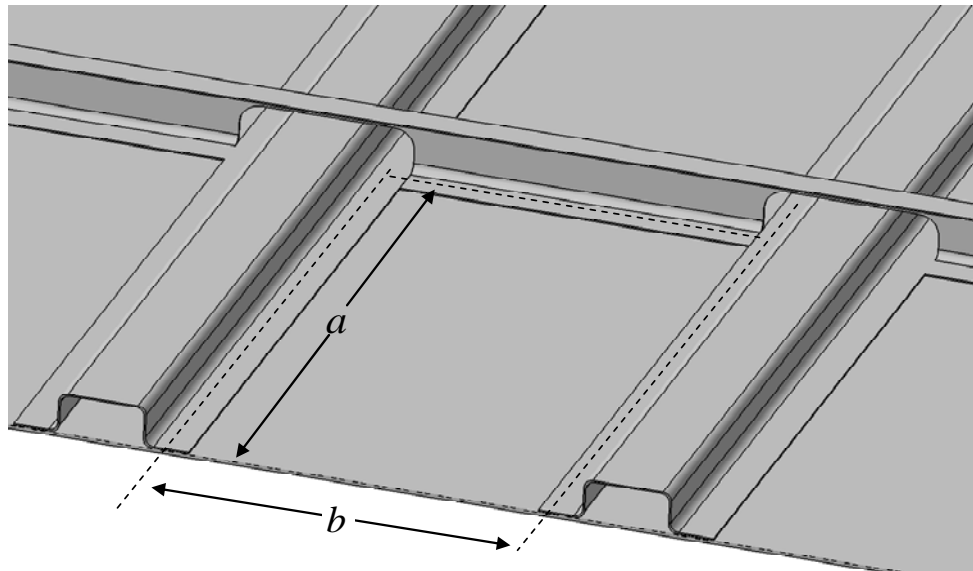


Figure 2.8: "Hat"-Section Stiffened Panel

Table 2.7: Fuselage Stiffened Panel Geometry Values (CFRP)

Parameter Designation	Parameter Name and Description	Units	Narrow Body (NB) Value	Wide Body (WB) Value
b	Panel Width	in	6.3	11.0
a	Panel Length	in	9.4	16.4

Table 2.8: Fuselage Stiffened Panel Geometry Values (Aluminum)

Parameter Designation	Parameter Name and Description	Units	Narrow Body (NB) Value	Wide Body (WB) Value
b	Panel Width	in	2.5	4.4
a	Panel Length	in	3.8	6.5

Figure 2.8 shows the geometry of the “Hat”-section stiffened panel. The webs of the stiffener are actually at an angle like what is shown in Figure 2.9. The angle of the hat stiffener web is used when determining the radius of gyration of the stiffener. The flange of the stiffener, with width b_f in Figure 2.9, is attached to the skin of the fuselage. All flanges are assumed to be bonded to the fuselage skin. Like the “I”-section stiffener the y_i lateral locations of the legs of the stiffener are inputs in the model to compute the radius of gyration and are functions of the stiffener dimensions and the wing or fuselage skin thickness (i.e. $f(b_i, t)$). The geometry of the “Hat”-section stiffener is given in Table 2.9 and 2.10 for the CFRP and Aluminum Alloy material respectively. The “Hat”-section stiffener is chosen because it is currently being used in industry on a medium transport aircraft with CFRP as its primary load bearing material. The stiffened panel geometry given in this section is a fixed input in the model and is not allowed to vary since the scope of this study is reduced to benefits of the material mechanical properties only. The stiffened panel geometry is optimized prior to the sensitivity analysis.

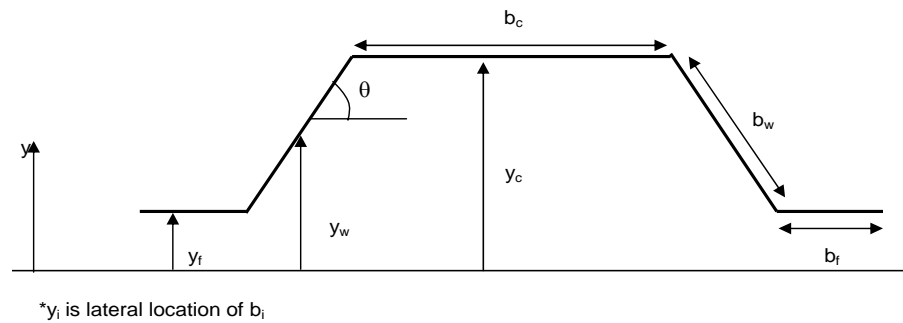


Figure 2.9: Geometry of a Hat Stiffener

Table 2.9: Fuselage Stringer Geometry (CFRP)

Parameter Designation	Parameter Name and Description	Units	Narrow Body (NB) Value	Wide Body (WB) Value
b_w	Stiffener Hat-Section Web Width	in.	0.66	1.00
b_f	Stiffener Hat-Section Flange Width	in.	0.50	0.50
b_c	Stiffener Hat-Section Cap Width	in.	1.00	1.50
θ	Stiffener Hat-Section Web Angle	Degrees	43	43

Table 2.10: Fuselage Stringer Geometry (Aluminum)

Parameter Designation	Parameter Name and Description	Units	Narrow Body (NB) Value	Wide Body (WB) Value
b_w	Stiffener Hat-Section Web Width	in.	0.35	0.70
b_f	Stiffener Hat-Section Flange Width	in.	0.30	0.45
b_c	Stiffener Hat-Section Cap Width	in.	0.70	1.40
θ	Stiffener Hat-Section Web Angle	Degrees	43	43

2.3 Loads

2.3.1 Wing

The critical load cases being analyzed is a positive 2.5g maneuver and a negative 1.0g gust at limit load that is a standard specification for Jet Transport Aircraft (Ref 7). Figure 2.10 and 2.11 illustrates the difference between the two load cases. Figure A.2, in Appendix A, shows the V-N diagram for transport military aircraft. The load case for the medium transport military aircraft is the same for the commercial medium transport. The medium transport loading capability is marked in Figure A.2. All load cases are symmetric about the center axis of the fuselage. There is no torsion, drag, or dynamic load cases applied to the wing because the details required for these load cases is out of the scope of this sensitivity analysis.

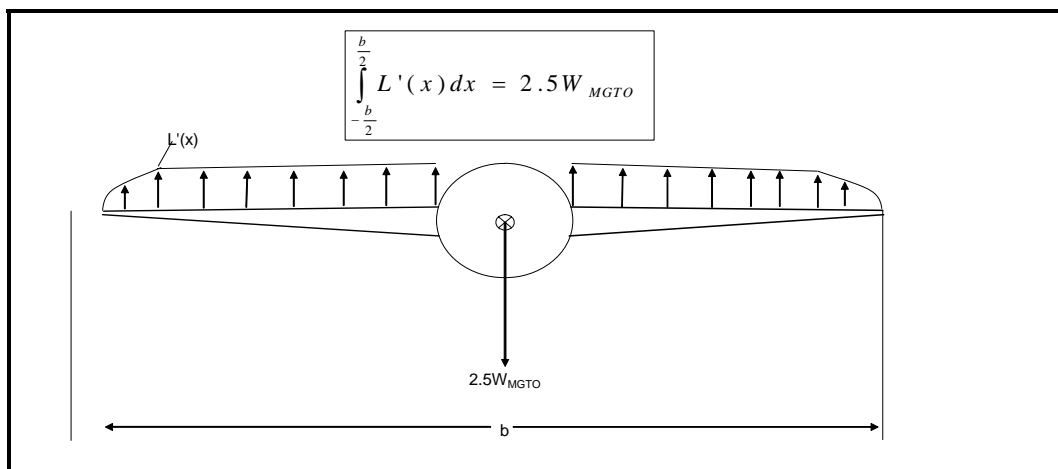


Figure 2.10: Generic Load Profile for 2.5g Positive Maneuver

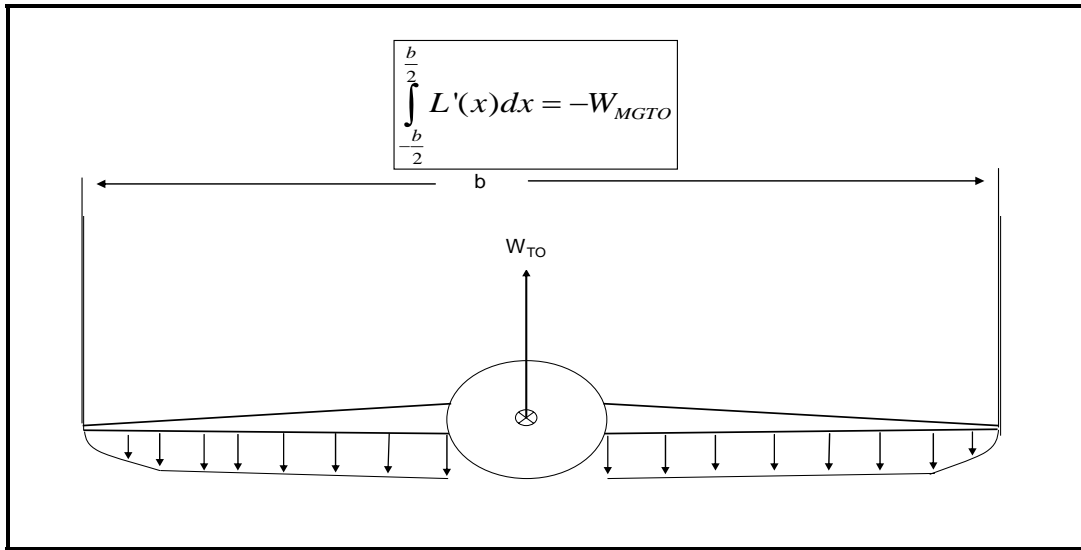


Figure 2.11: Generic Load Profile for Negative 1.0g Gust

2.3.1.1 Lift Profile

Using Shrenk's Approximation (Ref 3) it is required to find the trapezoidal chord distribution of the wing, shown in Figure 2.12, and the theoretical elliptical chord distribution of the wing illustrated in Figure 2.13. According to Shrenk's approximation the lift distribution is proportional to the average of the Trapezoidal and the elliptic chord distribution. Figure 2.14 plots the comparison between the two distributions. Figure 2.15 shows the resultant lift distribution of the two geometrically averaged. Figure 2.15 gives a linear approximation of the lift distribution which can be used as a short hand method to assure that the distribution sums to the gross takeoff weight; this calculation is shown in Equation 5 (453,000 lb is the gross takeoff weight of the wide body aircraft). Half the gross takeoff weight would be experienced by the half span of the wing in steady level 1.0g flight.

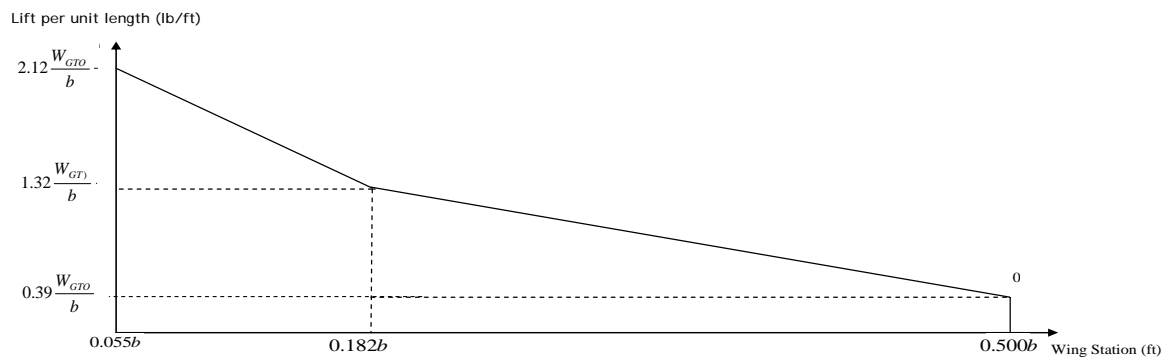


Figure 2.12: Trapezoidal Lift Distribution (1g Steady Level Flight)

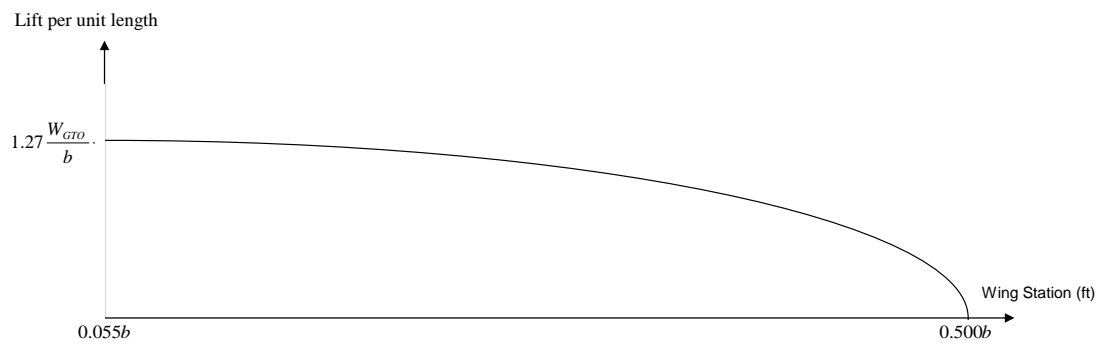


Figure 2.13: Elliptical Lift Distribution (1g Steady Level Flight)

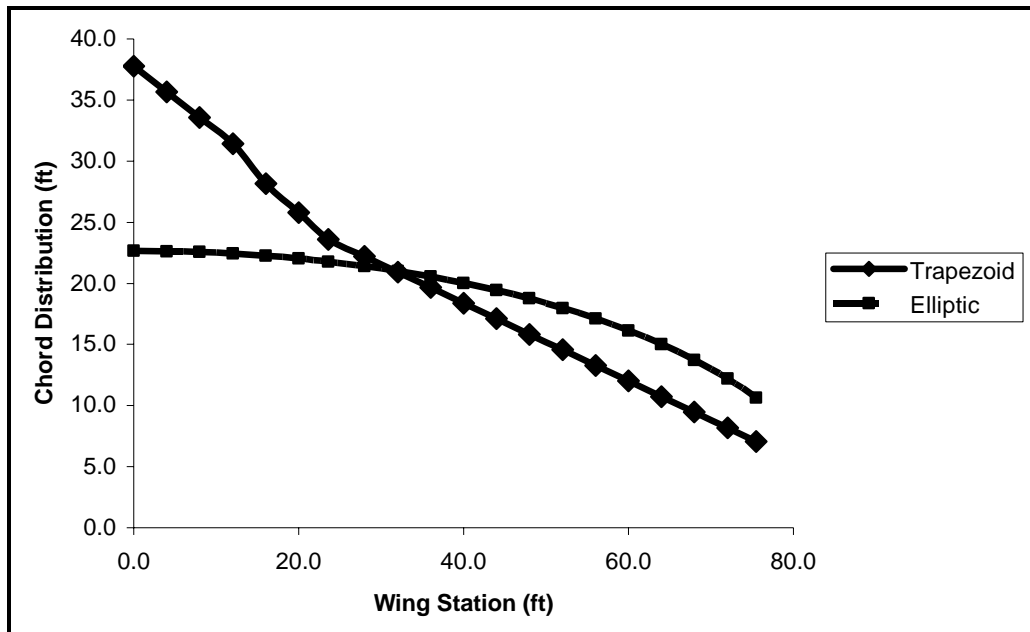


Figure 2.14: Plot of Trapezoid and Elliptic Chord Distribution

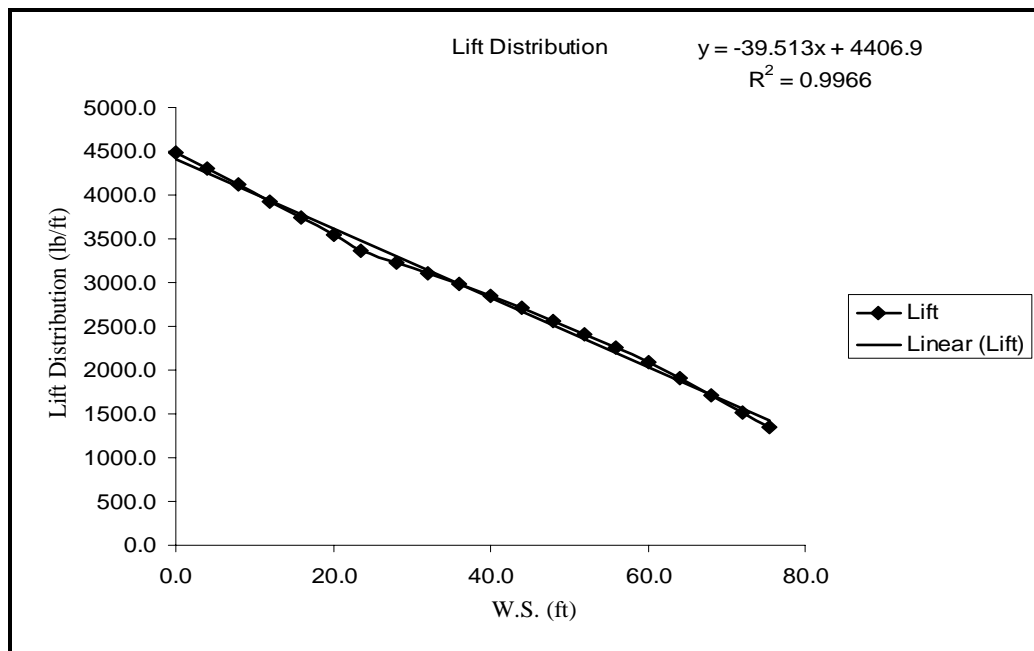


Figure 2.15: Lift Distribution

(5)

$$Total_Load = 2 \left[\frac{\left(4500 \frac{lb}{ft} - 1500 \frac{lb}{ft} \right) (75 ft)}{2} + \left(1500 \frac{lb}{ft} \right) (75 ft) \right] = 450,000 \approx 453,000 lb$$

2.3.1.2 Inertial Relief

2.3.1.2.1 Wing Weight

The wing total structural weight is modeled with wing trapezoidal chord distribution, shown in Figure 2.16, which is similar to the trapezoidal approximation of the lift distribution. The weight of the wing is subtracted from the lift profile. This is consistent with the load case because when the wing is experiencing a positive 2.5g maneuver the wing weight is resisting the motion with the same load factor. The wing total structural weight is estimated to be 12% of the Gross Takeoff Weight. The wing structural weight distribution is a fixed function of the aircraft gross takeoff weight of the aircraft regardless of the material applied to the structure this is done because there is a large amount of the structural mass in the wing that cannot be accounted for in this sensitivity analysis.

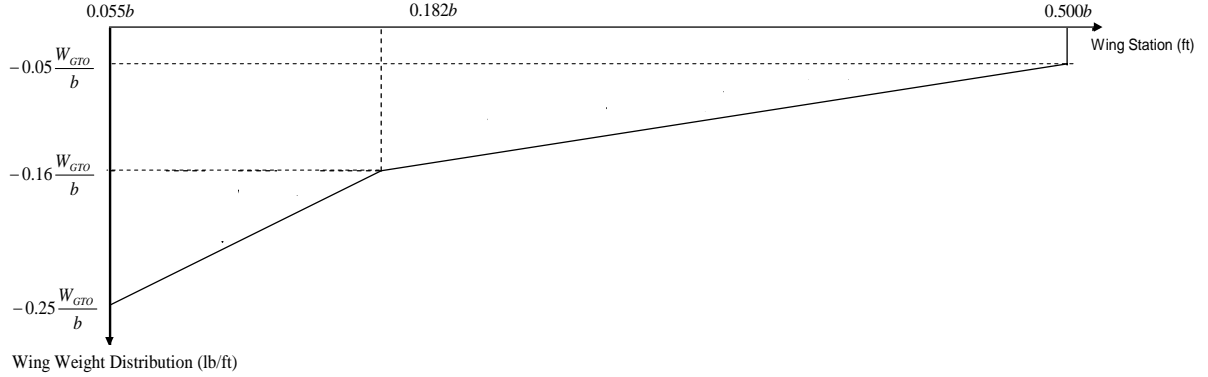


Figure 2.16: Wing Structural Weight Distribution

2.3.1.2.2 Engine and Pylon Weight

The engine weight load is applied at the location of the wing kick (25.4% of the wing half-span outboard of the wing-fuselage intersection). The weight of the engine and the pylon is applied as a discrete point load on the wing. There are two engines, one on each wing, for both the wide and narrow body aircraft. Equation 6 estimates the engine pylon weight using the gross takeoff weight and the maximum thrust to weight ratio.

(6)

$$W_{Engine / Pylon} = 0.064 \left(\frac{1}{\#_of_Engines} \frac{T}{W} W_{GTO} \right)^{1.1} \quad (\text{Ref 3})$$

2.3.1.2.3 Fuel Weight

It is assumed that the portion of the total fuel in the wing, specified in Table 2.12, is 80%. The fuel distribution, shown in Figure 2.17, is assumed to taper linearly to zero within the span of one wing. The fuel weight, along with the engine and wing structural weight, is subtracted from the positive lift distribution for the resultant loading on the wing structure.

Table 2.11: Fuel Weight Breakdown

Fuel	
% Weight _{fuel}	35%W _{TO}
%Weight _{fuel in wing}	80%W _{fuel}
%b _{span} occupied by fuel	100%b _{span}

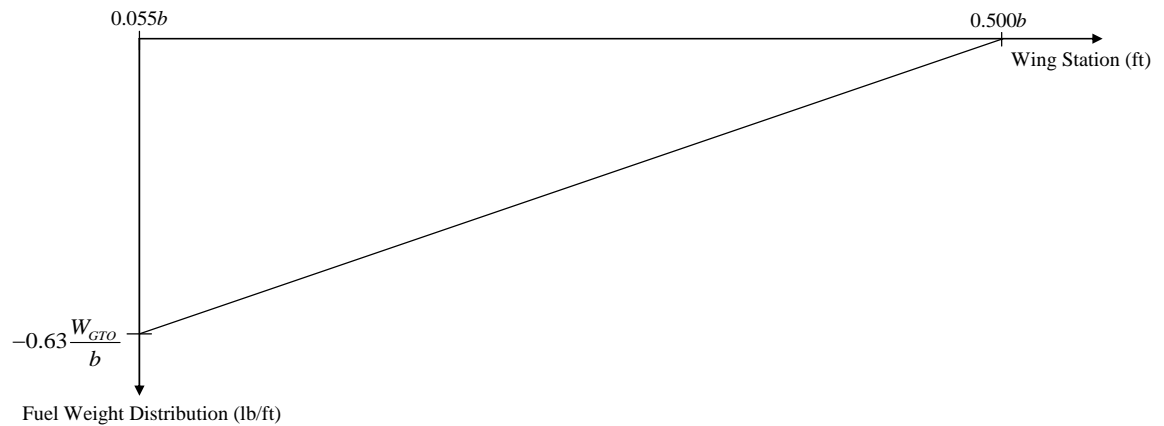


Figure 2.17: Fuel in Wing Weight Distribution

2.3.1.3 Load Summary

The lift distribution for the positive 2.5g load case is given in Figure 2.18.

The negative 1.0g load case would take the same profile but in the negative lift direction with 40% of the magnitude. Both load cases on the wing structure are quasi-static and symmetric.

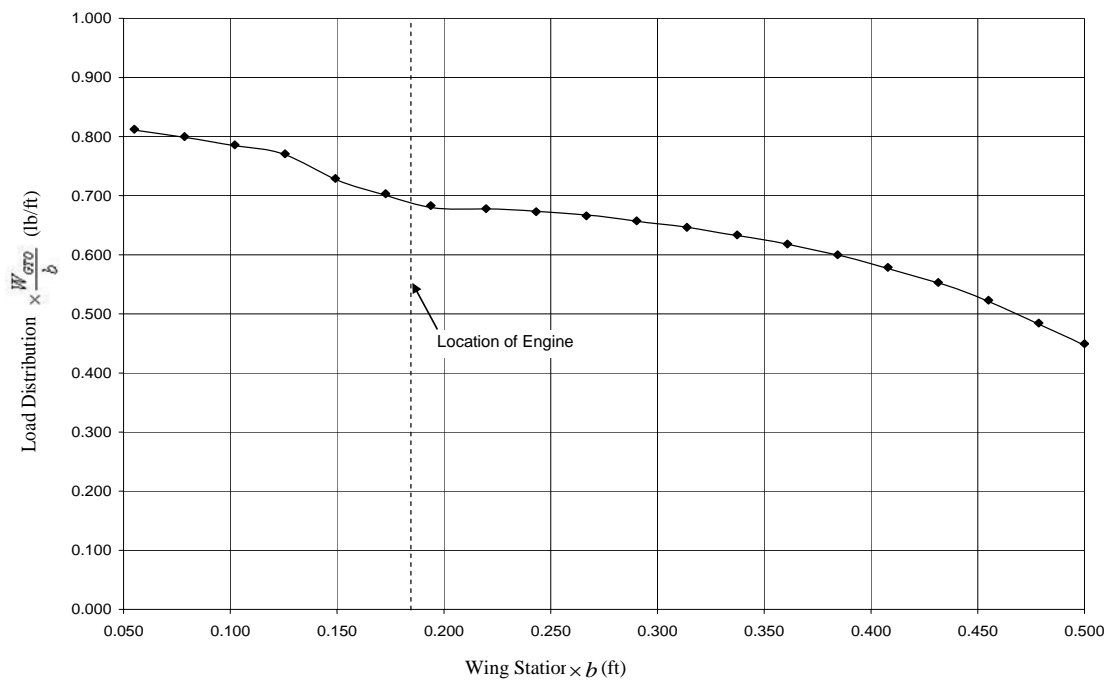


Figure 2.18: Distributed Load Summary Profile of Positive 2.5g maneuver (does not include engine point load)

2.3.1.4 Internal Loading

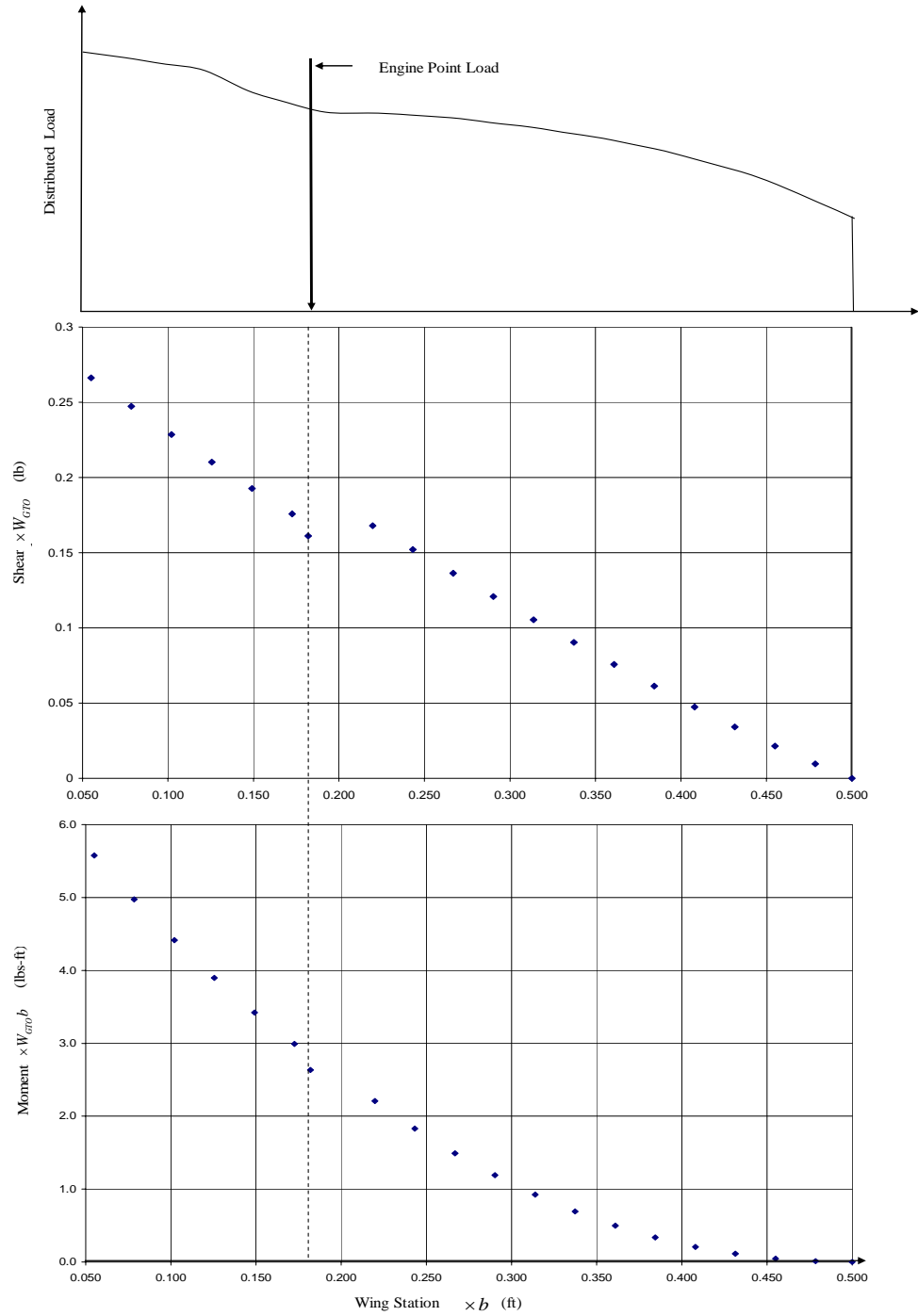


Figure 2.19: Shear and Moment Diagram (Positive 2.5g maneuver)

2.3.1.5 Load Distribution Correction for Sweep

The load distribution $p(x)$ is reduced to its component perpendicular to the quarter chord swept span, to account for the effects of a wing sweep.. This will stretch the shear distribution over the swept span while maintaining the same shear loading at the root. The moment at the root will increase. The calculation for quarter chord sweep is given in Equation 3.

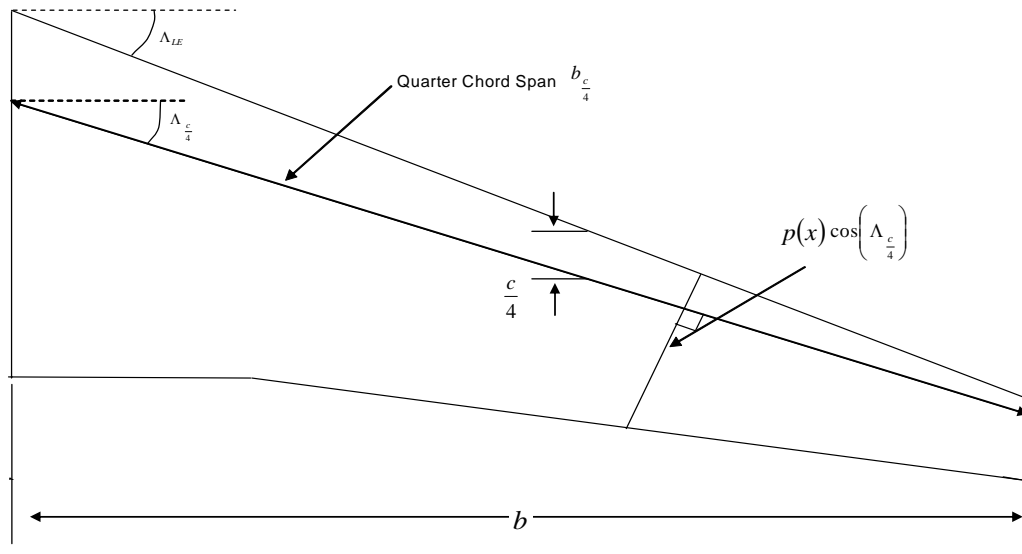


Figure 2.20: Correction for Wing Sweep Illustration

2.3.2 Fuselage

The fuselage structure is sized using two load cases: a positive 2.5g maneuver and a negative 2.0g hard landing. Static load cases are used, for this sizing analysis,

which exclude external aerodynamic pressure forces from drag or bending moments from thrust lines of the engines. The hard landing load case takes into account the nose down pitch rate of the fuselage.

This model only takes into account symmetrical load conditions, therefore there is no torsion induced on the fuselage structure. Two load cases are applied individually. The worst case scenario for the crown and belly of any fuselage section is taken for a given failure mode. The model does account for pressurization, but neglects the effects of pressurization on fuselage sections in compression and sections that are failure critical from load case 2. This is because it is assumed that the fuselage is not fully pressurized in the negative 2.0g hard landing load case.

2.3.2.1 Loading Profile

The loading profile for the fuselage structure includes the fuselage structural weight, the airplane payload weight, the front landing gear weight, and the empennage structural weight. It is assumed that the rear landing gear is mounted in the wing fuselage attachment and therefore the load is taken by structural loading points that are not sized in this model. The loading profile is illustrated in Figure 2.21.

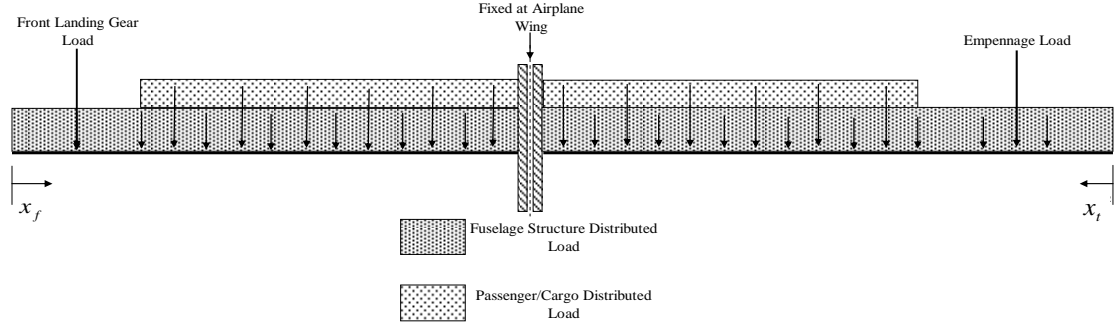


Figure 2.21: Fuselage Structure Loading Modeled as Cantilever Beam

The fuselage is modeled as two cantilever beams facing outwards, as shown in Figure 2.21, from the wing box quarter chord point. Modeling the fuselage as two cantilever beam is convenient because modeling it as one beam makes it an indeterminate problem. Each cantilever beam has its own coordinate reference system. x_f is the fuselage station coordinate starting at the nose of the fuselage and ending at the fuselage quarter chord. x_t is the coordinate originating from the tail of the airplane and ending at the wing box quarter chord point.

2.3.2.2 Internal Loading

For the loading given in Figure 2.21 the bottom of the fuselage is in compression which corresponds to a negative bending moment. With the sign convention in Equation 7 and 8, the coordinate system using x_f and x_t , a maximum positive shear, and minimum negative bending moment takes place at the wing box

quarter chord. The internal load distribution for load case 1 and 2 are given in Figures 2.22 and 2.23 respectively.

(7)

$$V_y(x) = \int -p(x)dx$$

(8)

$$\frac{\partial M_x}{\partial x} = -V_y$$

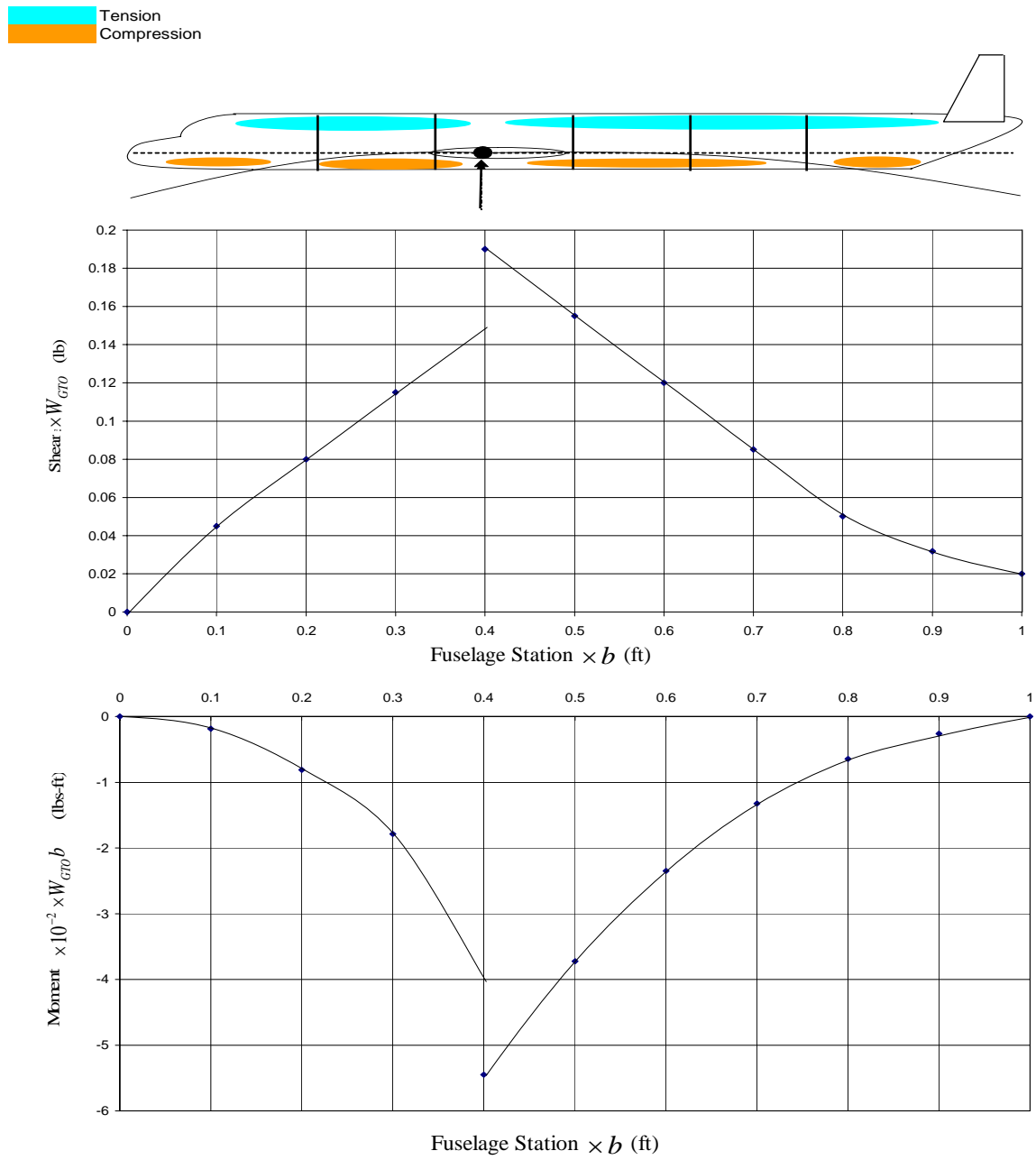


Figure 2.22: Shear and Moment Distribution for Fuselage Load Case 1 (Positive 2.5g Maneuver)

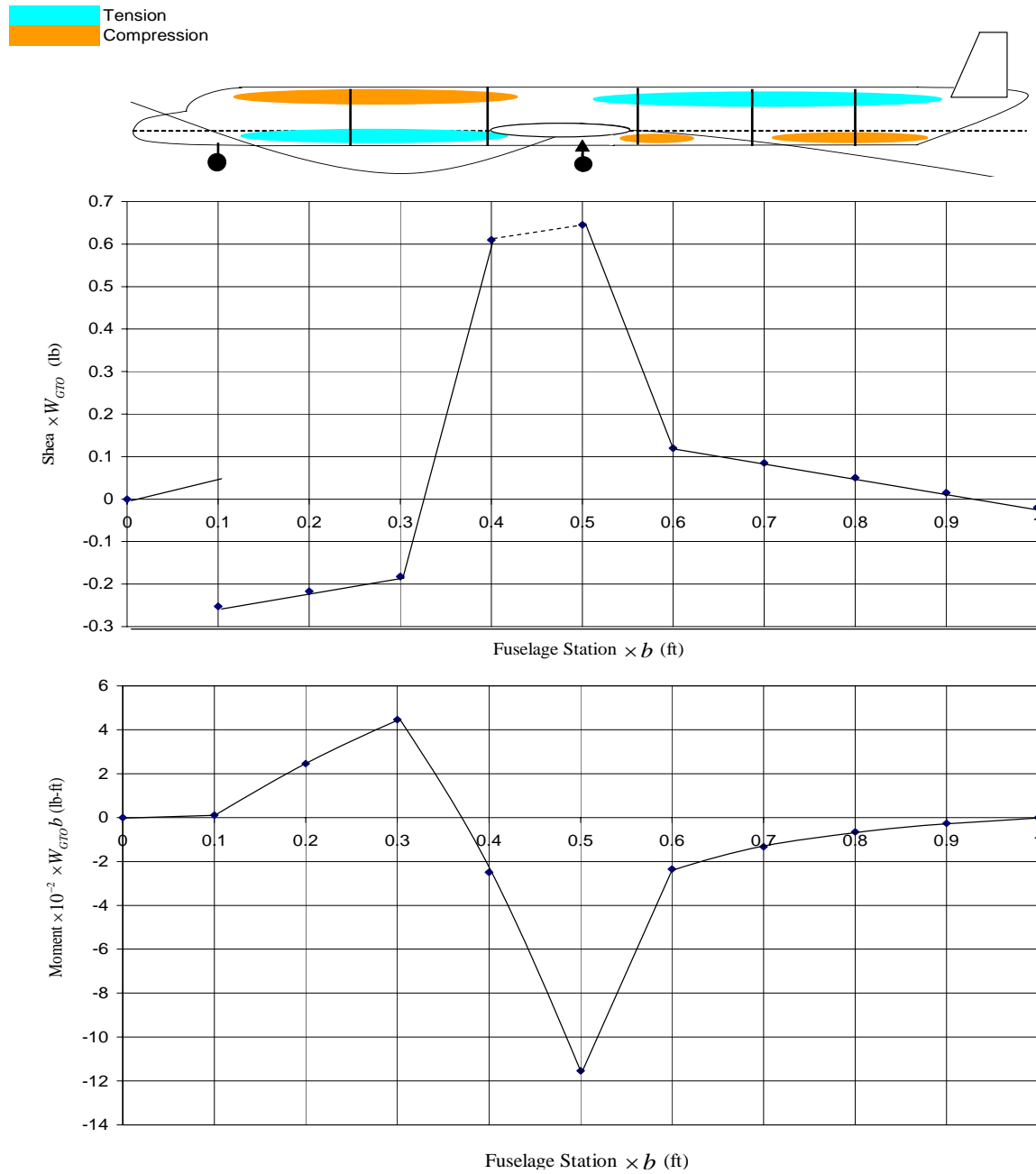


Figure 2.23: Shear and Moment Distribution for Fuselage Load Case 2 (Negative 2.0g Hard Landing)

The shear and moment distribution profiles are the same for the narrow and wide body, though they have different magnitudes and length of distributions. The maneuver load case has a maximum negative moment at the intersection of the rear fuselage and the wing box. The hard landing condition has a maximum negative moment at the rear landing gear and a maximum positive moment on the forward fuselage at the mid point between the front and rear landing gear.

2.3.2.3 Pressurization

The fuselage skin has a tensile stress from an ultimate pressurization load of 18 psi, applied to all fuselage cabin structure. The pressurization load is the same between the narrow and wide body aircraft, and also the same for the analysis of the CFRP and Aluminum Alloy materials.

2.4 *Stress Analysis*

2.4.1 **Thin Walled Idealized Beam Theory (Ref 2)**

The axial stress formula is given in Equation 9. M_z is the moment about the lateral axis. y_i is the discrete location of stress.

(9)

$$\sigma_x = \frac{-M_z(y_i - y_G)}{I_{zz}}$$

The Shear Flow and Shear Stress formula is given in Equation 10 and 11.

(10)

$$\Delta q = \frac{V_y Q_z}{I_{zz}},$$

(11)

$$\tau_{xy} = \frac{q_i}{t_i}$$

Q_z and I_z are the first and second moment of area respectively, and are given in Equation 12. The first and second moment of inertia using discrete areas is given in Equation 13.

(12)

$$Q_z = \iint_A y dA$$

$$I_z = \iint_A y^2 dA$$

(13)

$$Q_z = \sum_{i=1}^n A_i (y_i - y_G)$$

$$I_z = \sum_{i=1}^n A_i (y_i - y_G)^2$$

y_G is the lateral neutral axis (or y-component of the mass center) and its formula is given in Equation 14. The discretized calculation of the y-component of the centroid is also in Equation 14.

(14)

$$y_G = \frac{1}{A} \iint_A y dA = \frac{\sum_{i=1}^n A_i y_i}{\sum_{i=1}^n A_i}$$

2.4.2 Hoop and Longitudinal Stress (Ref 5)

The hoop stress is the circumferential stress in a pressure vessel wall. The longitudinal stress is parallel to the axis of symmetry in the pressure vessel wall. p is the pressure in psi. r is the radius of the pressure vessel. t is the thickness of the pressure vessel wall.

(15)

$$\sigma_{Hoop} = \frac{pr}{t}$$

$$\sigma_{Longitudinal} = \frac{pr}{2t}$$

2.4.3 Buckling Analysis

2.4.3.1 Compression Buckling

The buckling strength of a panel depends on thickness, width, stiffness, aspect ratio, Poisson's effects and the lay-up or bending stiffness matrix of the laminate.

Figure 2.24 shows the geometry and loads on individual panels of width b and length a that are used to determine buckling stability. Since the buckling strength for laminates depends on thickness and stacking sequence the flexural stiffness coefficients are used, referred to as the $[D]$ matrix. The $[D]$ matrix terms are used to calculate the buckling strength of a composite laminate in Equation 16.

\bar{N}_x is the critical running load in the laminate panel expressed in (lb/in.). m is the number of half sine waves formed by the buckled material. The value of m is chosen that gives the minimum buckling strength for a given aspect ratio.

(16)

$$\bar{N}_x = \frac{\pi^2}{b^2} \left[D_{11} m^2 \left(\frac{b}{a} \right)^2 + 2(D_{12} + 2D_{66}) + D_{22} \left(\frac{a}{b} \right)^2 \left(\frac{1}{m} \right)^2 \right]$$

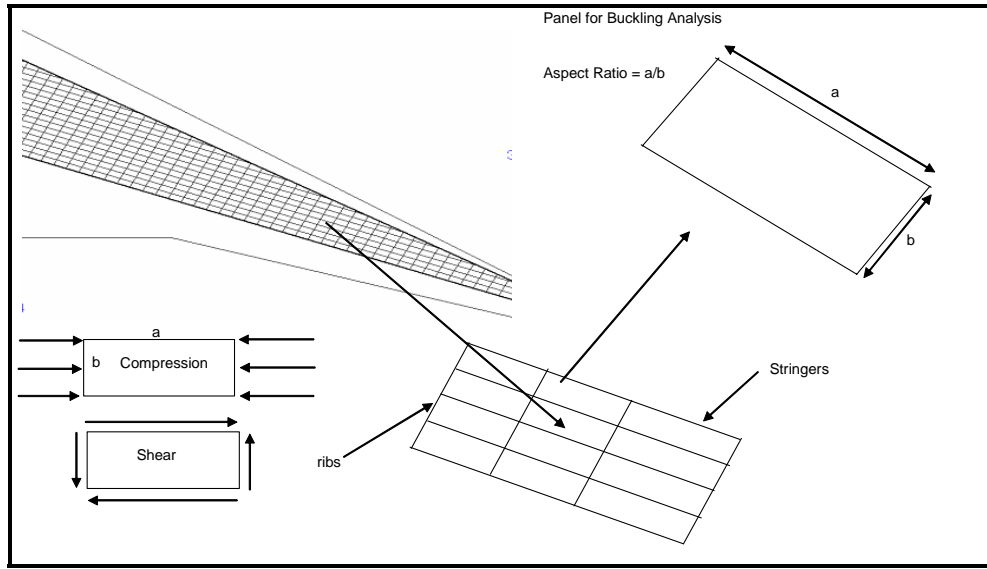


Figure 2.24: Stiffened Panels on the Wing Box Skin

Buckling of aluminum depends on thickness, width, stiffness, poisons ratio and aspect ratio. The equations to calculate buckling strength are for isotropic materials. The isotropic buckling equations are used to calculate the buckling strength of an Aluminum Alloy panel as shown in Equation 17, where E_c is the Elastic Modulus of the material in compression. The plot illustrating the K values for the compression and shear buckling are in Appendix C, Figure C.2.

(17)

$$\sigma_{cr} = C_c \frac{\pi^2 E_c}{12(1-\nu^2)} \left(\frac{t}{b} \right)^2 = K_c E_c \left(\frac{t}{b} \right)^2 \text{ where } K_c = f\left(\frac{a}{b} \right)$$

2.4.3.2 Shear Buckling

The shear buckling strength formula in Equation 18 is found in Reference 8 for a composite laminate. It is also a function of the flexure coefficients. This equation is derived assuming the long plate assumption which makes it a conservative shear buckling strength calculation for the geometry of the panels in this structure. K is a parameter that accounts for bend-twist coupling in the stability of a laminate.

(18)

$$K = \frac{D_{12} + 2D_{66}}{\sqrt{D_{11}D_{22}}}$$

$$N_{xy} = \frac{4}{b^2} \sqrt[4]{D_{11}D_{22}^3} (8.125 + 5.045K) \text{ when } K \leq 1$$

$$N_{xy} = \frac{4}{b^2} \sqrt[4]{D_{22}(D_{12} + 2D_{66})} \left(11.71 + \frac{1.46}{K^2} \right) \text{ when } K < 1$$

In Equation 19 the shear buckling strength τ_{cr} , for the isotropic Aluminum Alloy, is a function of axial Elastic Modulus E . Equation 19 uses the Elastic Modulus rather than the shear modulus, because pure shear produces equal compressive and tensile principal stresses on the diagonal plane with respect to the edge of the plate. The concept of pure shear as diagonal principal stresses is displayed in Figure 2.25 (Ref 2).

(19)

$$\tau_{cr} = C_s \frac{\pi^2 E_c}{12(1-\nu^2)} \left(\frac{t}{b} \right)^2 = K_s E_c \left(\frac{t}{b} \right)^2 \text{ where } K_s = f \left(\frac{a}{b} \right)$$

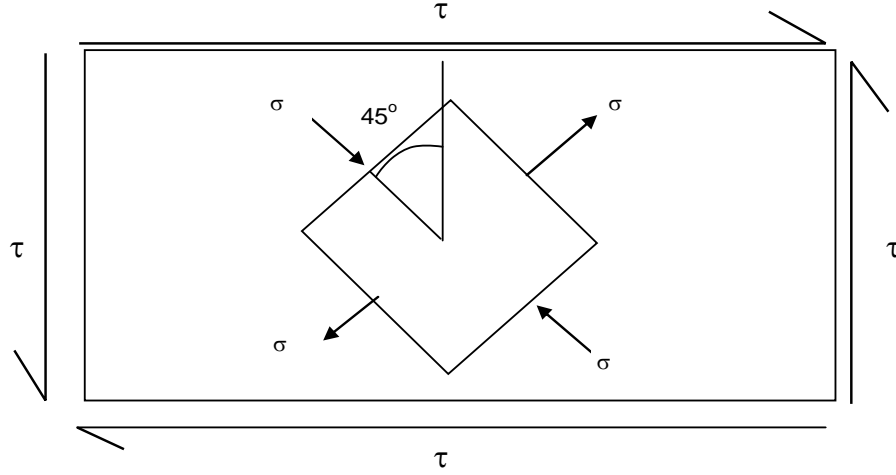


Figure 2.25: Principal Stress Components of Pure Shear Buckling (Ref 2)

2.4.3.3 Bending Buckling

The bending buckling strength formula, Equation 20, for a composite laminate is found in Reference 8. Like the shear buckling equation for composite laminate, Equation 20 assumes the long plate assumption.

(20)

$$N_x = \frac{\pi^2}{b^2} \left[13.9 \sqrt{D_{11} D_{22}} + 11.1 (D_{12} + 2D_{66}) \right]$$

The bending buckling allowable, used for the Aluminum Alloy, is found using Equation 21 (Ref 7). The buckling coefficient k_b is found from Figure C5.15 from Reference 7. The Elastic Modulus for Compression $E = E_c$ is used for Aluminum Alloy in Equation 21. Bending buckling is illustrated, in Figure 2.26, where w is the deflection of the web. Buckling, in Figure 2.26, is positive for “out of the page” and negative for “in the page”.

(21)

$$\sigma_b = k_b \frac{\pi^2 E_c}{12(1-\nu^2)} \left(\frac{t}{b} \right)^2$$

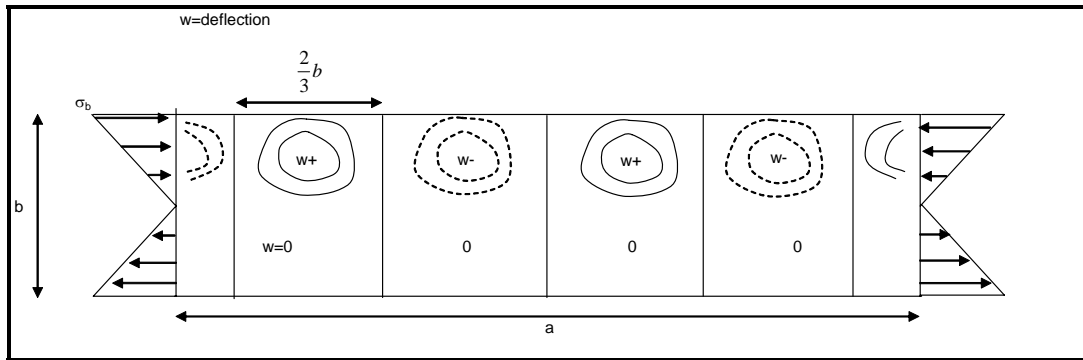


Figure 2.26: Bending Buckling Illustration (Ref 7)

2.4.3.4 Compression-Shear Interaction

To determine the compression and shear buckling interaction the following ratios are defined in Equation 22. The margin of safety for this buckling interaction is defined in Equation 23 and is displayed in Figure 2.27 for a margin of safety of zero. The critical compression ratio R_L for axial stress is negative if the axial stress is in tension and positive if in compression. If R_L is negative it helps prohibit shear buckling, therefore increasing the buckling stability in Equation 23.

(22)

$$R_L = \frac{\sigma_x}{\sigma_{Cr}}$$

$$R_S = \frac{\tau_x}{\tau_{Cr}}$$

(Note: RL is negative for tension)

(23)

$$M.S. = \frac{2}{R_L + \sqrt{R_L^2 + 4R_S^2}} - 1$$

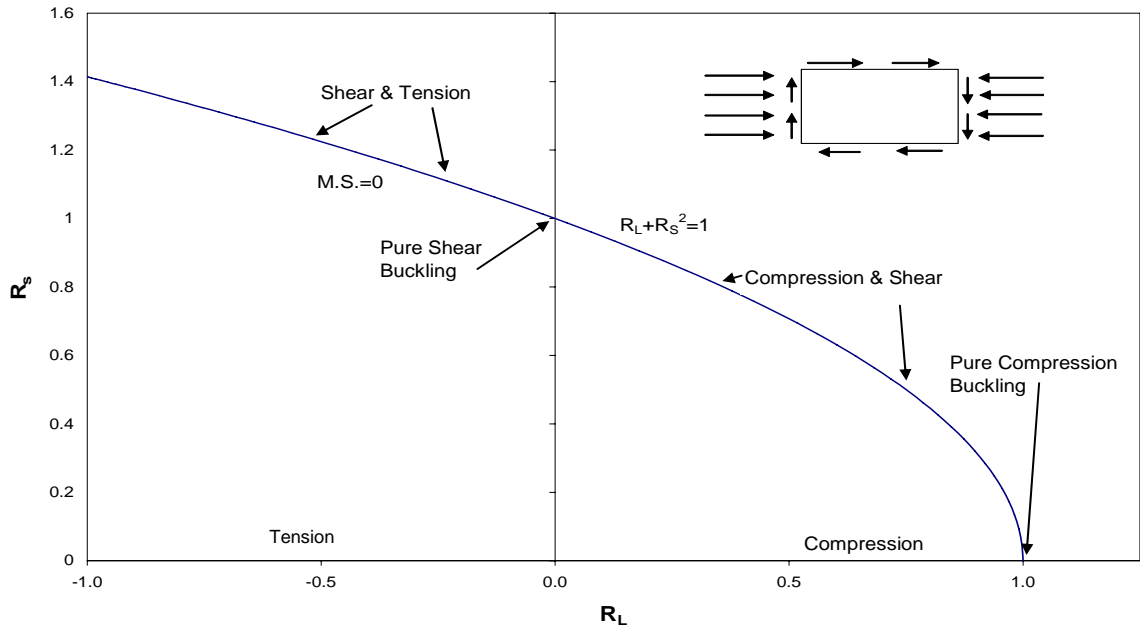


Figure 2.27: Compression Shear Buckling Interaction (Ref 7)

2.4.3.5 Shear-Bending Interaction

The shear-bending buckling interaction formula uses the ratios presented in Equation 24 and 25. The ratios include: the shear stress τ_{xy} and shear buckling strength τ_{cr} ratio. The bending axial stress on a web σ_{x_b} , shown in Figure 2.25, and the bending strength σ_{cr_b} ratio. The ratios in Equation 24 are used in Equation 25 to determine shear-bending buckling failure.

(24)

$$R_s = \frac{\tau_{xy}}{\tau_{cr}}$$

$$R_b = \frac{\sigma_{x_b}}{\sigma_{cr_bending}}$$

(25)

$$M.S. = \frac{1}{\sqrt{R_s^2 + R_b^2}} - 1$$

2.4.3.6 Longitudinal Crippling of Stringers

2.4.3.6.1 CFRP

A method for determining the crippling allowables for a long slender plate is taken from Reference 4. “Tests conducted by Lockheed and McDonnell Douglas under their Independent Research Development (IRAD) programs have confirmed that more accurate buckling and crippling predictions may be obtained when the curves (for unidirectional material) are defined in terms of non-dimensional parameters (Ref 4).” These non-dimensional parameters are displayed in Equation 26. In the following equations and figures F_{cc} is the crippling stress, F_{cu} is the ultimate compression stress of the material, E_x is the in plane elastic modulus, E_y is the transverse elastic modulus, b is the width of the loaded edge of the panel, and t is the thickness of the stiffener.

(26)

$$\frac{F^{cc}}{F^{cu}} \frac{E_x}{\bar{E}} - \frac{b}{t} \frac{\bar{E}}{E_x} \sqrt{\frac{F_{cu}}{\sqrt{E_x E_y}}}$$

There are two curves provided in Reference 4 dealing with one edge free and no edge free crippling test results. These curves were generated with unidirectional tape data from the following carbon fiber types:

-IM7/5250-4 Data

-IM8/HTA Data

-Crad AS/3501-6 Data

The one edge free crippling curve is displayed in Figure 2.28. The no edge free crippling curve is given in Figure 2.29.

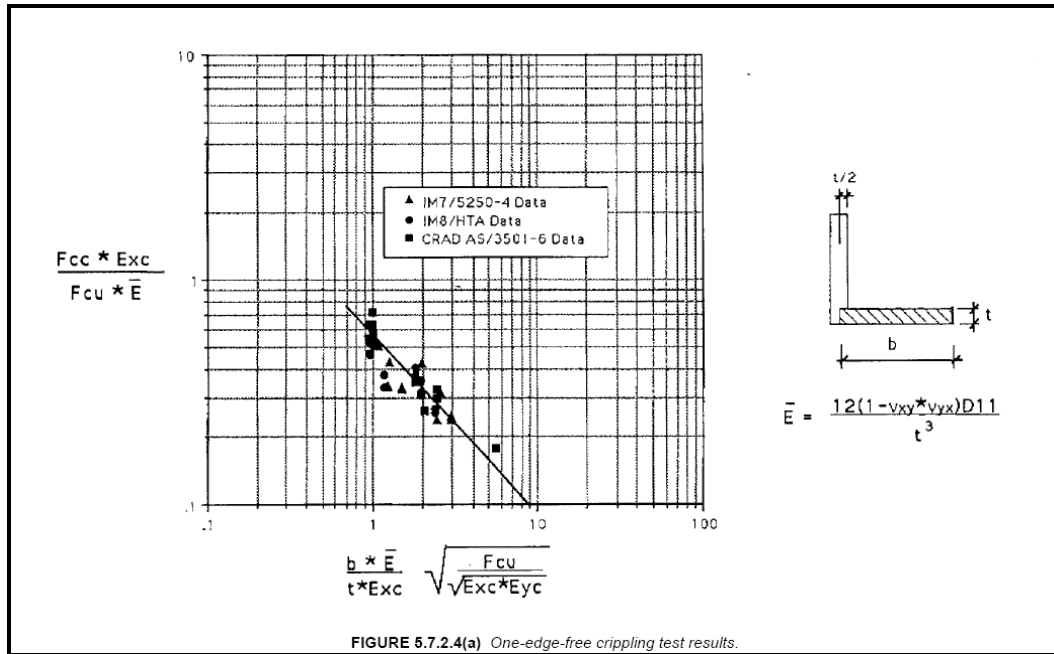


Figure 2.28: One Edge Free Crippling (logarithmic scale) (Ref 4)

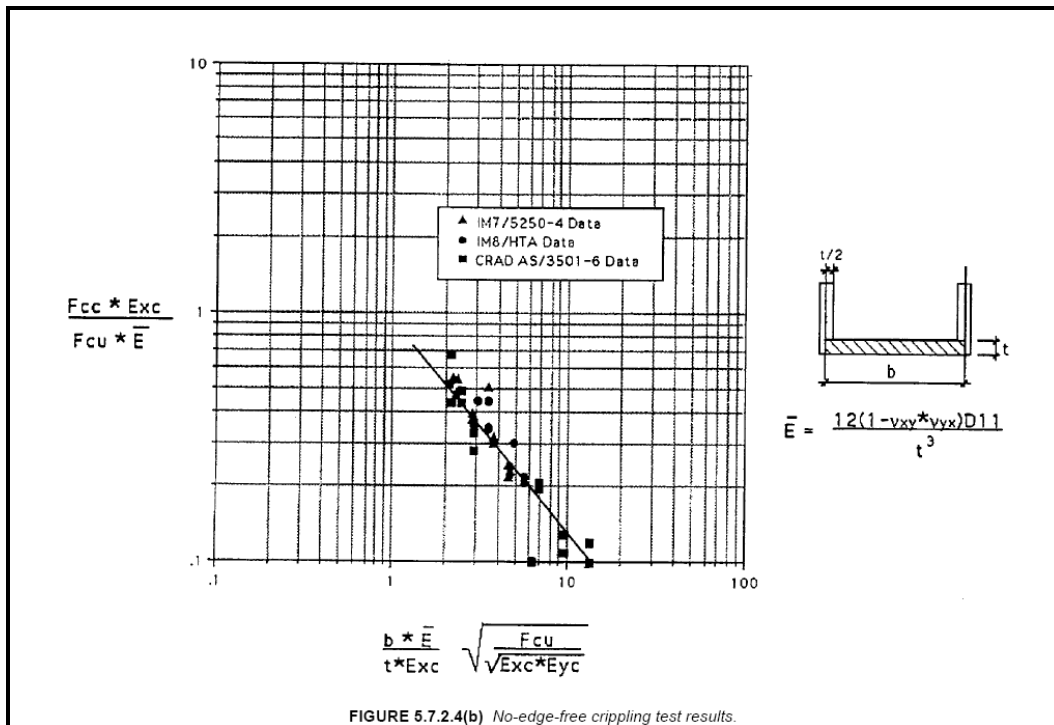


Figure 2.29: No Edge Free Crippling (logarithmic scale) (Ref 4)

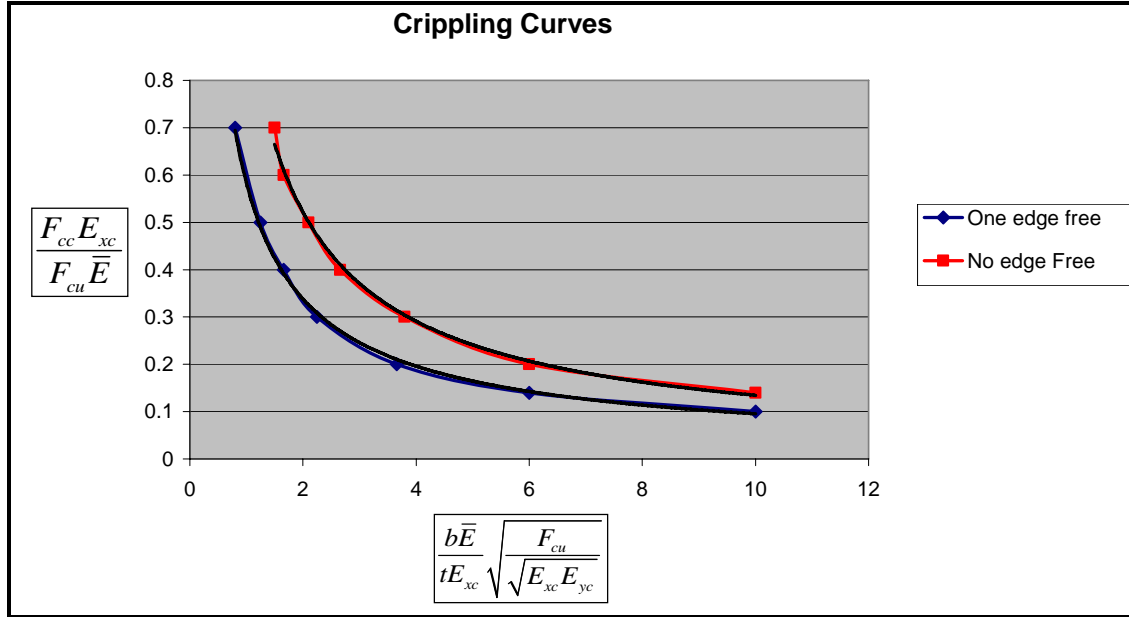


Figure 2.30: Crippling Curves

The trend line points were taken from Figure 2.28 and 2.29, written down by hand, and were plotted on a linear scaled graph presented in Figure 2.30. Equation 27 is used to determine the crippling strength for a one edge free or no edge free long plate. These equations were formulated by adding trend lines to the curves in Figure 2.30. Each cap of the stringer in the “I”-section of the wing is modeled as two long plates with one edge free and one edge fixed. The web of the stringer is modeled as one long plate with both edges fixed. The spar caps are modeled as two long plates with one edge free and one edge fixed. The crippling curves are for one edge free (OEF) and no edge free (NEF) long slender panels.

The fuselage “Hat”-section cap has one cap plate, two webs, and two flanges as shown in Figure 2.9. The cap is modeled as a long slender plate with both edges clamped, the webs modeled with both edges clamped, and the flanges with only one edge clamped. The radius of the curved geometry between the plates is neglected in the crippling analysis.

(27)

$$\frac{F^{cc}}{F^{cu}} \frac{E_x}{\bar{E}} (OEF) = 0.5832 \left(\frac{b}{t} \frac{\bar{E}}{E_x} \sqrt{\frac{F_{cu}}{\sqrt{E_x E_y}}} \right)^{-0.786}$$

$$\frac{F^{cc}}{F^{cu}} \frac{E_x}{\bar{E}} (NEF) = 0.9356 \left(\frac{b}{t} \frac{\bar{E}}{E_x} \sqrt{\frac{F_{cu}}{\sqrt{E_x E_y}}} \right)^{-0.842}$$

where

$$\bar{E} = \frac{12(1 - \nu_{xy}^2) D_{11}}{t^3}$$

2.4.3.6.2 Aluminum

Equation 28 is used to calculate the crippling strength of the Aluminum Alloy Columns. σ_{cy} is the compressive yield strength. There is a specified cutoff stress for 7075-T3 Aluminum Alloy given in Equation 29. The cutoff stress is used as the crippling strength of the column in the case where the calculated crippling strength from Equation 28 exceeds the cutoff stress in Equation 29.

(28)

$$\frac{\sigma_{cc}}{\sigma_{cy}}(OEF) = 0.546 \left(\frac{b}{t} \sqrt{\frac{\sigma_{cy}}{E_c}} \right)^{-0.8}$$

$$\frac{\sigma_{cc}}{\sigma_{cy}}(NEF) = 1.34 \left(\frac{b}{t} \sqrt{\frac{\sigma_{cy}}{E_c}} \right)^{-0.8} \quad (\text{Ref 2})$$

(29)

$$\sigma_{co} = 1.075 \sigma_{cy} \quad (\text{Ref 2})$$

2.4.3.7 Effective Width

The concept of effective width is used in determining the buckling stability of a stiffened panel. The formula used to determine effective width is given in Equation 30. The effective width is used to determine the amount of skin area that shares the same stress as the stiffener before the stiffener buckles. Therefore it is used in conjunction with Euler column buckling to determine the global buckling strength of the stiffeners. Figure 2.31 illustrates the concept of effective width. $K = 0.85$ is used when both edges of the skin is clamped. A plot used to determine the radius of gyration for a given effective width contribution is given in Appendix B, Figure B.5.

(30)

$$w_e = t_{skin} K \frac{E_{skin}}{\sqrt{E_{stiffener}}} \sqrt{\frac{1}{\sigma_{skin}}} \quad (\text{Ref 2})$$

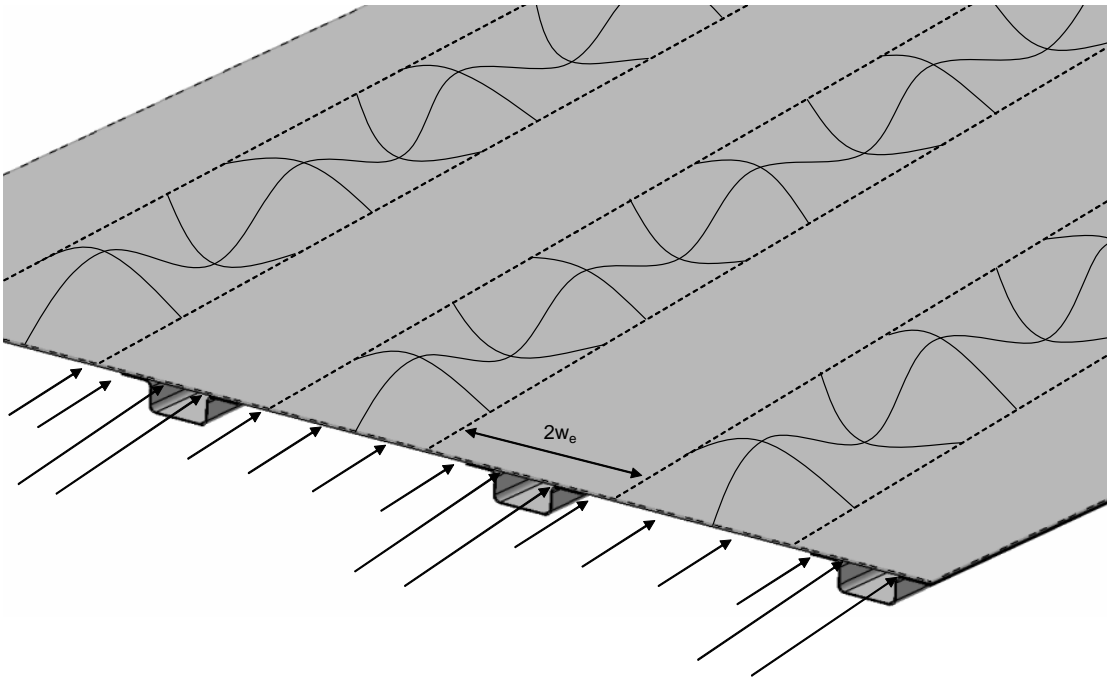


Figure 2.31: Skin Buckled Stiffened Panel and Effective Width Illustration

2.4.3.8 Euler Column Buckling

Equation 31 is used to determine Euler Column Buckling strength. L_e is the effective length, ρ is the radius of gyration, and the ratio of the two is the slenderness ratio. If the slenderness ratio is below a critical value displayed in

Equation 31 than inelastic buckling occurs; if the slenderness ratio is above the critical value than the buckling is elastic. The inelastic portion is referred to as the Johnson Curve, and the Elastic the as Euler curve. The Elastic Modulus in Equation 31 corresponds to that of the stringer material. There is a Johnson and Euler Column Curve illustrated in Figure B.4 in Appendix B.

(31)

$$\left. \frac{L_e}{\rho} \right)_{crit} = \pi \sqrt{\frac{2}{\sigma_{cc}/E}}$$

$$\sigma_{cr} = \sigma_{cc} \left[1 - \frac{1}{4\pi^2} \frac{\sigma_{cc}}{E} \left(\frac{L_e}{\rho} \right)^2 \right] \text{ for } \frac{L_e}{\rho} < \left. \frac{L_e}{\rho} \right)_{crit}$$

$$\sigma_{cr} = \frac{\pi^2 E}{(L_e/\rho)^2} \text{ for } \frac{L_e}{\rho} > \left. \frac{L_e}{\rho} \right)_{crit}$$

2.5 Materials

Two materials are selected to be representative for this comparison. The composite lamina properties are taken from Reference 4. The lamina and laminate tension ultimate, and open hole strengths, are adjusted to mimic the tension compression strength ratio's that are currently being used in the commercial industry.

2.5.1 CFRP

Table 2.12: CFRP Lamina Properties

E_1	25	Msi	α_1	0.3	$\mu\epsilon/C^\circ$
E_2	1.7	Msi	α_2	19.5	$\mu\epsilon/C^\circ$
G_{12}	0.65	Msi			
ν	0.31				
ρ	0.056	lb/in ³			
F_{1tu}	165	ksi	F_{1cu}	110	ksi
F_{2tu}	4	ksi	F_{2cu}	20	ksi
F_{12su}	9	ksi			
V_f	0.6		t_p	0.0052	in

Table 2.13: CFRP Laminate Properties

[25/50/25]					
E_x	9.4	Msi			
E_y	9.4	Msi			
ν_{xy}	0.32				
σ_{tu}	60	ksi	σ_{oht}	48	ksi
σ_{cu}	40	ksi	σ_{ohc}	27	ksi
τ_{su}	24	ksi			

[50/40/10]					
E_x	14.5	Msi			
E_y	5.9	Msi			
ν_{xy}	0.30				
σ_{tu}	96	ksi	σ_{oht}	77	ksi
σ_{cu}	64	ksi	σ_{ohc}	43	ksi
τ_{su}	24	ksi			

[10/80/10]					
E_x	5.8	Msi			
E_y	5.8	Msi			
ν_{xy}	0.59				
σ_{tu}	38	ksi	σ_{oht}	30	ksi
σ_{cu}	25	ksi	σ_{ohc}	17	ksi
τ_{su}	36	ksi			

2.5.2 CFRP Lamination Scheme of Aircraft Structure

The laminate families chosen for the sub-structure are those that are currently being used in the medium jet transport commercial industry. The actual laminate for the stringers is not [50/40/10] but rather quasi-isotropic and capped with uni-directional zero lamina plies. When a weighted average of the stiffness of the stringer

material is taken it is similar, though a little larger, than the skin. For simplicity the stringer family is assumed to be that of the skin.

The laminate families for the wing structure are:

Wing

Skin-50/40/10

Stringers-50/40/10

Spar Caps-10/80/10

Spar Webs-10/80/10

Ribs (not of significance in this analysis)

*The rib spacing is analogous to the stiffened panel length presented in section 2.2.1 (wing). The rib spacing is a multiple of the stringers spacing and is maintained a constant to what is being used in industry.

The laminate families for the fuselage structure are:

Fuselage

Skin-25/50/25

Stringers-25/50/25

Frames (not of significance in this analysis)

*The frame spacing is analogous to the stiffened panel length presented in section 2.2.2 (fuselage). The frame spacing is a multiple of the stiffener spacing and is maintained a constant to what is being used in industry.

The minimum gauge for the quasi-isotropic laminate is 0.055 in. This is the minimum gauge value used in industry, therefore the ply thickness is scaled from this value to determine buildable laminate thicknesses. The minimum gauge laminate thickness corresponds to a ply value of 0.0068 in., different from the ply value used to determine laminate mechanical properties displayed in Table 2.12.

2.5.3 Aluminum

The Aluminum Alloy used in this comparison is 7075-T6 sheet properties. The same mechanical properties are used for the sheets and longitudinal extrusions, which actually have slightly different property values. 7075-T6 Aluminum Alloy is normally used in compression critical areas like the belly of the fuselage and the top of the wing. The Aluminum Alloy does not have good toughness and damage tolerant properties. The material properties of 7075-T6 Aluminum Alloy sheet are given in Table 2.14.

Table 2.14: 7075-T6 Aluminum Alloy Properties

Alloy	Current
Yield Strength (ksi)	71
Ultimate Strength (ksi)	80
Fatigue Strength (ksi)	23.7
Elastic Modulus (msi)	10.5
Shear Modulus (msi)	3.9
Shear Stregth (ksi)	48

The fatigue strength for the 7075 Aluminum Alloy is defined as the detail fatigue rating for a Class 1 Notch with a stress ratio of $R = 0.06$ at 100,000 cycles. The fatigue strength of 24 ksi is used as an estimate based on one third of the yield stress. The fatigue strength is the same for all tension critical sections of the aircraft except for fuselage section tension critical from load case 2 (negative 2.0g Hard Landing). The yield strength in Table 2.14 refers to compression yield strength and the ultimate strength corresponds to ultimate tension strength. The density of 7075-T6 is 0.101 lb/in³.

2.5.4 Material Enhancement Analysis Cases

Each material case is an enhancement of the baseline material. The percent enhancement is chosen based on the feasibility of the enhancement in industry. Technically this is not a sensitivity study because the percent enhancements are not adjusted to give the same unit change in thickness Δt of the structure. A sensitivity study would give better weight or volume estimates of the structure that is governed

by a certain failure mode. Listed below are the material enhancements for this comparison.

CFRP

Improved Composite

+25% OHC

+25% OHT

+50% Elastic Modulus

Aluminum

Advanced Alloy

+10% Elastic Modulus

+50% Fatigue Limit

+100% Fatigue Limit

2.6 *Failure Modes and Criteria*

2.6.1 **CFRP**

2.6.1.1 Wing

There is a stiffness redistribution factor applied to the directionalized wing skin. Since the wing box sub-structures are different families of laminates they have different Modulus of Elasticity. For example the [50/40/10] wing skin will take more loading from wing flexure than the [10/80/10] spar caps. The wing skin has more fiber lamina with zero orientation in the plane of the wing flexure load and therefore has a larger stiffness in that direction. The stress transformation factor was found in Reference 5. The equations and illustrations of the load redistribution are given in Appendix C, Figure C.3.

2.6.1.1.1 *Fracture*

The Ultimate Tension and Compression Fracture Strength used for the current composite material and for three improved material cases for Quasi-Isotropic material is given in Table 2.13. Fracture takes place at ultimate load for all sub-structure. Ultimate load is the limit or design load multiplied by a safety factor of 1.5. Equation 32 shows the margin of safety used to size the structure. The margin of safety must be greater than or equal to zero. In the enhancement analysis cases it should be noted that although the OHC fracture strength is larger for the case of improved composite

1, the compression ultimate allowable is not changed, this is also true for OHT. The failure criteria for the CFRP laminate wing structure:

- 1) Open Hole Compression (OHC) of skin and spar caps at ultimate load.
- 2) Open Hole Tension (OHT) of skin and spar caps at ultimate load.
- 3) Tension ultimate of stringers at ultimate load.
- 4) Compression ultimate of stringers at ultimate load.
- 5) Shear ultimate of spar web at ultimate load.

(32)

$$M.S._{Fracture} = \frac{\sigma_{Fracture_Allowable}}{1.5\sigma_{Limit}} - 1 \geq 0$$

2.6.1.1.2 Buckling

- 1) Compression buckling of stringers at ultimate load.
- 2) Compression crippling of spar caps at ultimate load.
- 3) Combined compression and shear buckling of skin at ultimate load.
- 4) Combined shear and bending buckling of spar webs at ultimate load.

2.6.1.2 Fuselage

2.6.1.2.1 Fracture

- 1) Open Hole Compression OHC fracture at limit load (when the minimum principal stress in the skin σ_2 exceeds the open hole compression strength of the material).
- 2) Open Hole Tension fracture OHT at limit load (when the maximum principal stress in the skin σ_1 exceeds the open hole tension strength).
- 3) Ultimate shear fracture at ultimate load (where the maximum shear stress τ_{\max} exceeds the shear strength of the skin material)
- 4) Ultimate tension fracture at ultimate load (when axial tension stress $\sigma_{x(+)}$ exceeds the tensile strength of the stringer material)
- 5) Ultimate compression fracture at ultimate load (when the axial compressive stress $\sigma_{x(-)}$ exceeds the compressive strength of the material)

2.6.1.2.2 Buckling

- 1) Buckling from combined shear and compression at limit load (when the axial compression stress $\sigma_{x(-)}$ and the shear stress τ_{xy} interacts and makes the skin unstable)
- 2) Buckling from combined shear and tension at limit load (when axial tension stress $\sigma_{x(+)}$ and shear stress τ_{xy} interact and the skin becomes unstable)

- 3) Compression Buckling/Crippling at ultimate load (when the axial compression stress $\sigma_{x(-)}$ exceeds the value at which the stringer integrated stiffened panel becomes unstable)

2.6.2 Aluminum Alloy

Additional Aluminum Alloy properties are given in Appendix C, Figure C.1.

Aluminum Failure modes are the same for both wing and fuselage.

2.6.2.1 Fracture

- 1) Compression yield of skin, stringers, spar caps at ultimate load.
- 2) Tensile ultimate of skin, stringers, spar caps at ultimate load.
- 3) Shear ultimate of skin and spar web at ultimate load.

2.6.2.2 Buckling

- 1) Compression buckling of stringers at ultimate load.
- 2) Compression crippling of spar cap at ultimate load.
- 3) Combined compression and shear buckling of skin at ultimate load.
- 4) Combined shear and bending buckling of spar webs at ultimate load.

2.6.2.3 Fatigue

- 1) Fatigue from tension of skin, stringers, and spar caps at limit load, for both load cases.

2.7 Optimization

2.7.1 Optimized Variables

2.7.1.1 Wing

Optimized variables include the thickness of all substructures such as:

- 1) Skin thickness (top and bottom)
- 2) Spar web thickness (forward and aft)
- 3) Spar cap thickness (forward and aft)
- 4) Stringer cap/web thickness (top and bottom)

2.7.1.2 Fuselage

- 1) Skin thickness (top and bottom)
- 2) Stringer cap/web/flange thickness

2.7.2 Fixed Variables

- 1) All material properties are fixed.
 - 2) The configuration geometry is fixed (i.e. stiffener spacing and widths of stiffener cross section)
- * The structural configuration geometry is fixed because otherwise the optimization would be under-constrained.

2.7.2.1 Wing

Fixed variables for geometry of the wing box substructure:

- 1) Skin width or wing box width (top and bottom)
- 2) Spar web width or wing box height (forward and aft)
- 3) Spar cap width (forward and aft)
- 4) Stringer width (top and bottom)
- 5) Stringer height (top and bottom)
- 6) Stringer Spacing
- 7) Frame Spacing
- 8) Stringer Geometry

2.7.2.2 Fuselage

Fixed variables fuselage structure:

- 1) Fuselage Diameter
- 2) Fuselage Length
- 3) Stinger Spacing
- 4) Frame Spacing
- 5) Stringer Geometry

2.7.3 Concept of Minimum Gauge

Minimum gauge is the minimum skin thickness for the fuselage that is driven by a default requirement. The minimum skin thickness is maintained when there is no critical structural requirement that drives the skin thickness. Default requirements that determine minimum gauge can consist of:

- 1) Structural integrity after impact
- 2) Lightning strike
- 3) Pressurization (or pillowing)
- 4) Manufacturability

In this study the Minimum Gauge is 0.055 in. which is the thinnest Quasi-Isotropic ([25/50/25]) laminate that can be manufactured.

2.7.4 Discretization

Figure 2.35 illustrates the sequence of the methodology in the calculation process. Figure 2.35 also shows and defines the input parameters for each function in the methodology. This is an iterative calculation process, therefore the flow chart represents an iteration starting from the initial thickness and finishing with the optimized thickness. The optimized thickness is then put in as the initial thickness for the next iteration.

2.7.4.1 Geometry and Cross Sectional Area Distribution

The structure is broken up into sections with “lumped” area a_i . The areas are referred to as “lumped” because they include the cross sectional area of the skin and stringers for the i^{th} section. t is an array of the thicknesses of the structure to be optimized. b_i is a $n \times 1$ array of the widths of each i^{th} panel for a total of n panels for the stringers. For example an “I-section stringer” has three panels consisting of two caps and a web. The input parameters for the area distribution of the wing are given in Equation 33 and for the fuselage, Equation 34. h and w correspond to the wing box height and width respectively. D is the fuselage diameter. Figure 2.32 gives an example of how the area of the wing box is implemented as an area distribution in MATLAB.

(33)

$$\begin{aligned} a_i &= a(h, w, t, b_i) \\ y_i &= y(h, w, a_i) \end{aligned}$$

(34)

$$\begin{aligned} a_i &= a(D, t, b_i) \\ y_i &= y(D) \end{aligned}$$

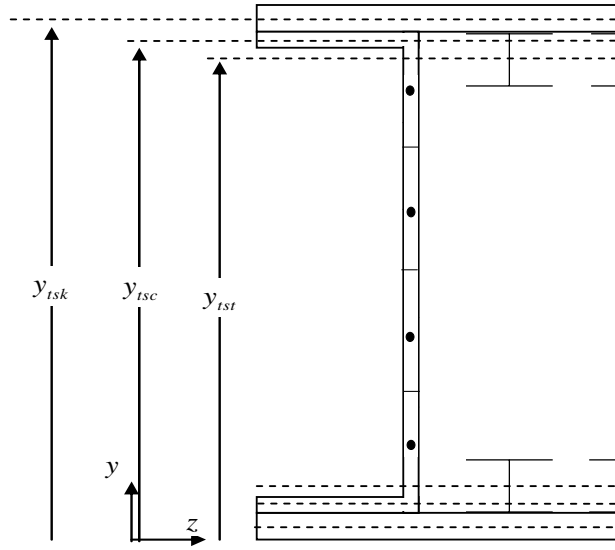


Figure 2.32: Lumping Areas on the Wing Box

Once the lateral area distribution is known the center of area y_G (or referred to as center of mass) and the second moment of area I_z are calculated. The input parameters for this calculation are given in Equation 35. The discretized formulas in Equation 14, section 2.4.1, are used to calculate the center of area and second moment of area.

(35)

$$y_G = y_G(a_i, y_i)$$

$$I_z = I(a_i, y_i, y_G)$$

2.7.4.2 Internal Loads

The internal loads are found using the maximum gross takeoff weight, geometry, and load cases from the wide body aircraft. This internal loading is scaled to the weight and geometry of the aircraft being analyzed. The input parameters for the internal loads on the aircraft structure are given in Equation 36. W_{GTO} is the maximum gross takeoff weight of the aircraft. L is the length of the structure (i.e. the span of the wing or length of the fuselage). n_z is the load factor for the specified load case where LC1 is load case 1 and LC2 is load case 2.

(36)

$$\begin{aligned} V_y &= V(W_{GTO}, L, n_{z_LC1}, n_{z_LC2}) \\ M_z &= M(W_{GTO}, L, n_{z_LC1}, n_{z_LC2}) \end{aligned}$$

2.7.4.3 Internal Stress

At this point in the method it is required that the user define material properties. E_{skin} and $E_{stringer}$ are applied to distinguish between the skin and the stringers, based on their material stiffness. This enables instances where the skin and stringers have different stiffness and therefore carry different axial stress.

The input parameters used to calculate internal stress are presented in Equation 37 and 38 for the wing and fuselage respectively. p is the internal cabin pressure. σ_{xi} is the axial stress in the i^{th} lumped area. σ_{yi} is the transverse stress, which is entirely from hoop stress due to pressurization. Axial tensile stress from pressurization is applied to sections in tension from bending, or that are not compression critical. q_i is the shear flow. τ_{xyi} is the shear stress. $\sigma_{1,2i}$ is the maximum and minimum principal stress.

(37)

$$\begin{aligned}\sigma_{xi} &= \sigma_x(M_z, I_z, y_i, y_G, E_{Skin}, E_{Stiff}, h, w, t) \\ q_i &= q(V_y, I_z, a_i, y_i) \\ \tau_{xyi} &= \tau_{xy}(q_i, t) \\ \sigma_{1,2i} &= \sigma_1(\sigma_{xi}, \sigma_{yi}, \tau_{xyi})\end{aligned}$$

(38)

$$\begin{aligned}
\sigma_{xi} &= \sigma_x(M_z, I_z, y_i, y_G, E_{Skin}, E_{Stiff}, P, D, t) \\
\sigma_{yi} &= \sigma_y(P, D, t) \\
q_i &= q(V_y, I_z, a_i, y_i) \\
\tau_{xyi} &= \tau_{xy}(q_i, t) \\
\sigma_{1,2i} &= \sigma_1(\sigma_{xi}, \sigma_{yi}, \tau_{xyi})
\end{aligned}$$

2.7.4.4 Buckling Stability

The material properties defined are now used to determine buckling stability. As described the fuselage is viewed as a series of flat stiffened panels around the circumference of a circle. ν is Poisson's ratio. b_p is the width of the stiffened panel. a_p is the length of the stiffened panel. y_{bi} is the local lateral position of each panel of the stiffener and is used to calculate the local second moment of area for the stringer cross section. The use of these parameters in determining the buckling stability is illustrated in Equation 39.

(39)

$$\begin{aligned}
\sigma_{Cr_Stiff} &= \sigma_{Stiff}(E_{Stiff}, E_{Skin}, b_i, y_{bi}, t) \\
\sigma_{Cr_Skin} &= \sigma_{Sk}(E_{Skin}, b_p, a_p, t, \sigma_{Cr_Stiff}, \nu) \\
\tau_{Cr_Skin} &= \tau_{Sk}(E_{Skin}, b_p, a_p, t, \nu)
\end{aligned}$$

2.7.4.5 Margins of Safety

All the information has been calculated to determine the margins of safety for each i^{th} lumped area. The margins of safety for fracture at limit and ultimate load, buckling at limit load and ultimate load for the wing, and fatigue at limit load are calculated. These margins of safety are stored in $n \times 1$ arrays. Since the load cases are laterally symmetric only the margins of safety along the lateral plane are necessary.

The fracture failure mode corresponds to Open Hole fracture for a quasi-isotropic composite at limit and the material ultimate fracture strength at ultimate load for aluminum. The buckling failure mode corresponds to thin plate buckling for the fuselage skin at limit and Euler beam elastic and inelastic buckling for the stringers at ultimate. The fatigue failure mode corresponds to Aluminum Alloy skin at limit load only.

The margins of safety now get filtered for the most critical one, for each failure mode, for the fuselage sections crown and belly. This is done because the margin of safety for the skin and stringers are applied to a variable constraint in the optimization. Each skin and stringer section has one linear and one non-linear constraint.

2.7.5 Optimization

The inputs used in the MATLAB formulated optimization function `fmincon` are illustrated in Equation 40. t' is the optimized thickness of the sub-structure.

(40)

$$t' = \text{fmincon} \left(f, [A], [UB], [LB], [C], t_0 \right)$$

2.7.5.1 Cost Function

f is the cost function which, like the non-linear inequality constraints, is defined as a separate MATLAB function of the optimized variable t . This is because any function where the first or second derivative is used by the optimization is required by MATLAB to be defined as a separate “called” function. The cost function is the function minimized during the optimization process. In this optimization the cost function is the total cross sectional area as a function of the skin and stringer thicknesses. The cross sectional area is used as the cost function because it is directly proportional to weight. In Equation 41 and 42 A is the area of the sub-structure.

(41)

$$A_{wing} = A_{skin} + A_{Stringers} + A_{Spar_Caps} + A_{Spar_Webs}$$

(42)

$$A_{fuselage} = A_{skin} + A_{Stringers}$$

2.7.5.2 Linear Inequality Constraints

Each fuselage sections margins of safety is filtered down to the most critical. This is applied to one linear and non-linear constraint for each variable in the thickness array t . The optimization starting position is t_0 and is the same as the initial thickness used to determine the initial margins of safety. The starting position of the optimization never changes only the constraints change. $[A]$ is a 4×4 matrix defining the linear inequality constraints of the optimization. The linear inequality constraints take the following form given in Equation 43. $\{b\}$ is the value that the inequality should not exceed.

(43)

$$[A] \leq \{b\}$$

It is more convenient to apply the margins of safeties directly to the constraints rather than deriving a constraint directly from the margin of safety equation and making it a function of thickness directly. A logical process of the application of the margins of safety to the constraints is described below. An example is presented using the Open Hole Compression (OHC) margin of safety for the quasi-isotropic skin material. t_{0i} is the initial thickness of the substructure. t_{fi} is the optimized thickness of the substructure. The OHC margin of safety is given in

Equation 44. The safety factor S.F. for the fuselage is 1.0 for the fuselage and 1.5 for the wing for OHC.

(44)

$$M.S. = \frac{\sigma_{OHC}}{(S.F.)\sigma_2} - 1$$

If the $M.S. < 0$ then the minimum principal stress of the skin is larger in magnitude than the open hole compression strength of the skin material, so the skin fails. Therefore the skin needs to become thicker. Axial stress is inversely related to second moment of area (i.e. $\sigma_x = -Mc/I$). The second moment of area is linearly related to thickness (i.e. $I = \pi D^3 t / 8$, for a thin walled cylinder). Therefore axial stress is inversely related to thickness. Assume we have an initial margin of safety of $M.S._0 < 0$. At what thickness increase would it take to make the margins of safety larger than or equal to zero. From the relationships established above the required thickness can be approximated from Equation 45. The general relationship between axial stress and skin thickness is presented in Figure 2.33.

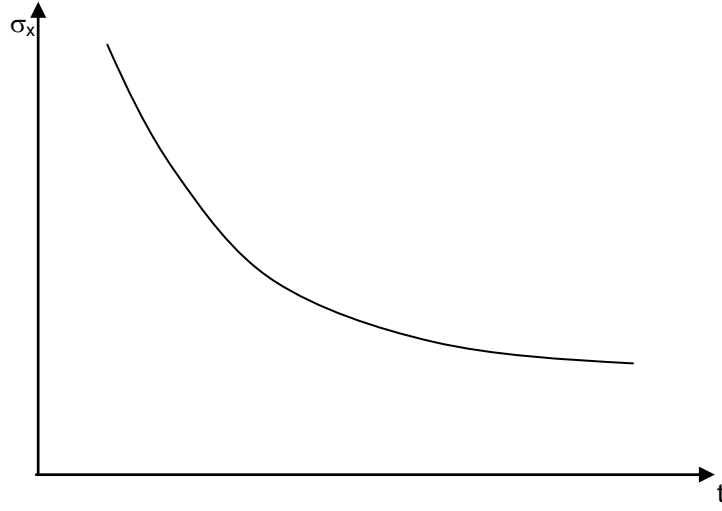


Figure 2.33:Generic Axial Stress and Skin Thickness Relationship

(45)

$$M.S._f = \frac{\sigma_{OHC}}{\sigma_2} \frac{t_{fi}}{t_{0i}} - 1 \geq 0$$

Where the optimized thickness $t_{fi} > t_{0i}$. The linear fracture constraint, with OHC as the critical failure mode, is given in Equation 46. A similar constraint formulation is valid for stringer ultimate tensile or compression failure.

(46)

$$g(x)_{Linear} = 1 - (M.S._0 + 1) \frac{t_{fi}}{t_{0i}} \leq 0$$

2.7.5.3 Non-linear Inequality Constraints

$[C]$ is the non-linear inequality constraint which is actually defined, like the cost function, as a separate MATLAB function. The variable being optimized, in this case t , is an input parameter. The non-linear inequality constraints have to be equal to or less than zero.

(47)

$$[C] \leq 0$$

The buckling margin of safety combines compression and shear buckling effects. The compression and shear buckling stability varies with the skin or web thickness squared (i.e. $\sigma_{cr}, \tau_{cr} = const \times t^2$). The relationship between actual axial stress and thickness is also combined to give the cubic relationship in Equation 48. The nonlinear constraint is constructed using the same logical method as the linear constraint. A generic plot illustrating how axial stress and buckling stability vary with skin or web thickness is given in Figure 2.34.

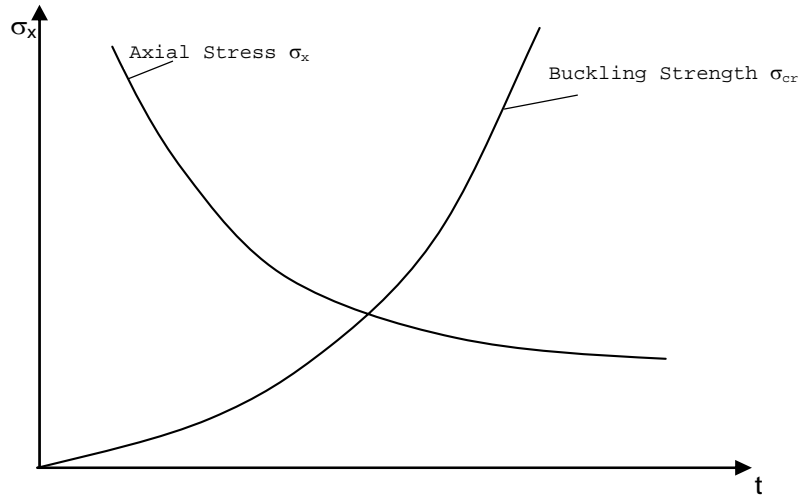


Figure 2.34: Generic Buckling Stability and Axial Stress vs Skin Thickness Relationship

(48)

$$g(x)_{non-linear} = 1 - (M.S._0 + 1) \frac{t_{fi}^3}{t_{0i}^3} \leq 0$$

Stringer buckling is a methodical procedure. Therefore, the buckling stability of a stringer or spar cap does not have an as apparent relationship to flange and web thickness, as it has for the skin thickness. Through a trial and error process the non-linear buckling constraint of the stringers yields the following relationship in Equation 49. This relationship was found by arbitrarily changing the exponent of the thickness ratio until the stringers thickness converged to a margin of safety of zero.

(49)

$$g(x)_{non-linear} = 1 - (M.S._0 + 1) \sqrt{\frac{t_{fi}}{t_{0i}}} \leq 0$$

There are no equality constraints used in this optimization.

2.7.5.4 Upper and Lower Boundaries

$[UB]$ and $[LB]$ are the upper and lower bound limits respectively. The optimized variable cannot exceed the upper bound limit values and cannot fall below the lower bound limit values. The lower bound limit is useful for enforcing minimum gauge requirement.

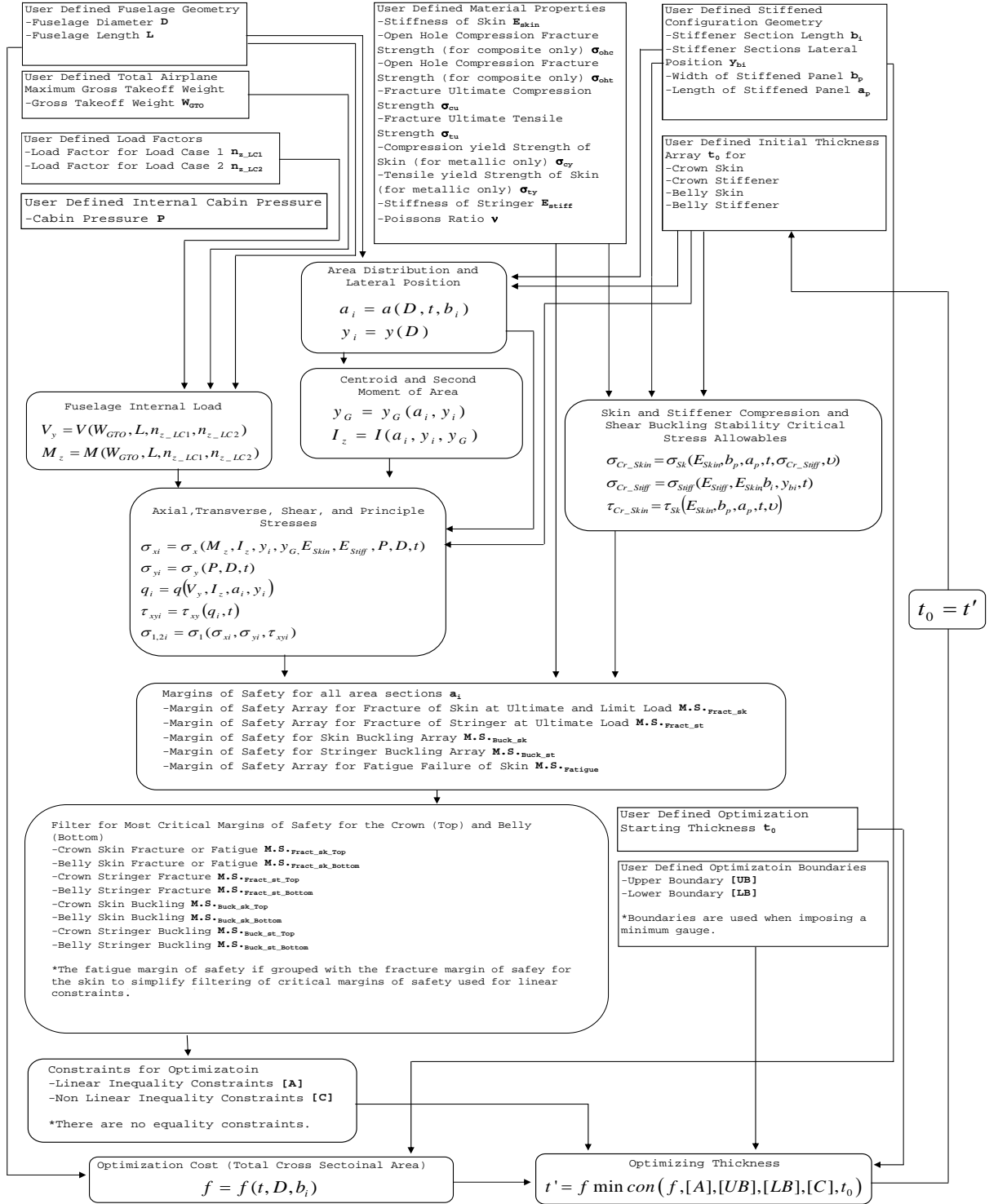


Figure 2.35: Optimization Flow Chart (example for fuselage)

3 Verification

3.1 Regression Analysis

Reference 1 takes a regression approach to verify the load bearing weight calculation of their model. Reference 1 breaks down the structural weight into three categories: load bearing, primary, and total structural weight. The substructure included in these three categories is listed below (Ref 1). These categories include substructure for both the fuselage and the wing.

Load Bearing Structural Weight (Ref 1)

- Skin
- Stringers
- Frames
- Bulkheads

Primary Structural Weight (Ref 1)

- Joints
- Fasteners
- Keel Beam
- Fail Safe Strap
- Flooring and Flooring Structural Supplies
- Pressure Web

- Lavatory Structure
- Galley Support
- Partitions
- Shear Ties
- Tie Rods
- Structural Firewall
- Torque Boxes
- Attachment Fittings

The total structural weight accounts for all structural members in addition to primary structural weight. Total structural weight does not include (Ref 1):

- Seats
- Lavatories
- Kitchen
- Stowage and Lighting
- Electrical Systems
- Flight and Navigation Systems
- Cargo Commodities
- Flight Deck Accommodations
- Air Conditioning Equipment
- Auxiliary Power Systems
- Emergency Systems

Reference 1 uses the weight breakdown of 8 commercial transport aircraft to compare the calculated weight from its parametric model (PDCYL). Reference 1 uses the value of the statistical correlation coefficient to verify the structural weight output of its model. Regression lines are plotted for load bearing, primary, and total structural weight. The model presented in this document calculated weight using the same aircraft data.

3.1.1 Wing

Table 3.1 shows the actual weight break downs of the wing for the eight aircraft that reference 1 uses to verify its weight calculations it also shows the calculated weight produced by the model presented in this document. Figures 3.1 through 3.4 show the linear regression lines for the data in Table 3.1. The correlation coefficients are displayed on each plot. Figure 3.1 presents a comparison of calculated results and the weight that NASA's PDCYL model produced.

Table 3.1: Wing Regression Analysis Data

Aircraft	W_{calc} (lbs)	W_{act} (lbs)	W_{GTO} (lbs)	$W_{primary}$ (lbs)	W_{total} (lbs)	W_{PDCYL} (lbs)
B-720	12,177	11,747	222,000	18,914	23,528	13,962
B-727	8,167	8,791	169,000	12,388	17,860	8,688
B-737	4,243	5,414	149,710	7,671	10,687	5,717
B-747	53,545	50,395	833,000	68,761	88,202	52,950
DC-8	18,533	19,130	310,000	27,924	35,330	22,080
MD-11	38,838	35,157	602,500	47,614	62,985	33,617
MD-83	7,796	8,720	140,000	11,553	15,839	6,953
L-1011	30,450	28,355	430,000	36,101	46,233	25,034

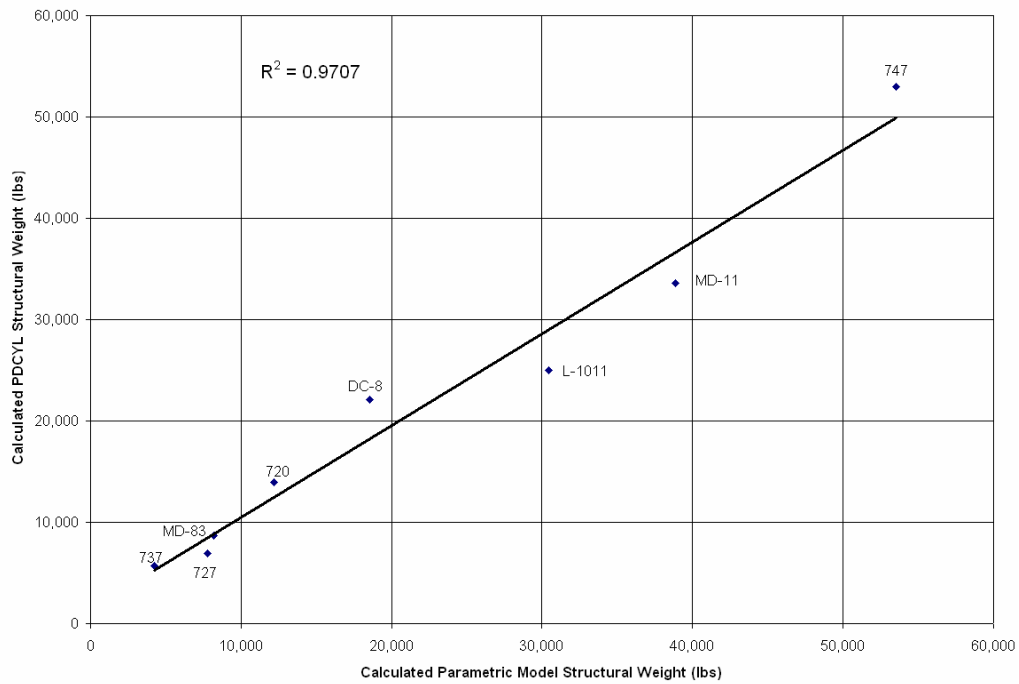


Figure 3.1: Linear Regression Correlation between PDCYL and Calculated Results

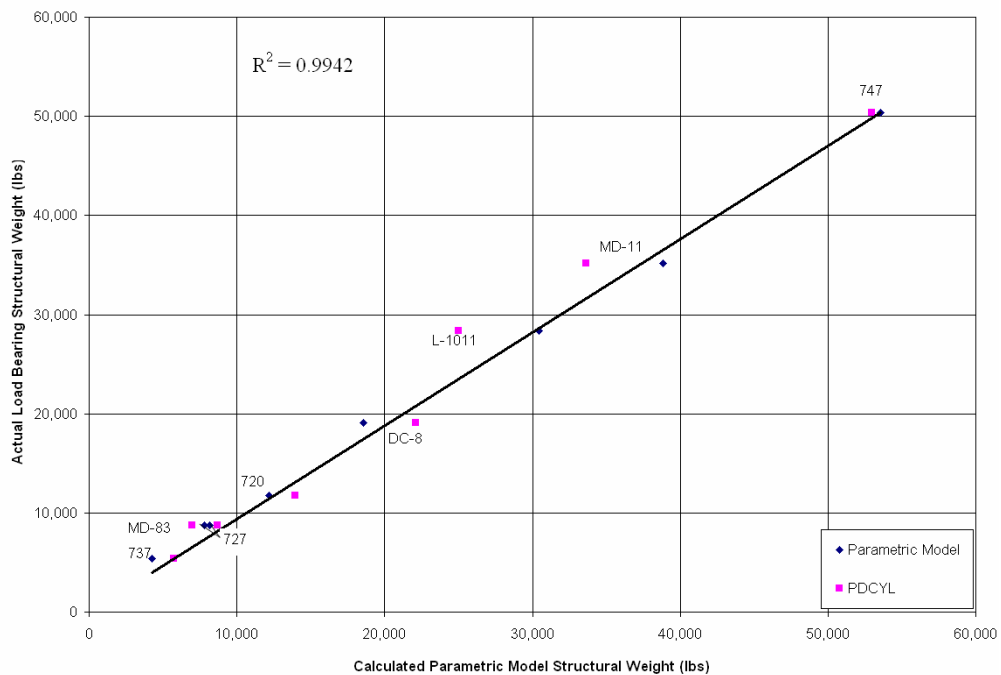


Figure 3.2: :Linear Regression Correlation between Actual Load Bearing Weight and Calculated Results

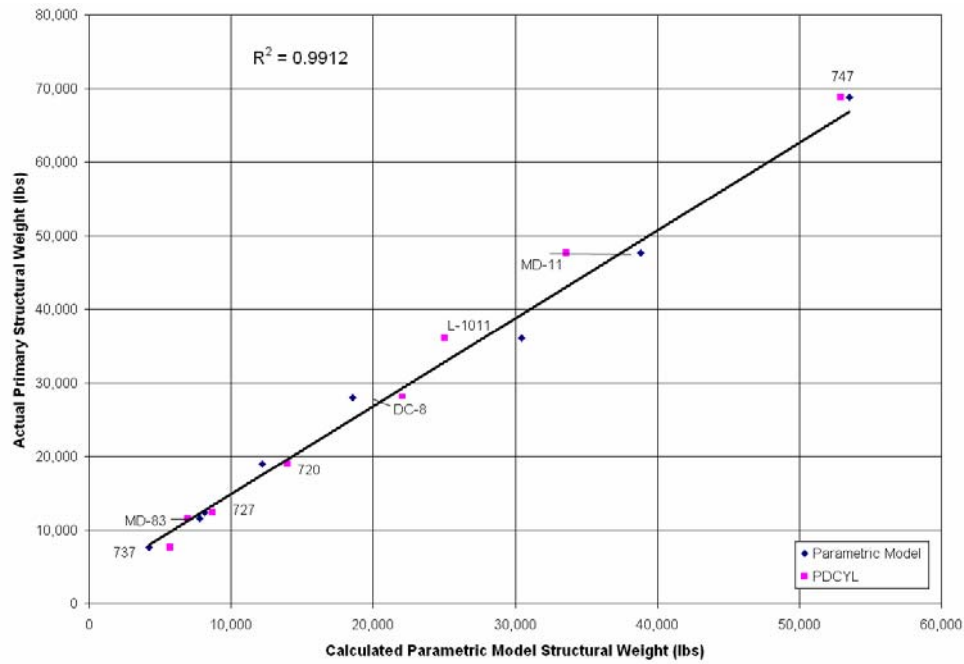


Figure 3.3: Linear Regression Correlation between Actual Primary Weight and Calculated Results

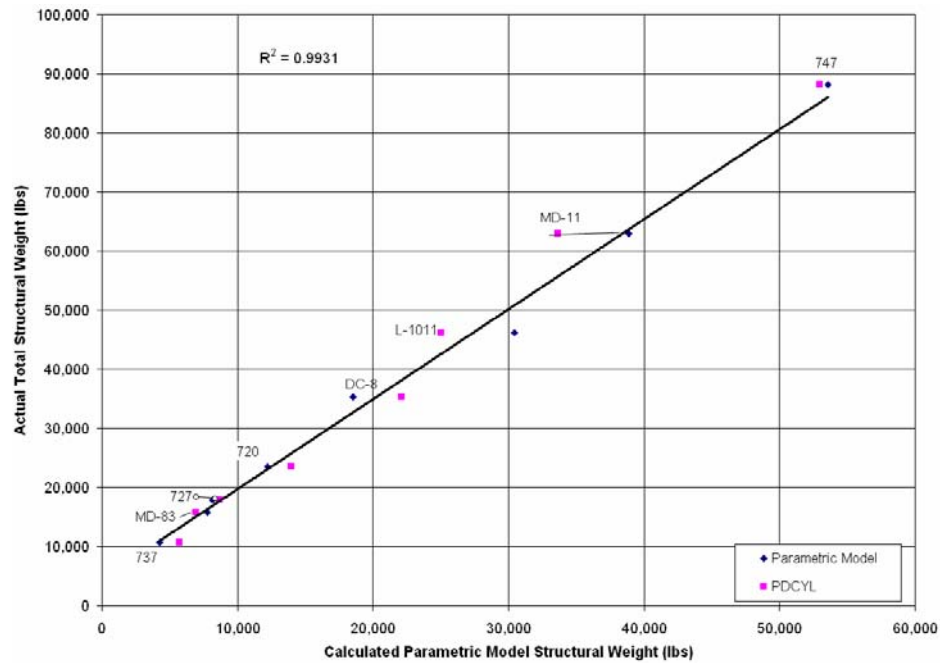


Figure 3.4: : Linear Regression Correlation between Actual Total Structural Weight and Calculated Results

3.1.2 Fuselage

Table 3.2 presents the weight breakdown for the fuselage of the eight aircraft documented in reference 1. Figure 3.5 compares the calculated data with that produce by NASA's PDCYL model. The regression lines comparing the calculated weight with the actual weight are presented in Figures 3.6 through 3.8. The correlation coefficients are displayed on the plots.

Table 3.2: Fuselage Regression Analysis Data

Aircraft	W_{calc} (lbs)	W_{act} (lbs)	W_{GTO} (lbs)	$W_{primary}$ (lbs)	W_{total} (lbs)	W_{PDCYL} (lbs)
B-720	6,544	9,013	222,000	13,336	19,383	6,545
B-727	5,530	8,790	169,000	12,424	17,586	5,888
B-737	3,693	5,089	149,710	7,435	11,831	3,428
B-747	30,615	39,936	833,000	55,207	72,659	28,039
DC-8	10,056	13,312	310,000	18,584	24,886	9,527
MD-11	21,726	25,970	602,500	34,999	54,936	20,915
MD-83	5,172	9,410	140,000	11,880	16,432	7,443
L-1011	16,401	28,355	430,000	41,804	52,329	21,608

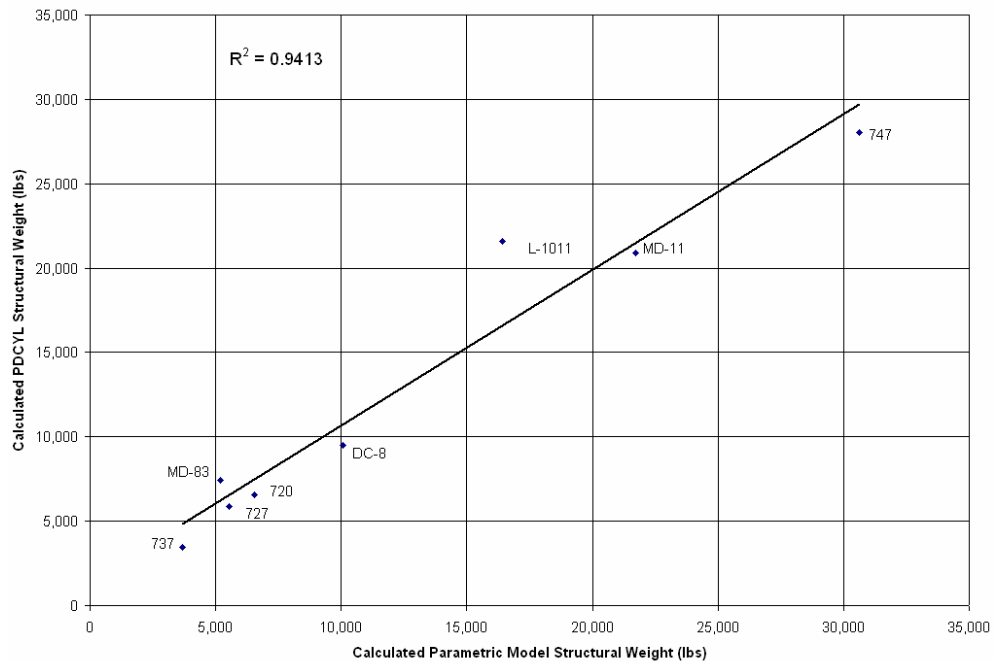


Figure 3.5: Linear Regression Correlation between PDCYL and Calculated Model Results

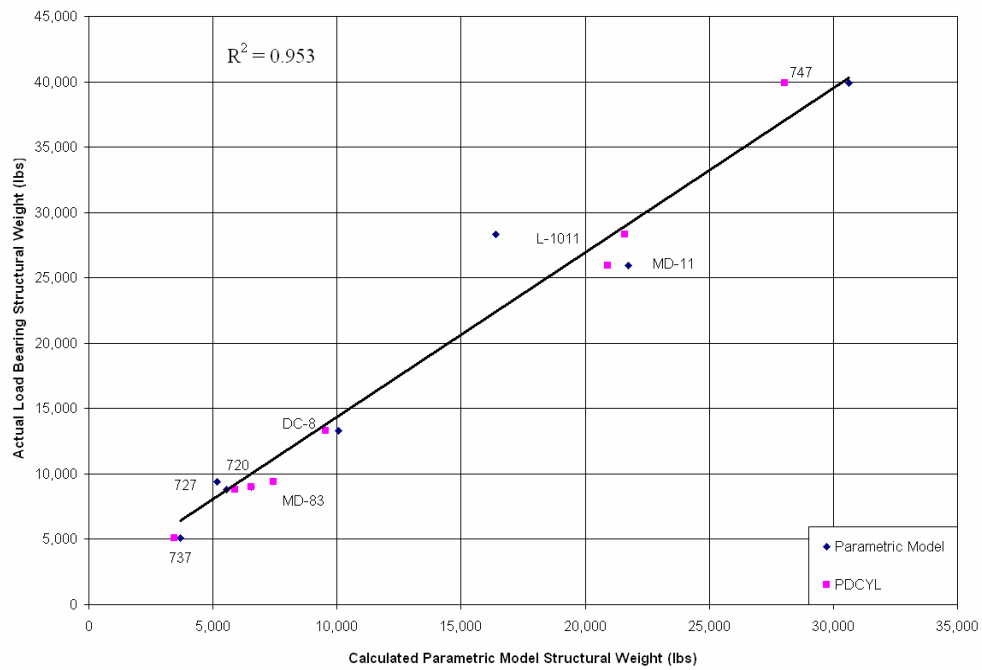


Figure 3.6: Linear Regression Correlation between Actual Load Bearing Weight and Calculated Model Results

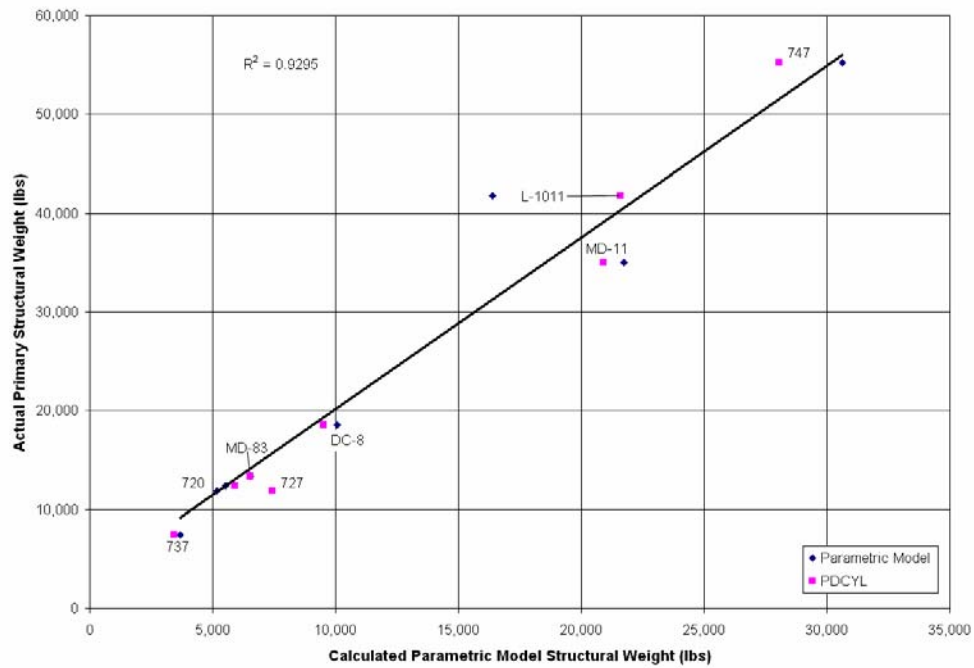


Figure 3.7: Linear Regression Correlation between Actual Primary Weight and Calculated Model Results

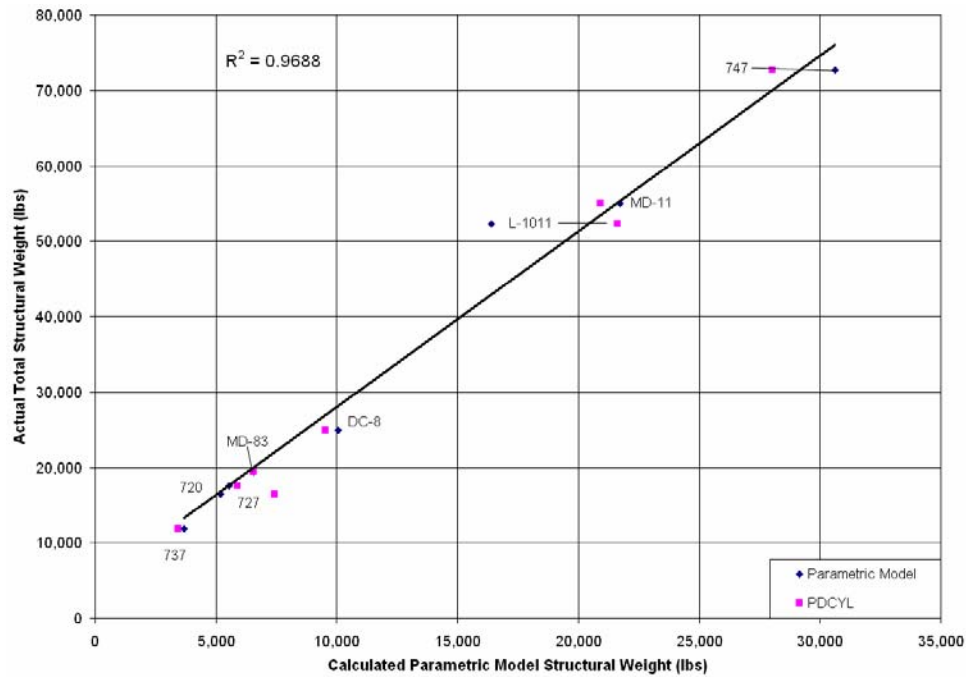


Figure 3.8: Linear Regression Correlation between Actual Total Structural Weight and Calculated Model Results

The results calculated by the model presented in this document correlate better for the wing than the fuselage. This could be because there are no tail loads applied to the sized fuselage structure and because curved geometry is not considered in the weight estimate. Including the frame and rib structure in the weight calculations would give better correlation for the both the wing and fuselage.

3.2 *Finite Element*

The following section verifies the in-plane axial stress and shear stress in the model with finite element.

3.2.1 **Wing**

The wing finite element geometry is given in Figure 3.9. The axial load on the FEM simulating the wing box at the root is given in Figure 3.10. The wing skin modeled as shell elements show stress concentrations at the root of the wing, where the skin meets the spar caps. Figure 3.11 shows the shell element ID numbers so the actual axial stress can be looked up in the output file (“f06” file). From Figure 3.10 it appears that the stress from the parametric model lies in between the orange and the yellow region illustrating the large tensile load in the bottom wing skin, blue and light blue illustrating the large compression load in the top wing skin. The stress due to bending in the top and bottom skin is approximately 43ksi.

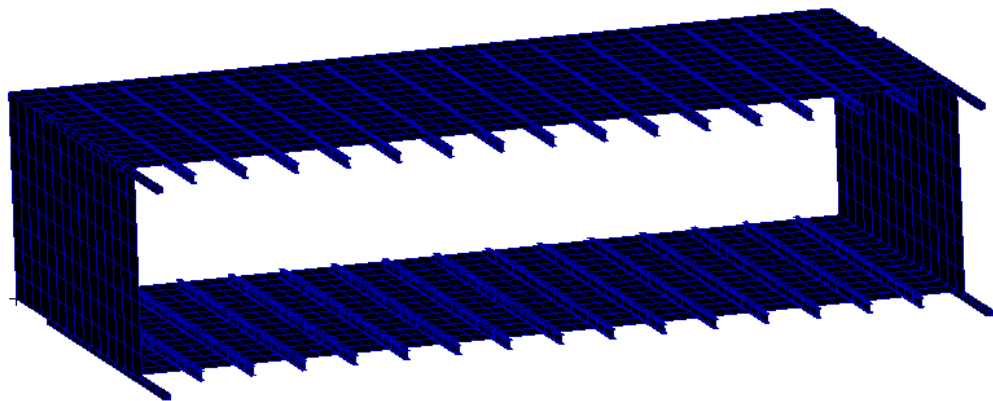


Figure 3.9: Wing Finite Element Geometry

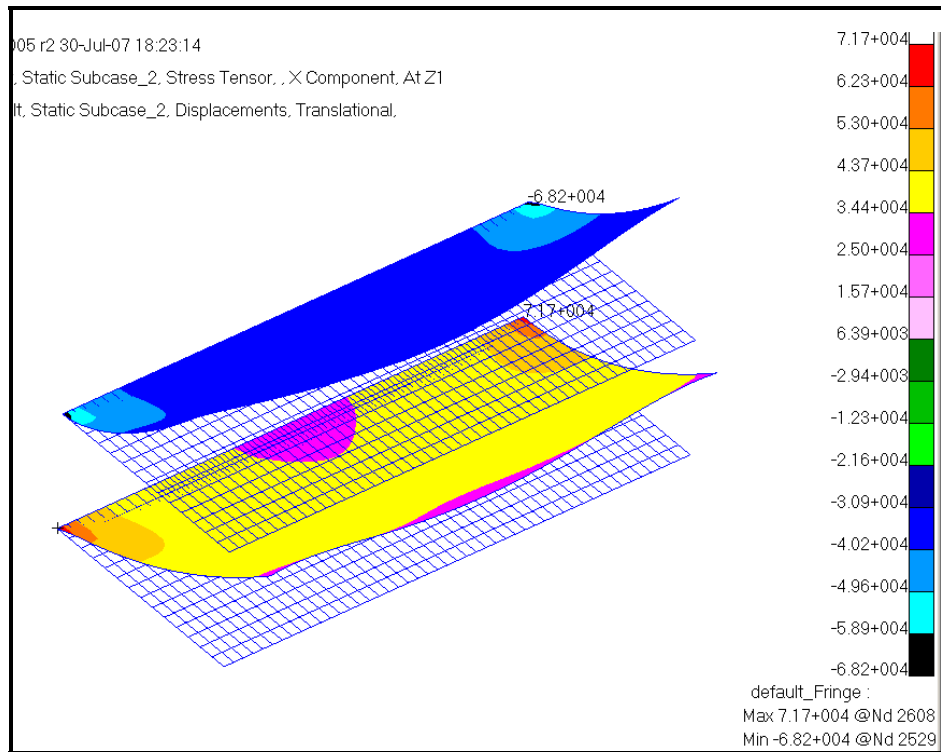


Figure 3.10: Axial Stress in Skin

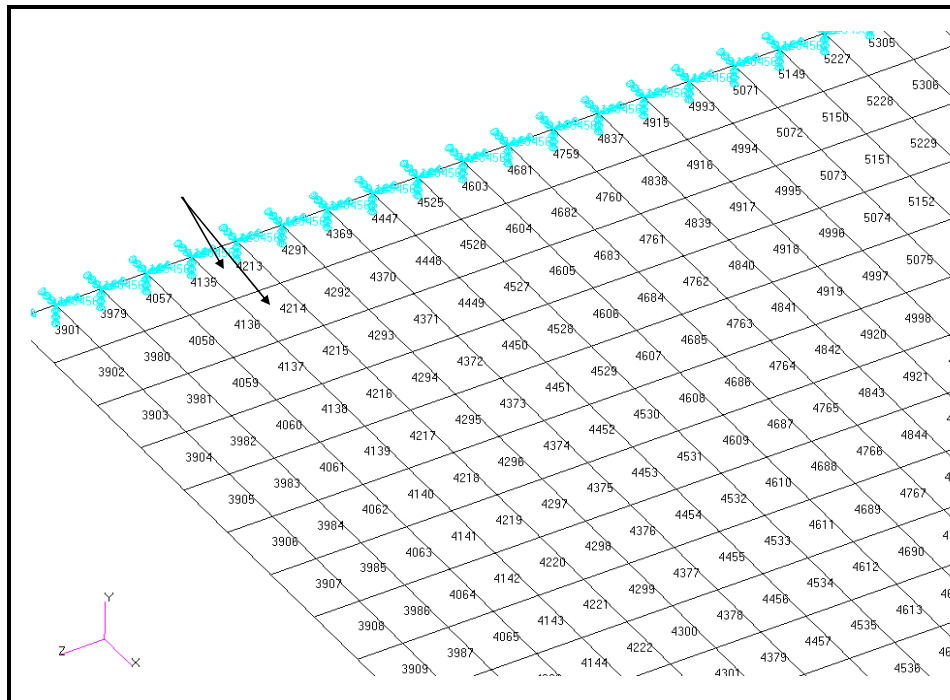


Figure 3.11: Top Skin Element ID Numbers

ELEMENT ID	GRID-ID	FIBER DISTANCE	STRESSES IN ELEMENT COORD SYSTEM		
			NORMAL-X	NORMAL-Y	SHEAR-XY
4213	CEN/4	-2.500000E-01	-4.208489E+04	-1.199796E+04	-4.551396E+03
		2.500000E-01	-4.431154E+04	-1.288838E+04	-4.325226E+03
	4504	-2.500000E-01	-4.290822E+04	-1.388802E+04	-4.551396E+03
		2.500000E-01	-4.527473E+04	-1.462281E+04	-4.325226E+03
	4505	-2.500000E-01	-4.290822E+04	-1.010791E+04	-4.551396E+03
		2.500000E-01	-4.527473E+04	-1.115395E+04	-4.325226E+03
4214	CEN/4	-2.500000E-01	-4.126157E+04	-1.010791E+04	-4.551396E+03
		2.500000E-01	-4.334836E+04	-1.115395E+04	-4.325226E+03
	4583	-2.500000E-01	-4.126157E+04	-1.388802E+04	-4.551396E+03
		2.500000E-01	-4.334836E+04	-1.462281E+04	-4.325226E+03
	4505	-2.500000E-01	-4.286246E+04	-8.560627E+03	-4.175380E+03
		2.500000E-01	-4.524419E+04	-9.793844E+03	-3.737211E+03
4214	CEN/4	-2.500000E-01	-4.389286E+04	-1.036450E+04	-4.175380E+03
		2.500000E-01	-4.635518E+04	-1.146172E+04	-3.737211E+03
	4506	-2.500000E-01	-4.389286E+04	-6.756749E+03	-4.175380E+03
		2.500000E-01	-4.635518E+04	-8.125966E+03	-3.737211E+03
	4585	-2.500000E-01	-4.183206E+04	-6.756749E+03	-4.175380E+03
		2.500000E-01	-4.413320E+04	-8.125966E+03	-3.737211E+03
4584	CEN/4	-2.500000E-01	-4.183206E+04	-1.036450E+04	-4.175380E+03
		2.500000E-01	-4.413320E+04	-1.146172E+04	-3.737211E+03

Figure 3.12: Axial and Shear Stresses in Elements 4213 and 4214 (“F06 file”)

```

sx1 =
1.0e+004 *
-4.2926 -4.2023 -4.1270 -3.0084 -1.5042 0.0000 1.5042 3.0084 4.1270 4.2023 4.2926
>> touxy1
touxy1 =
1.0e+004 *
0.4562 1.1584 1.1765 1.2006 1.2369 1.2489 1.2369 1.2006 1.1765 1.1584 0.4562

```

Figure 3.13: Axial and Shear Stress from Model

It is shown that the stresses in the “f06 file”, Figure 3.12, are approximately equal to the stresses given in the model presented in this document, Figure 3.13. These stresses are for elements on the top skin of the wing box root, the element ID number are given in Figure 3.11.

3.2.2 Fuselage

The fuselage model is a simple un-tapered cylinder. The axial stress distribution is given in Figure 3.14. The axial stress in the model presented in this document is given in Figure 3.15. The “f06 file” is not displayed because the stress in Figure 3.15 is consistent with the stress in the finite element model, Figure 3.14.

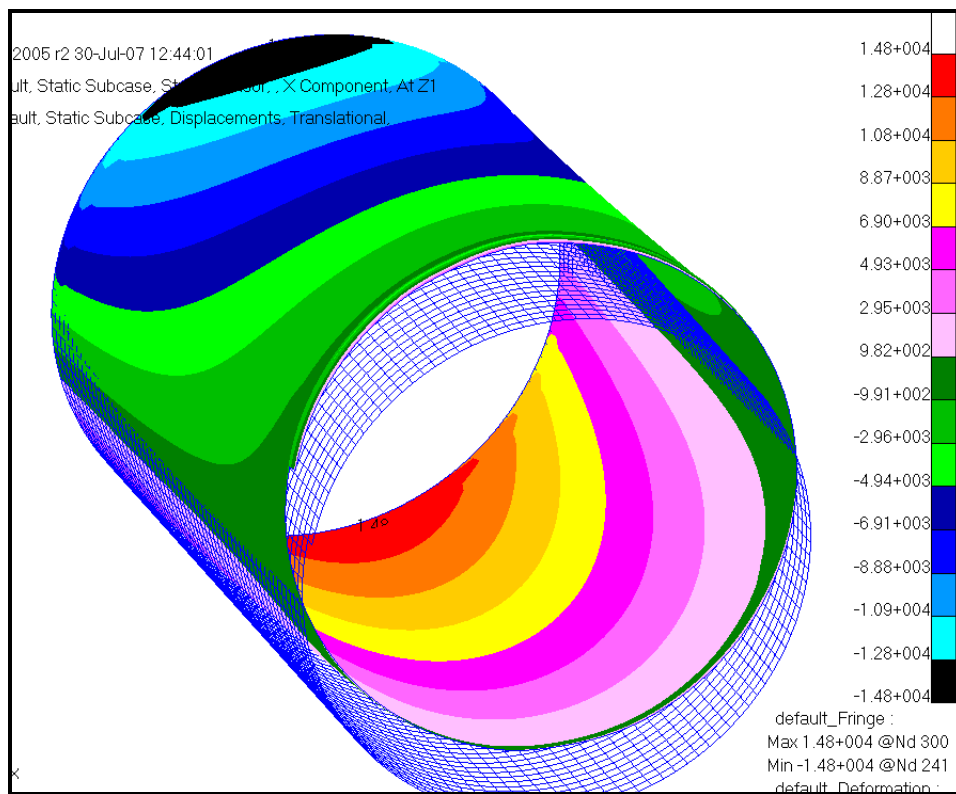


Figure 3.14: Axial Stress

sx2 =												
1.0e+004 *												
Columns 1 through 12												
1.4491	1.4471	1.4412	1.4313	1.4175	1.3998	1.3782	1.3529	1.3238	1.2912	1.2550	1.2153	
Columns 13 through 24												
1.1724	1.1262	1.0769	1.0247	0.9697	0.9120	0.8518	0.7893	0.7246	0.6579	0.5894	0.5193	
Columns 25 through 36												
0.4478	0.3751	0.3013	0.2267	0.1515	0.0758	-0.0000	-0.0758	-0.1515	-0.2267	-0.3013	-0.3751	
Columns 37 through 48												
-0.4478	-0.5193	-0.5894	-0.6579	-0.7246	-0.7893	-0.8518	-0.9120	-0.9697	-1.0247	-1.0769	-1.1262	
Columns 49 through 60												
-1.1724	-1.2153	-1.2550	-1.2912	-1.3238	-1.3529	-1.3782	-1.3998	-1.4175	-1.4313	-1.4412	-1.4471	
Column 61												
-1.4491												

Figure 3.15: Axial Stress from Model

Figure 3.16 illustrates the shear stress distribution in the finite element model. Figure 3.17 shows the shear stress distribution calculated from the model presented in this document. The shear stress distribution in the finite element model is consistent with the shear stress distribution calculated in this model.

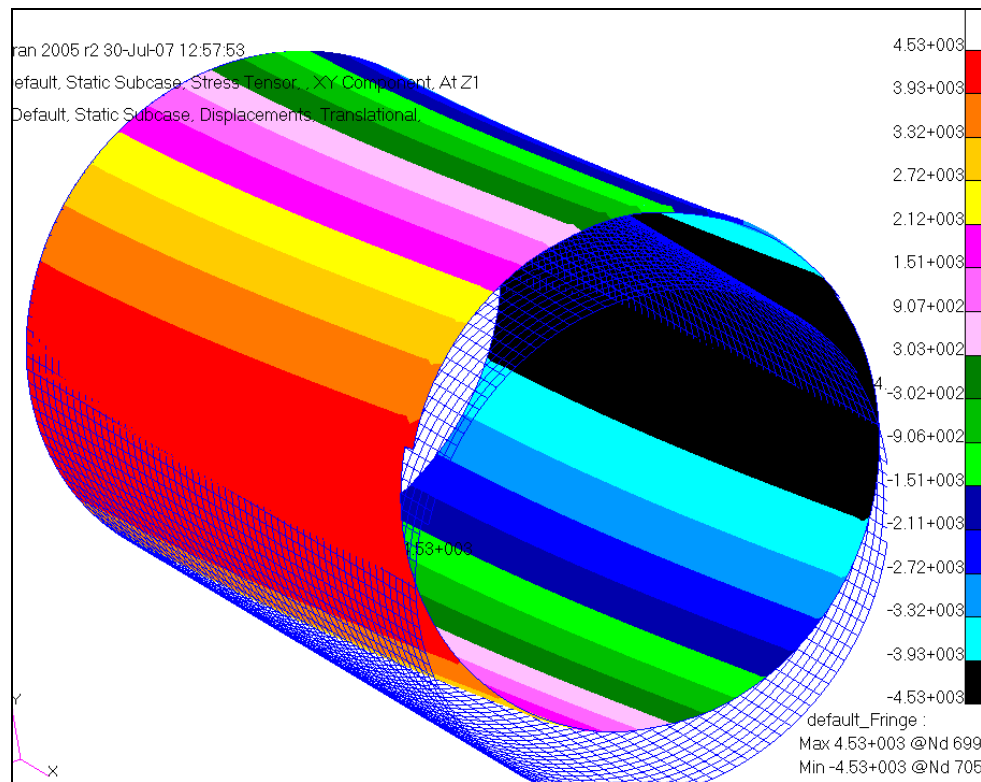


Figure 3.16: Shear Stress

touxy2 =

1.0e+003 *

Columns 1 through 12	0.2289	0.4575	0.6851	0.9112	1.1351	1.3561	1.5738	1.7875	1.9966	2.2005	2.3988	2.590
Columns 13 through 24	2.7759	2.9538	3.1239	3.2857	3.4389	3.5829	3.7175	3.8421	3.9566	4.0605	4.1536	4.235
Columns 25 through 36	4.3063	4.3656	4.4132	4.4490	4.4729	4.4849	4.4849	4.4729	4.4490	4.4132	4.3656	4.306
Columns 37 through 48	4.2356	4.1536	4.0605	3.9566	3.8421	3.7175	3.5829	3.4389	3.2857	3.1239	2.9538	2.775
Columns 49 through 60	2.5907	2.3988	2.2005	1.9966	1.7875	1.5738	1.3561	1.1351	0.9112	0.6851	0.4575	0.228
Column 61	0.0000											

Figure 3.17: Shear Stress Calculated in Model

4 Results and Discussion

The baseline and enhanced material case results are presented for CFRP and Aluminum Alloy in Table 4.1 and 4.2 respectively. The weight estimate includes the mass of the longitudinal load bearing structure, which for the wing and fuselage structure is the skin and stringers. The percent weight benefit of the enhanced material cases are also presented in Tables 4.1 and 4.2 (next to the calculated weight values). The CFRP resulting structural load bearing weight calculations neglect whether the optimized thickness is realistic to manufacture along with being a symmetric and balanced laminate. The percent weight benefit is calculated in reference to the baseline material.

Table 4.1: CFRP Baseline and Enhanced Material Weights (% Structural Weight Reduction)

	Baseline Material	Improved Composite 1 Baseline+25%OHC	Improved Composite 2 Baseline+25%OHT	Improved Composite 3 Baseline+50% Elastic Modulus
Wing Structural Weight (lb)				
Wide Body	16,737	14,829 (11.4%)	15,811 (5.5%)	16,635 (0.6%)
Narrow Body	3,177	2,860 (10.0%)	3,011 (5.2%)	3,167 (0.3%)
Fuselage Structural Weight				
Wide Body	10,968	10,554 (3.8%)	10,959 (0.1%)	10,199 (7.0%)
Narrow Body w/ Min Gauge =55mil	2,337	2,337 (0.0%)	2,337 (0.0%)	2,189 (6.3%)
Narrow Body Min Gauge=30mil	1,923	1,923 (0.0%)	1,923 (0.0%)	1,713 (10.9%)
Total Structural Weight (lb)				
Wide Body	27,705	25,383 (8.4%)	26,770 (3.4%)	26,834 (3.1%)
Narrow Body w/ Min Gauge =55mil	5,514	5,197 (5.7%)	5,348 (3.0%)	5,356 (2.9%)
Narrow Body Min Gauge = 30mil	5,100	4,783 (6.2%)	4,934 (3.3%)	4,880 (4.3%)

The fatigue or strength depends on the material notch toughness, nominal load, structure geometry, notch geometry, detectable crack size, and loading cycle profile for the aircraft. The fatigue performance for the Aluminum Alloys currently used in industry is unknown. Rather enhanced fatigue performance cases are studied to determine a range of weight benefit from the application of Aluminum Alloy with high fatigue performance.

Table 4.2: Aluminum Baseline and Enhanced Material Weights (% Structural Weight Reduction)

	Baseline Material	Advanced Alloy 1 +10% Elastic Modulus	Advanced Alloy 2 +50% Fatigue Performance (36 ksi)	Advanced Alloy 3 +100% Fatigue Performance (48 ksi)
Wing Structural Weight (lb)				
Wide Body	33,046	32,941 (0.3%)	25,998 (21.3%)	22,595 (31.6%)
Narrow Body	6,187	6,160 (0.4%)	4,915 (20.6%)	4,305 (30.4%)
Fuselage Structural Weight				
Wide Body	16,575	16,560 (0.1%)	12,585 (24.1%)	11,319 (31.7%)
Narrow Body	3,749	3,749 (0.0%)	2,688 (28.3%)	2,277 (39.3%)
Total Fuselage Structural Weight				
Wide Body	49,621	49,501 (0.2%)	38,583 (22.2%)	33,914 (31.7%)
Narrow Body	9,936	9,909 (0.3%)	7,603 (23.5%)	6,582 (33.8%)

To judge the consistency of the method used to determine the stiffener spacing and geometry, the baseline material structural weights are compared to their structural un-stiffened configuration weight. It is determined that all the structure is stiffness critical if un-stiffened. The ratio of the stiffened to un-stiffened weight for the wing and fuselage of the wide and narrow body aircraft is given in Table 4.3. It is desired that the numbers between the CFRP and Aluminum Alloy for the wing and fuselage of each aircraft are similar. This helps insure that a weight performance benefit for the application CFRP over Aluminum is not biased because the CFRP is more efficient than the Aluminum Alloy stiffened configuration.

Table 4.3: Stiffened and Un-stiffened Structural Weights

		Baseline Material Stiffened Configuration Weight (lb)	Baseline Material Un-Stiffened Configuration Weight (lb)	Stiffened/Un-Stiffened Weight (lb/lb)
Wide Body				
Wing	CFRP	16,601	52,011	0.32
	Aluminum	33,046	100,509	0.33
Fuselage	CFRP	10,538	26,610	0.40
	Aluminum	16,575	44,210	0.37
Narrow Body				
Wing	CFRP	3,147	12,515	0.25
	Aluminum	6,187	24,178	0.26
Fuselage	CFRP (MG = 55mil)	2,229	7,580	0.29
	Aluminum	3,749	12,868	0.29

How does the weight performance benefits from the application of CFRP and Aluminum Alloy on a medium transport aircraft compare with that on a small transport aircraft?

The results indicate that the small transport aircraft will have an almost equal structural weight benefit that the medium aircraft has using CFRP compared with Aluminum Alloy. Figure 4.1 plots the weight benefit of CFRP compared to Aluminum Alloy for the narrow and wide body aircraft for a range of fatigue performance. If the Aluminum wide and narrow body aircraft have different fatigue performance behavior they will see different benefits from the application of CFRP as their primary load bearing structural material. When the minimum laminate thickness is found for each structural region, allowing a 5% variation in the target laminate family (i.e. for the fuselage [25/50/25]), a reduction is seen in the weight benefit of

CFRP when compared to Aluminum Alloy. The decrease is more dramatic in the case of the narrow body. Using the ply thickness of the current material used on the medium jet transports, the narrow body will see a weight penalty when compared to an Aluminum Alloy with fatigue strength above 33ksi. Therefore, based on this analysis, with the current laminate thicknesses the narrow body will not have the weight benefit from the application of CFRP that the wide body does. When neglecting minimum laminate thickness, the narrow body will have a similar weight performance benefit as the wide body. The total structural weight values of CFRP aircraft is in Table 4.1. and for Aluminum Alloy in Table 4.2.

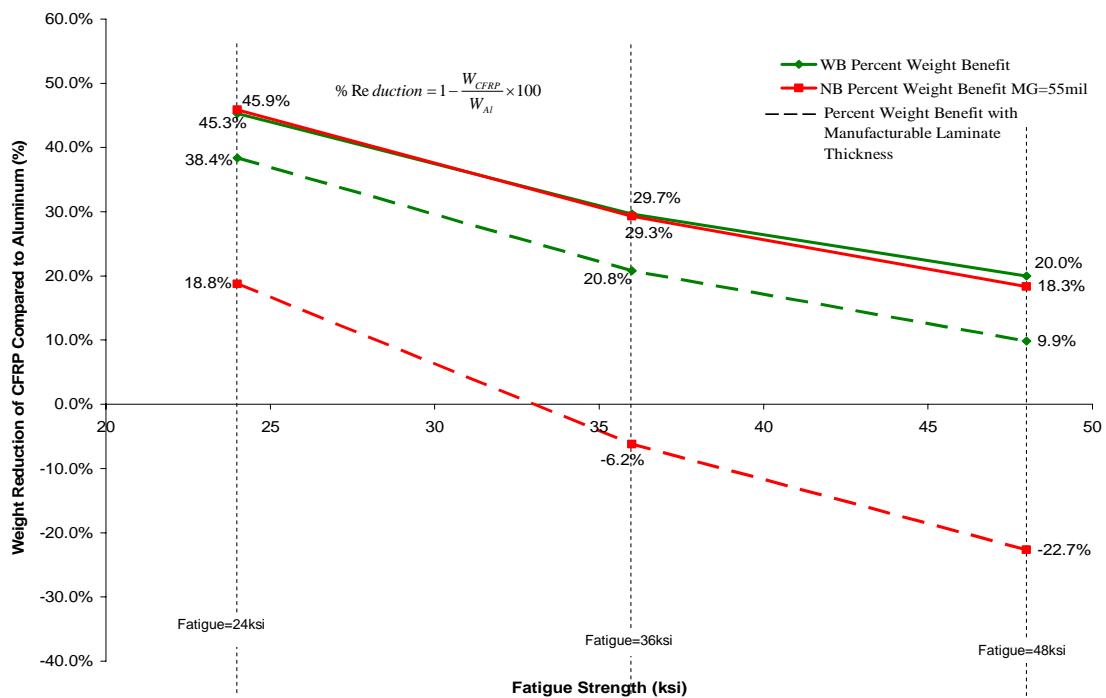


Figure 4.1: Percent Load Bearing Structural Weight Benefit of CFRP over Aluminum for a Range of Potential Fatigue Performance

What are the critical structural design drivers with the application of CFRP on the medium and small commercial transport and how do they compare?

The data from Table 4.1 shows that the wide and narrow body CFRP wing experiences the largest reduction in weight from OHC enhancement (Improved Composite Case 1). Therefore OHC is the most weight sensitive design driver for the CFRP wing box structure on both the wide and narrow body aircraft. OHC is a critical design driver because it is the lowest material strength allowable governing the design. The wide body CFRP wing has more of a weight benefit because it has thicker skin and a larger load. Enhancing a lower stress allowable yields a larger thickness benefit than increasing high stress allowable this is illustrated in Figure 4.2. This is also the reason why increasing OHC yields more of a weight performance benefit than enhancing OHT. Figure 4.3 shows the failure mode distribution on the wing structure, which is the same for the wide and narrow body and all subsequent material enhancements except Improved Composite 1 applied to the narrow body. Relationship of thickness change with the change of low and high stress allowables is given in Figure 4.2. Figure 4.3 shows an increase in the stiffness critical region on the upper wing skin of the narrow body aircraft with a 25% OHC enhancement.

(50)

$$t \propto \frac{1}{\sigma_{Design}}$$
$$M.S. = \frac{\sigma_{All}}{\sigma_{Design}} - 1 = 0 \rightarrow \sigma_{Design} = \sigma_{All}$$

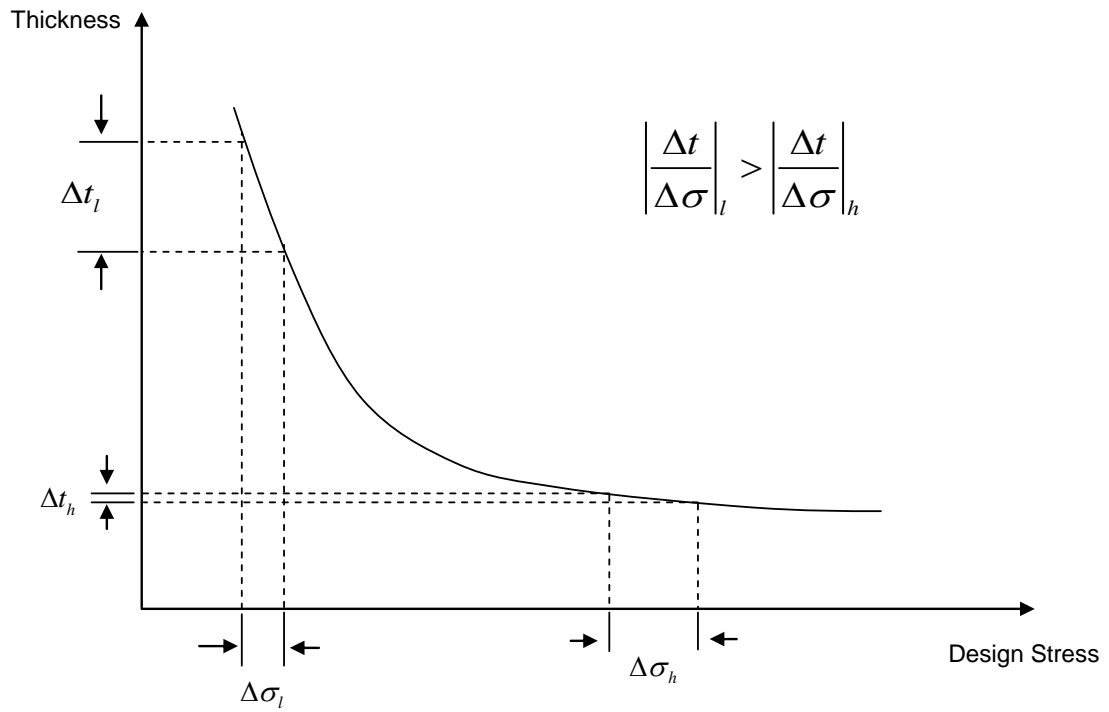


Figure 4.2: Skin Thickness Design Stress Relationship

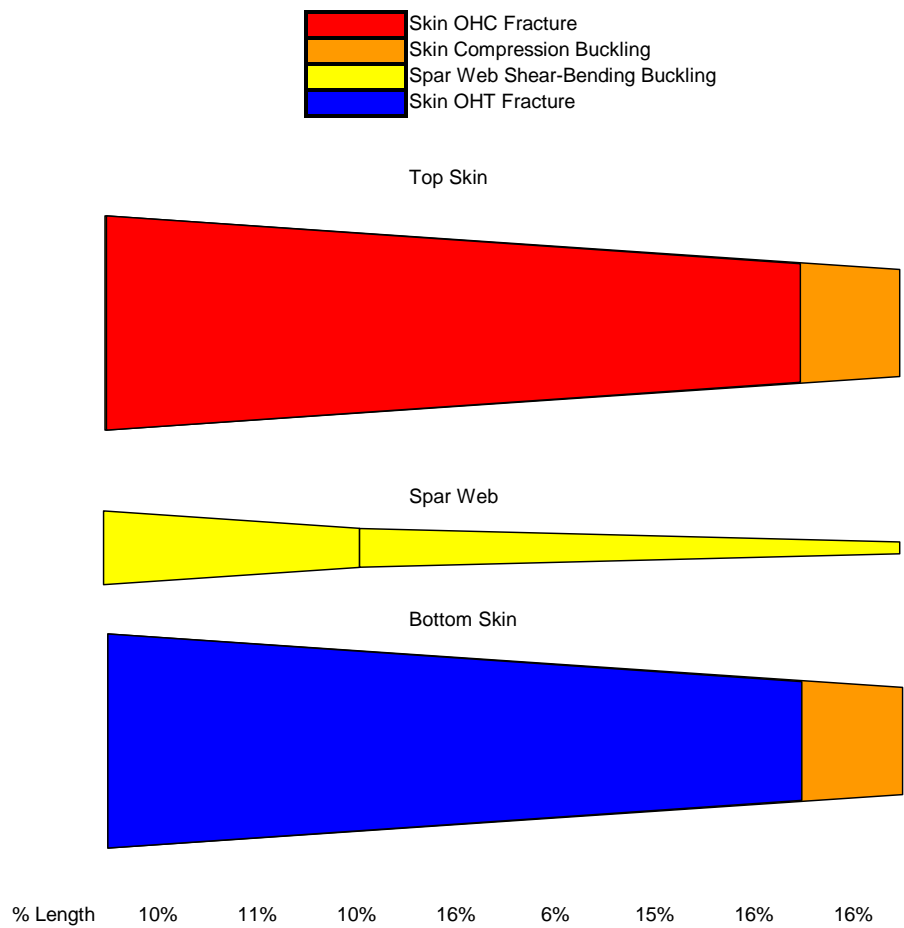


Figure 4.3: Failure Mode Distribution on Wing Structure for Wide and Narrow body (CFRP Baseline and all cases except for narrow body Improved Composite 1)

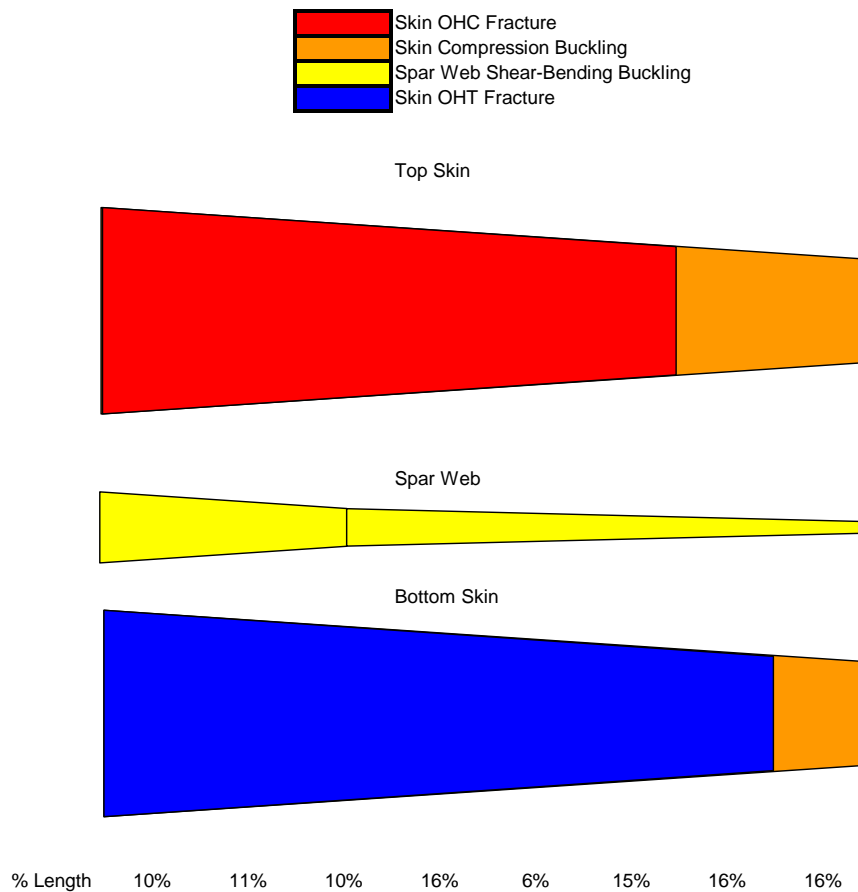


Figure 4.4: Failure Mode Distribution for Narrow Body Wing (CFRP Improved Composite 1)

The most weight sensitive material enhancement for the wide and narrow body CFRP fuselage is the 50% increase in the Elastic Modulus. Table 4.1 shows that in the case of the relaxed minimum gauge the narrow body experiences more of a weight benefit than the wide body from the stiffness enhancement. The wide body has less of a benefit from stiffness enhancement because a portion of its fuselage is OHC fracture critical. If the narrow body fuselage structure is limited by minimum gauge than the wide body has more of a weight benefit from stiffness enhancement. Both

aircrafts fuselage structure has OHT fracture critical sections. They have a small amount of weight benefit from OHT enhancement because, as stated earlier, enhancements for allowables at large stress levels, relative to the structure, have a smaller decrease in thickness or no decrease in thickness if limited by minimum gauge. Figure 4.5 shows the failure mode distribution for the wide body fuselage. Figure 4.6 shows the failure mode distribution for the narrow body fuselage, which has the same failure mode distribution for all subsequent material enhancements.

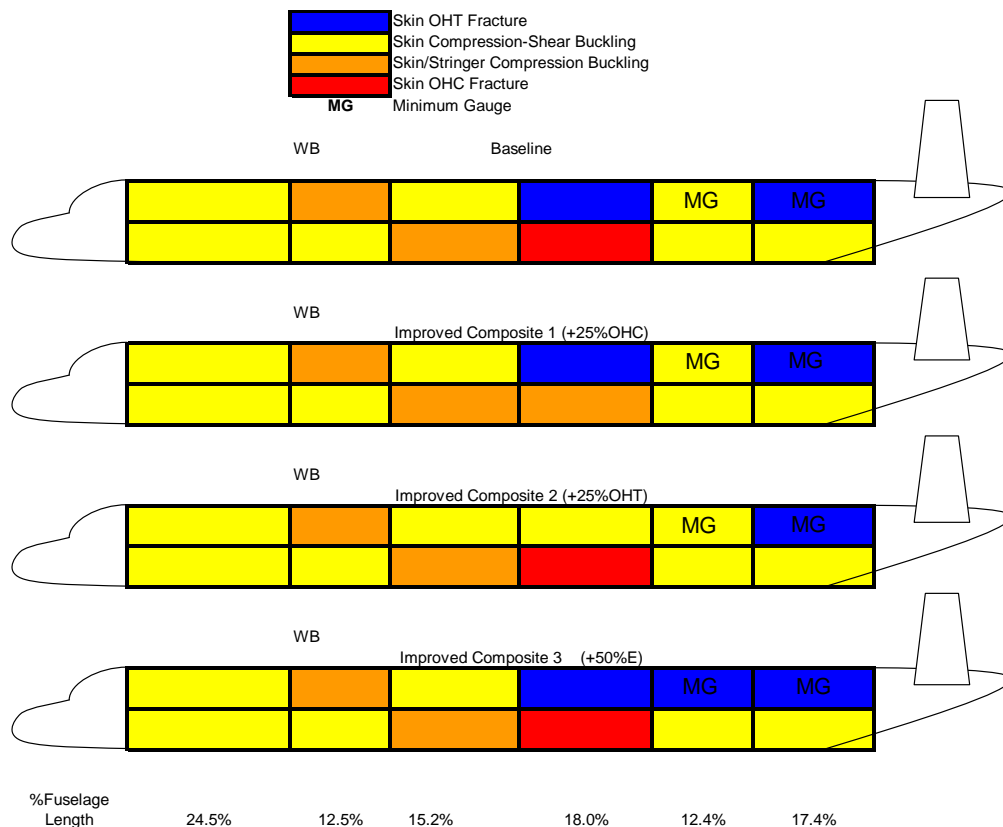


Figure 4.5: Failure Mode Distribution on Wide Body Fuselage (CFRP)

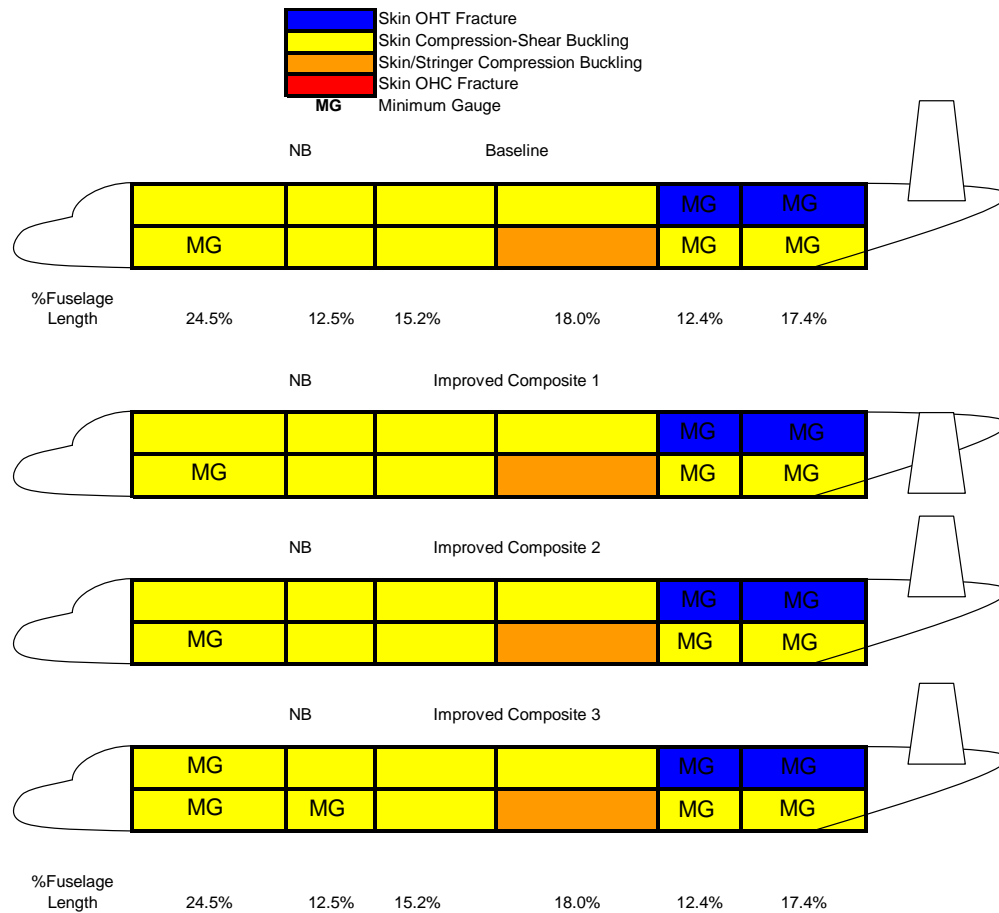


Figure 4.6: Failure Mode Distribution on Narrow Body Fuselage (CFRP)

The most weight sensitive material enhancement is OHC for both the wide and narrow body aircraft total load bearing structural weight. The second most weight sensitive material enhancement is OHT for the wide and narrow body aircraft

Though OHT is neither the CFRP wing or fuselage structures most weight sensitive material enhancement it provides more of a weight reduction in the wing

than Improved Composite 3 provides in the fuselage structure. If the narrow body minimum gauge is relaxed to 30 mils the Improved Composite 3 stiffness enhancement is the second most weight sensitive material case for the total load bearing structural weight. There are portions of the fuselage structure that are OHT critical where the critical stress is hoop stress. The skin on the OHT critical (pressurization critical) portions of the fuselage are so thin that you see little weight benefit from Improved Composite 2, in the narrow body case there is no weight benefit because the skin thickness is limited by minimum gauge.

The wide and narrow body wing has a similar critical failure mode pattern. Both aircrafts have OHT critical lower skins of the wing and a large percentage of the top skin OHC critical. The OHC enhancement provided more of a weight benefit than OHT, even though it's critical in a smaller portion of the wing, because it's a much lower stress allowable therefore thickness reduction is more sensitive to OHC enhancement.

The primary failure mode in the wide and narrow body fuselage is compression-shear buckling. Only one fuselage section of the wide body is OHC critical, the narrow body has none. There is a large weight benefit in the wide body fuselage when the OHC is enhanced because it has the largest reduction in skin thickness.

What are the critical failure modes on the Aluminum Alloy wide and narrow body aircraft structure?

The wide and narrow body airframe is most sensitive to fatigue performance. The Aluminum Alloy wing and fuselage have a large buckling critical portion of their structure but a 10% stiffness enhancement shows very little weight benefit in the thickness range. The wide and narrow body wing show similar weight benefits when enhancing the Fatigue strength. The failure mode distribution is similar for the Aluminum Alloy wide and narrow body aircraft along with all subsequent material enhancements. The failure distribution for the Aluminum Alloy wing structure on the wide and narrow body aircraft is given in Figure 4.7.

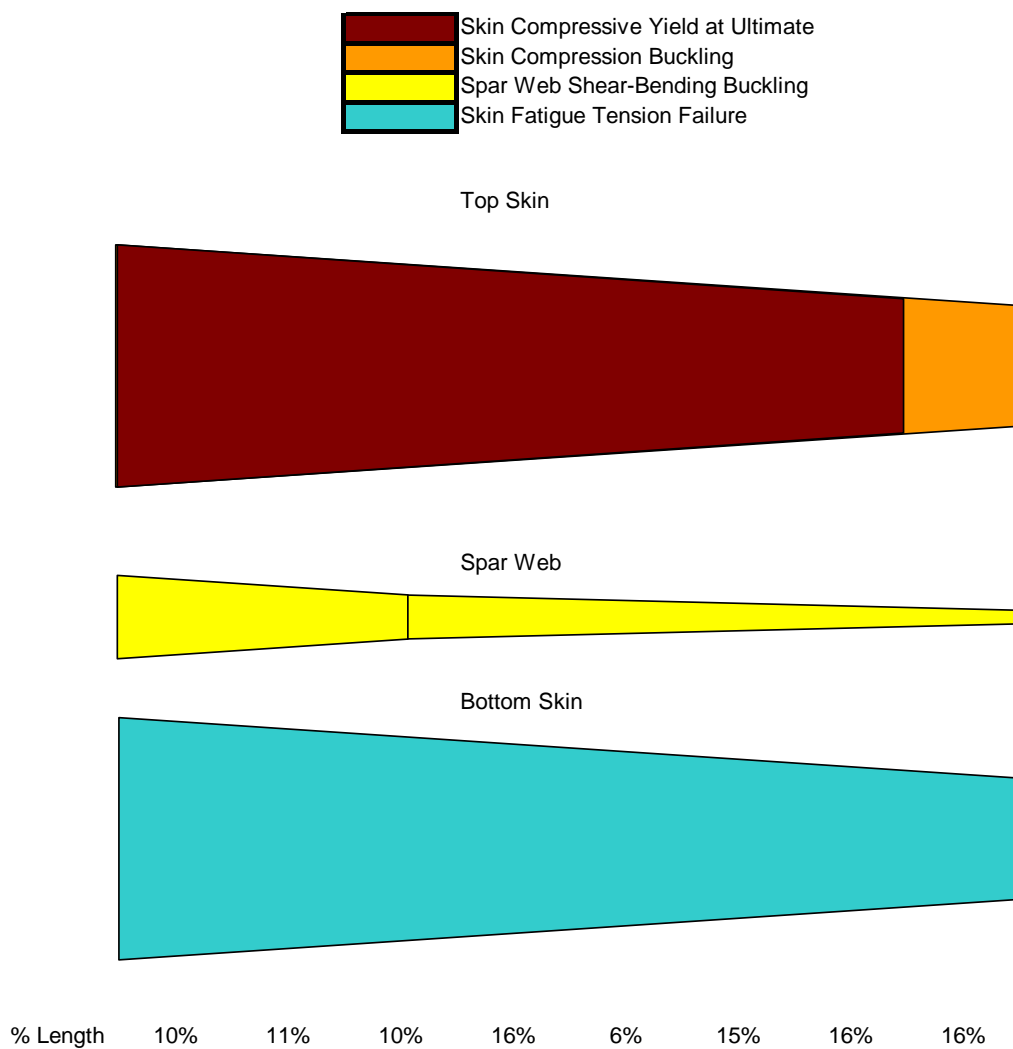


Figure 4.7: Failure Mode Distribution for Wide Body and Narrow Body Wing (Aluminum)

The Aluminum Alloy narrow body fuselage has the most weight benefit because it is entirely fatigue critical due to pressurization. Table 4.2 shows weight benefits of the Aluminum material enhancements which include 10% Elastic Modulus, 50% Fatigue performance, and 100% Fatigue performance enhancement. The material fatigue enhancement cases give a range of possible fatigue performance for an Aluminum Alloy aircraft similar to the size of the narrow body and wide body aircraft. Figure 4.8 shows the failure mode distribution for the Aluminum Alloy wide body fuselage and all subsequent material enhancements. Figure 4.9 shows the failure mode distribution on the Aluminum Alloy narrow body fuselage and all subsequent material enhancements.

The Aluminum Alloy wide body aircraft with a fatigue performance of 24 ksi is almost entirely fatigue critical from fuselage pressurization and bending tension stress, except for a fracture critical section above aft of the wing box. The wide body Advanced Alloy 2 optimized failure mode output and state of stress with the respective critical load case is shown in Figure 4.8. Advanced Alloy 3 which increases the fatigue performance to 48ksi has a failure mode scheme where the entire forward fuselage is compression and shear buckling critical and the mid-section (above the wing box) is tension fracture critical from load case 2. The failure modes are similar for the narrow body aircraft except there is a larger area of the skin that is fatigue fracture critical from pressurization for each material enhancement case. Therefore the critical failure modes on the wide and narrow body aircraft include:

- 1) Fatigue fracture of skin from tension stress due to pressurization and bending from load case 1 (2.5g maneuver).
- 2) Ultimate tension strength fracture of skin and stringers from bending induced by load case 2 (-2.0g hard landing).

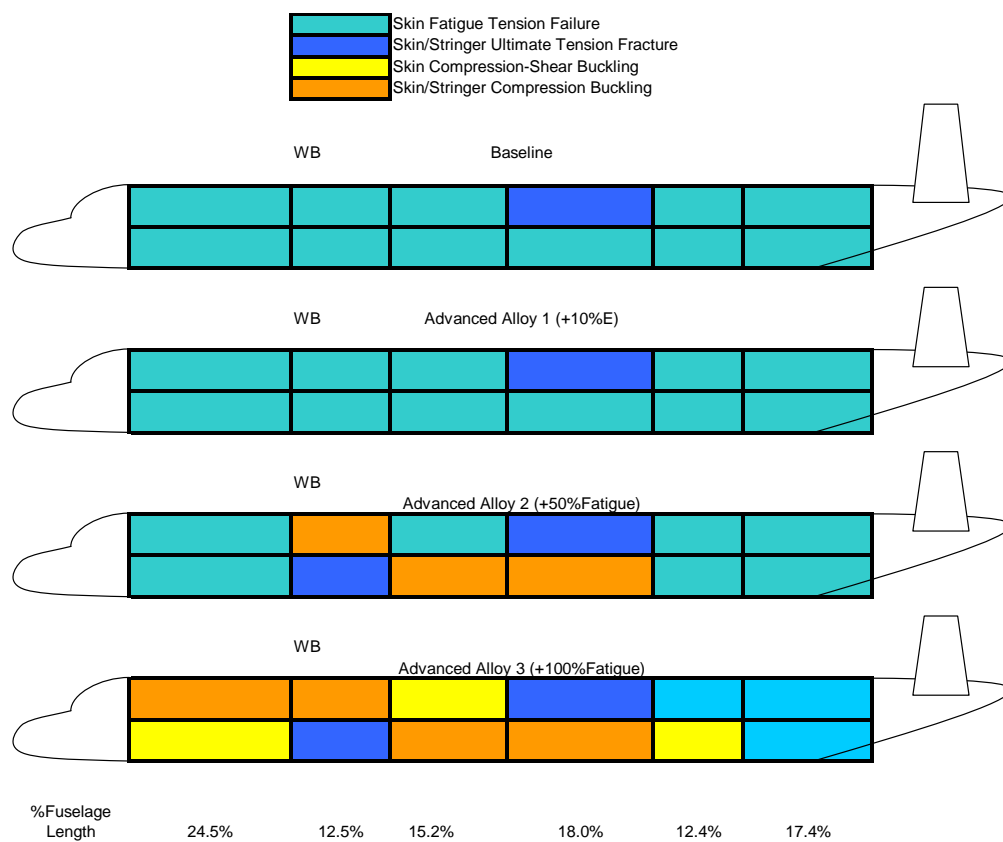


Figure 4.8: Failure Mode Distribution for Wide Body Fuselage (Aluminum)

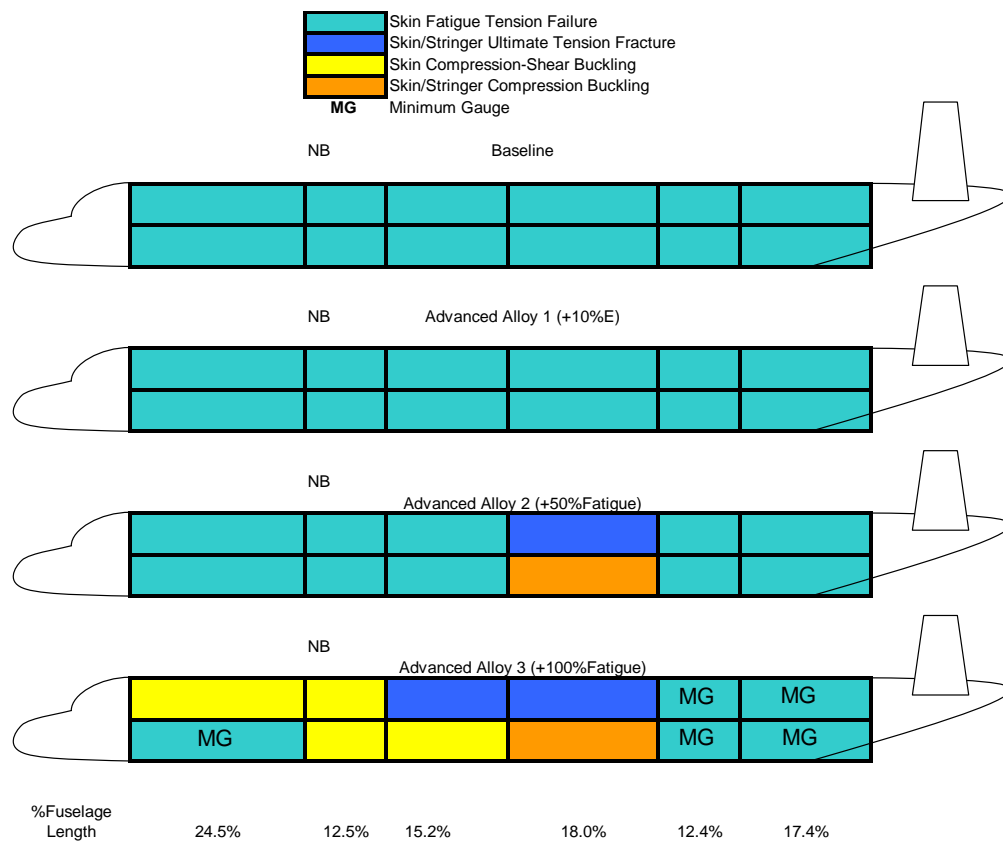


Figure 4.9: : Failure Mode Distribution for Narrow Body Fuselage (Aluminum)

5 Conclusions

The wide and narrow body aircraft yield similar failure mode distributions for CFRP Laminate. The wing structure has the most weight benefit from the enhancement of the OHC allowable and the fuselage structure has the most weight benefit from the enhancement of stiffness.

In the case of an Aluminum Alloy structure, the wide and narrow body results show similar failure mode distributions for the wing and fuselage. The Aluminum Alloy Structure is primarily fatigue failure critical and has the largest weight reduction with the enhancement of fatigue performance.

Since the wide and narrow body results show similar failure mode distributions it is not the “type” of failure that limits the feasibility of CFRP laminate being applied to the narrow body aircraft structure but rather the range of thickness of the laminate. With Improved Composite 3 (25% Elastic Modulus enhancement) more than half of the narrow body fuselage structure was limited by Minimum gauge. Therefore the weight benefit from the application of CFRP laminate on the narrow body fuselage structure is limited by minimum gauge of the laminate.

6 Recommendations

To improve the accuracy of the optimization model the following could be done:

- 1) Improving the accuracy of the critical fatigue stress (for aluminums) by conducting a more detailed fatigue methodology.
- 2) Study multiple materials for the different sections of the aircraft. This could include different types of aluminums, CFRP laminates, laminas, or fabric for different wing and fuselage sections.
- 3) Studying different structural concepts such as Honeycomb Sandwich and Iso-grid configurations.
- 4) Obtain and apply information on criteria for different failure modes such as strength after impact for CFRP, pillowing of fuselage skin due to pressurization, and delaminating due to joint flexure for CFRP.
- 5) Applying methodology for sizing ribs and frames to include in the load bearing structural weight calculation.
- 6) Applying load cases that subject the structure to torsion.

- 7) Use linear regression to scale the takeoff weight of the aircraft to the calculate load bearing structural weight in order to approximate the change in load on the structure.
- 8) Include tail loads to size the fuselage structure.
- 9) Calculate actual producible laminate thicknesses that correspond to ply thickness and laminate family.

To simplify the model and reduce computational load the following could be done:

- 1) Produce a basic axial, transverse, and shear running load profile for the wing and fuselage for a class of aircraft (w/ similar geometry). So that it could be mapped for different size aircraft. The running loads should be specific to different sub-structure.
- 2) Specify reasonable convergence criteria to reduce the number of iterations necessary to obtain an optimum thickness.

References

- (1) Ardema M.D., Chambers M.C., Patron A.P., Hahn A.S., Miura H., Moore M.D., 1996. Analytical Fuselage and Wing Weight Estimation of Transport Aircraft, NASA Technical Memorandum 110392
- (2) Curtis, Howard D. Fundamentals of Aircraft Structural Analysis 1997. Richard D. Irwin, a Times Mirror Higher Education Group, Inc.
- (3) Raymer, D.P. Aircraft Design: A Conceptual Approach 3rd Ed, 1999. American Institute of Aeronautics and Astronautics, Inc.
- (4) MIL-HDBK-17-3D, Polymer Matrix Composites Volume 3. Material Usage, Design, and Analysis 1997, U.S. Department of Defense.
- (5) Hibbler, Mechanics of Materials Fifth Edition 2003, Pearson Education, Inc.
- (6) Lan, E.L. Roskam, J. Airplane Aerodynamics and Performance Third Printing, 2003. Design, Analysis and Research Corporation (DARcorporation)
- (7) Bruhn, E.F. Analysis and Design of Flight Vehicle Structures, 1973. Jacobs Publishing, Inc.

(8) Kollar, L.P. Mechanics of Composite Structures, 2003. Cambridge University Press.

A Appendix

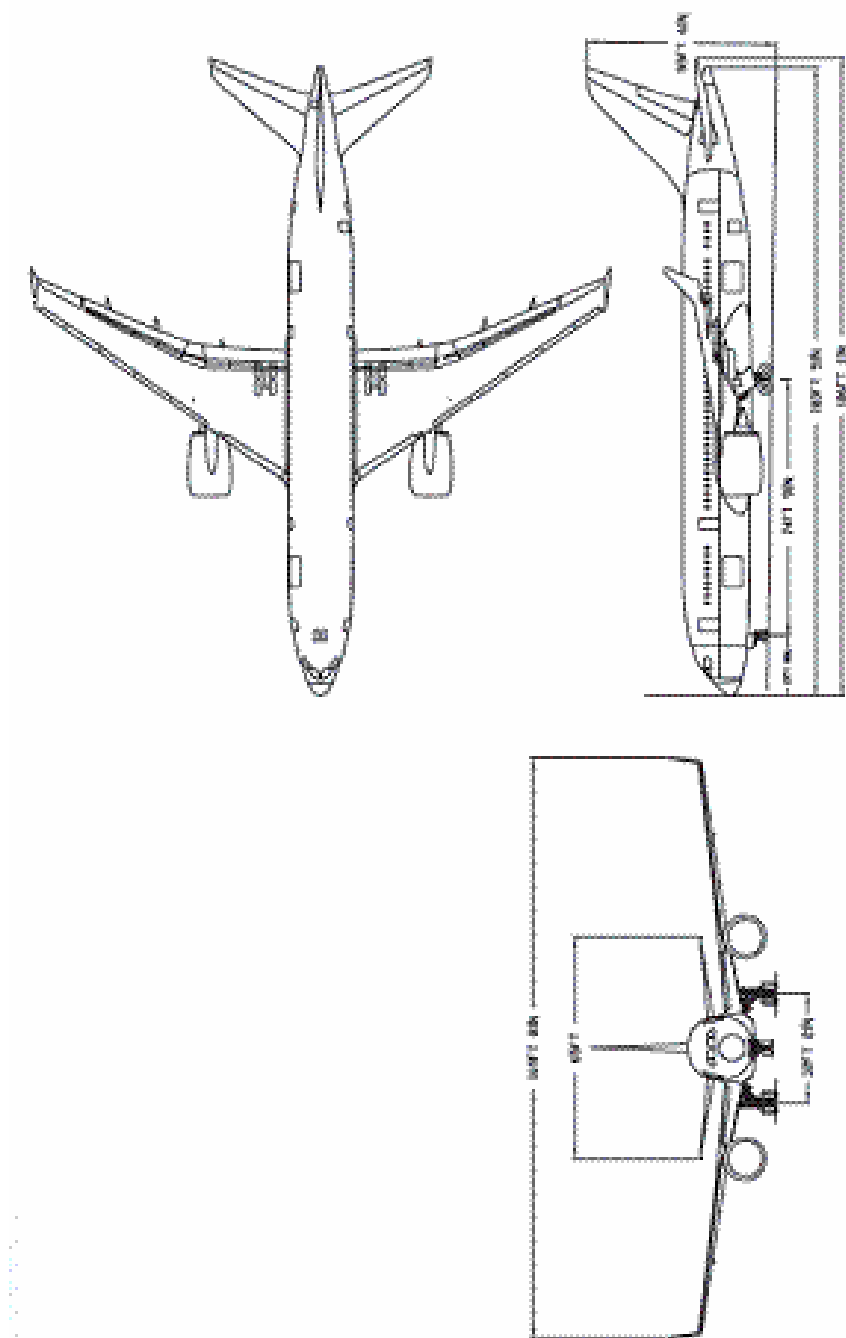


Figure A.1: Medium Body Jet Transport

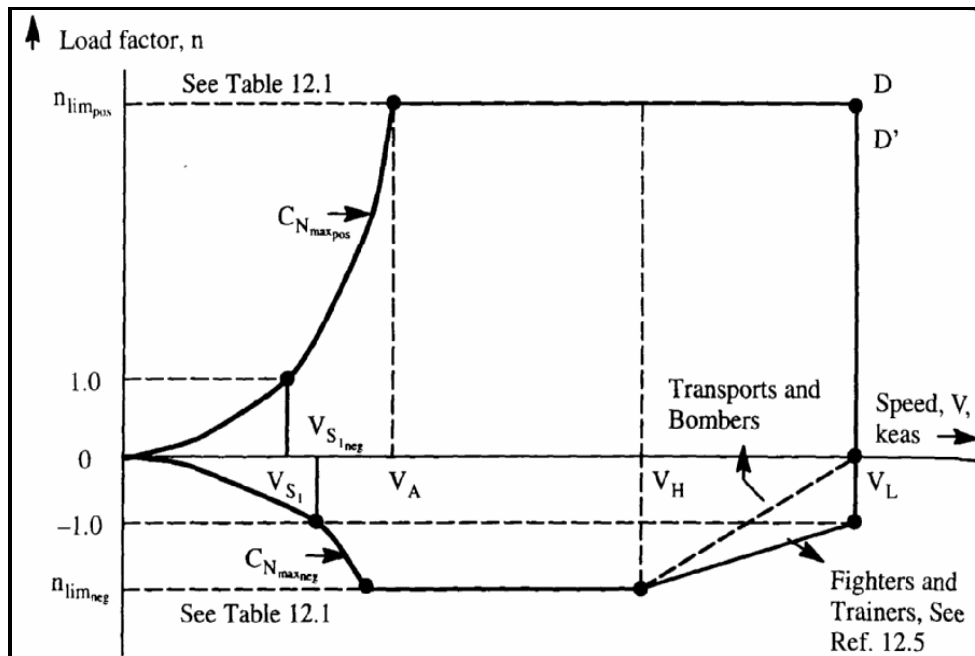


Figure 12.15 V-n Maneuver Diagram for Military Airplanes

Table 12.1 Design Limit Load Factors for Military Airplanes {MIL-A 8861 (ASG)}

Airplane Type		Design Limit Load Factor at Flight Design Gross Weight: W_{FDGW}	
USAF	USN	$n_{lim_{pos}}$	$n_{lim_{neg}}$
Fighter		8.67	-3.00
Attack	Fighter, Attack, Trainer	7.33	-3.00
	Observation	6.00	-3.00
Trainer		5.67	-2.33
Utility	Utility	4.00	-2.00
Small Bomber		3.67	-1.67
Medium Bomber, Assault Transport	Patrol, Weather, Anti-submarine, Reconnaissance	3.00	-1.00
Medium Transport		2.50	-1.00
Heavy Bomber, Heavy Transport		2.00	-1.00

Figure A.2: V-N Diagram Specifications for Military Airplanes (Ref 6)

B Appendix

Example Calculation to Determine Stringer Dimensions and Spacing

Using the running load from load case 1, wing station 66.

$$N_- = 9.5 \frac{kips}{in}$$
$$\sigma_{ohc} = 43ksi(ultimate) \rightarrow \sigma_{Limit} = 29ksi(compression)$$
$$t_{skin} = \frac{N_-}{\sigma_{ohc}} = 0.331in$$

Figure 7.12 (Ewing Buckling Presentation), simply supported boundary conditions are used. Contribution of effective width is neglected because of the heavy thickness of the skin (Bruhn).

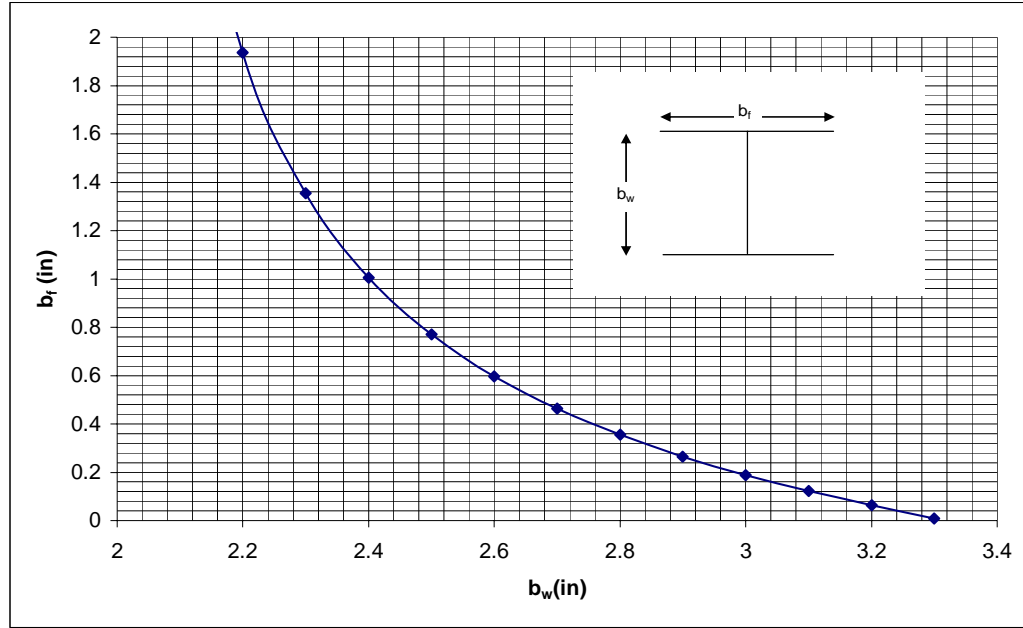
$$\sigma_{cr} = KE \left(\frac{t_{skin}}{b} \right)^2$$
$$\frac{a}{b} = 2(ss) \rightarrow K = 3.6$$
$$b = t_{skin} \sqrt{\frac{\sigma_{cr}}{KE}} = (0.331in) \sqrt{\frac{(3.6)(14.5msi)}{(29ksi)}} = 14in$$
$$\frac{a}{b} = 2 \rightarrow a = 28in.$$
$$L_e = \frac{a}{\sqrt{c}} = \frac{28}{\sqrt{1.5}} = 23in.$$

Note: The calculation of the stringer spacing b above is only used to estimate the effective length of the stiffener column. A slenderness ratio is chosen from the Euler-

Johnson Column Curve (Figure 4) for a crippling stress of $\sigma_{cc} = 30ksi$.

$$\frac{L_e}{\rho} = 24 \rightarrow \rho = 0.958$$

The following is a derivation to calculate all the solutions for the dimensions of an “I”-beam section type stiffener for a radius of gyration, ρ .



The following dimensions were chosen for the “I”-beam section type stiffener.

$$b_f = 1.0in$$

$$b_w = 2.4in.$$

Since the crippling stress is known an estimate for the thickness comes from Figure 3.

$$\frac{b_f}{b_w} \approx 0.4 \rightarrow \frac{b_w}{t_{stiffener}} = 49 \rightarrow t_{stiffener} = 0.049in$$

$$A_{stiffener} = (2b_f + b_w)t_{stiffener} = [2(1.0in) + 2.4in](0.049in) = 0.216in^2$$

The following is a method of estimating the contribution of each stiffener to the second moment of area. The width of the top skin at W.S. 66 is:

$$width = (4.077 \text{ ft}) \left(12 \frac{\text{in}}{\text{ft}} \right) = 49 \text{ in}$$

n: number of stringers

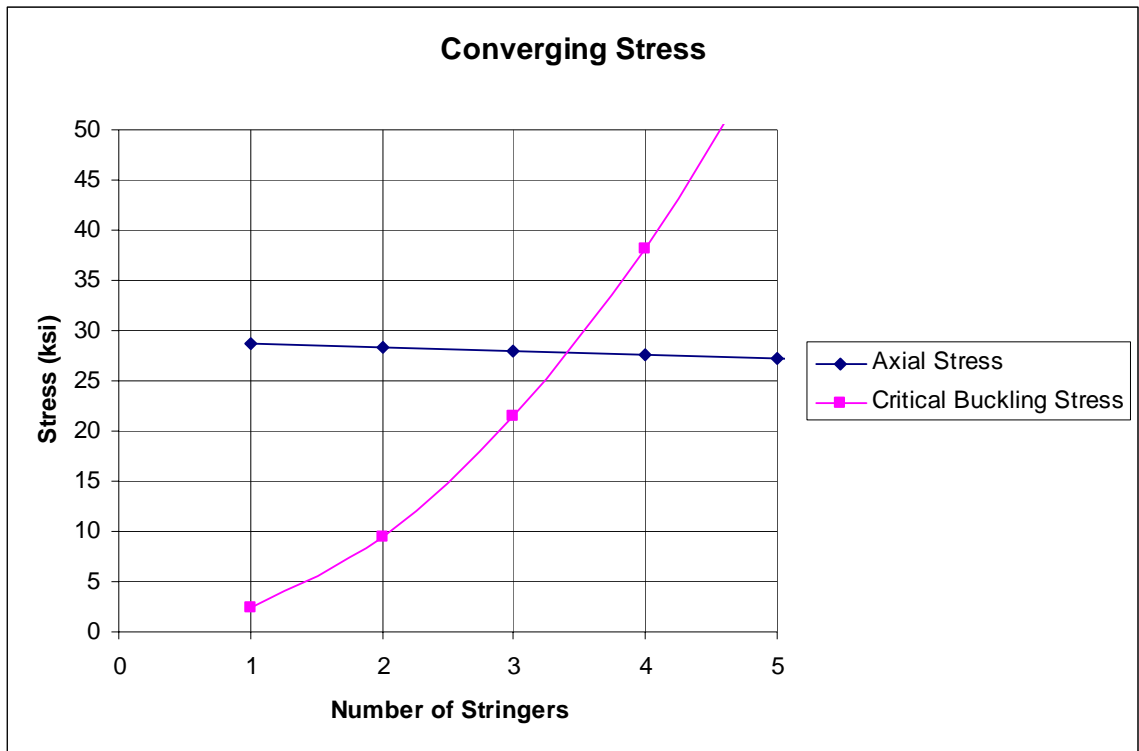
Contribution of area for n stiffeners on the top skin per unit thickness is:

$$\frac{\Delta A}{width} = \frac{(0.216 \text{ in}^2)n}{49 \text{ in}} = (4.4 \times 10^{-3} \text{ in})n$$

From the past analysis it is known that this wing station is open hole compression (top skin) fracture critical. To estimate the number of stringers it is necessary to find the stress at which the following equations converge.

$$\sigma_x = \sigma_0 \frac{t_{skin}}{t_{skin} + \frac{\Delta A}{width}} = (29 \text{ ksi}) \frac{0.331 \text{ in}}{0.331 \text{ in} + (4.4 \times 10^{-3} \text{ in})n}$$

$$\sigma_{cr} = KE \left(\frac{t}{width/n} \right)^2 = 3.6(14.5 \text{ msi}) \left(\frac{0.331 \text{ in.}}{49 \text{ in./}n} \right)^2$$



The equations above converge between 3 and 4 stringers at a stress of about 28ksi. An approximate stringer spacing is between the two calculated values below.

$$b_1 = \frac{\text{width}}{n_1} = \frac{49\text{in.}}{3} \approx 16\text{in.}$$

$$b_2 = \frac{\text{width}}{n_2} = \frac{49\text{in.}}{4} \approx 12\text{in.}$$

$$b_2 \leq b \leq b_1$$

$$12\text{in.} \leq b \leq 16\text{in.}$$

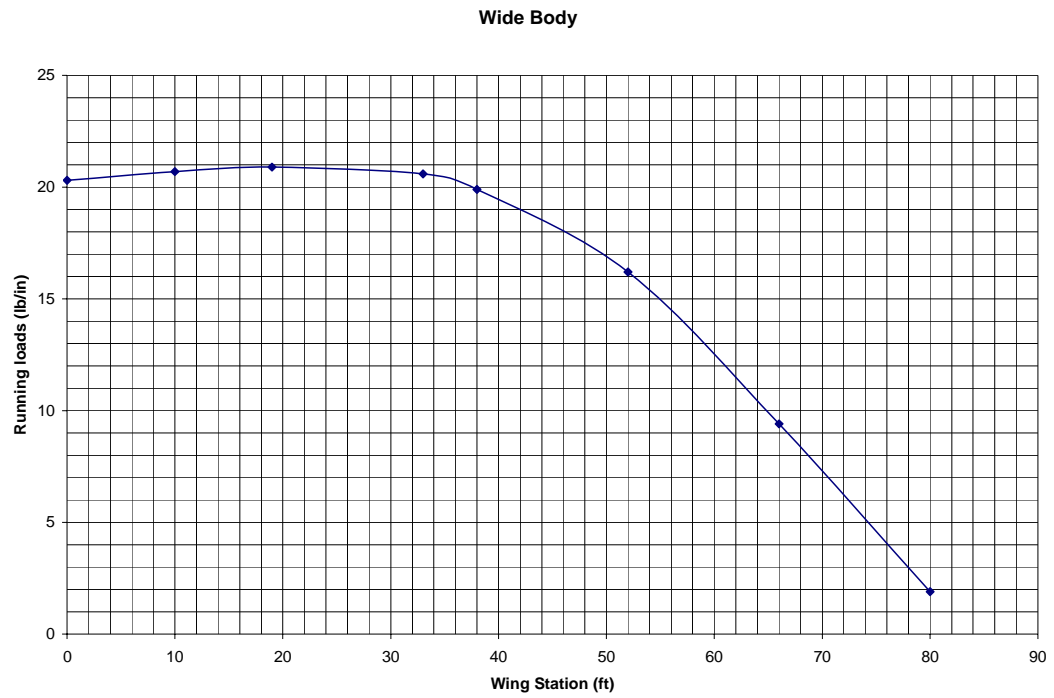


Figure B.1:WB Wing Running Loads



Figure B.2: NB Wing Running Loads

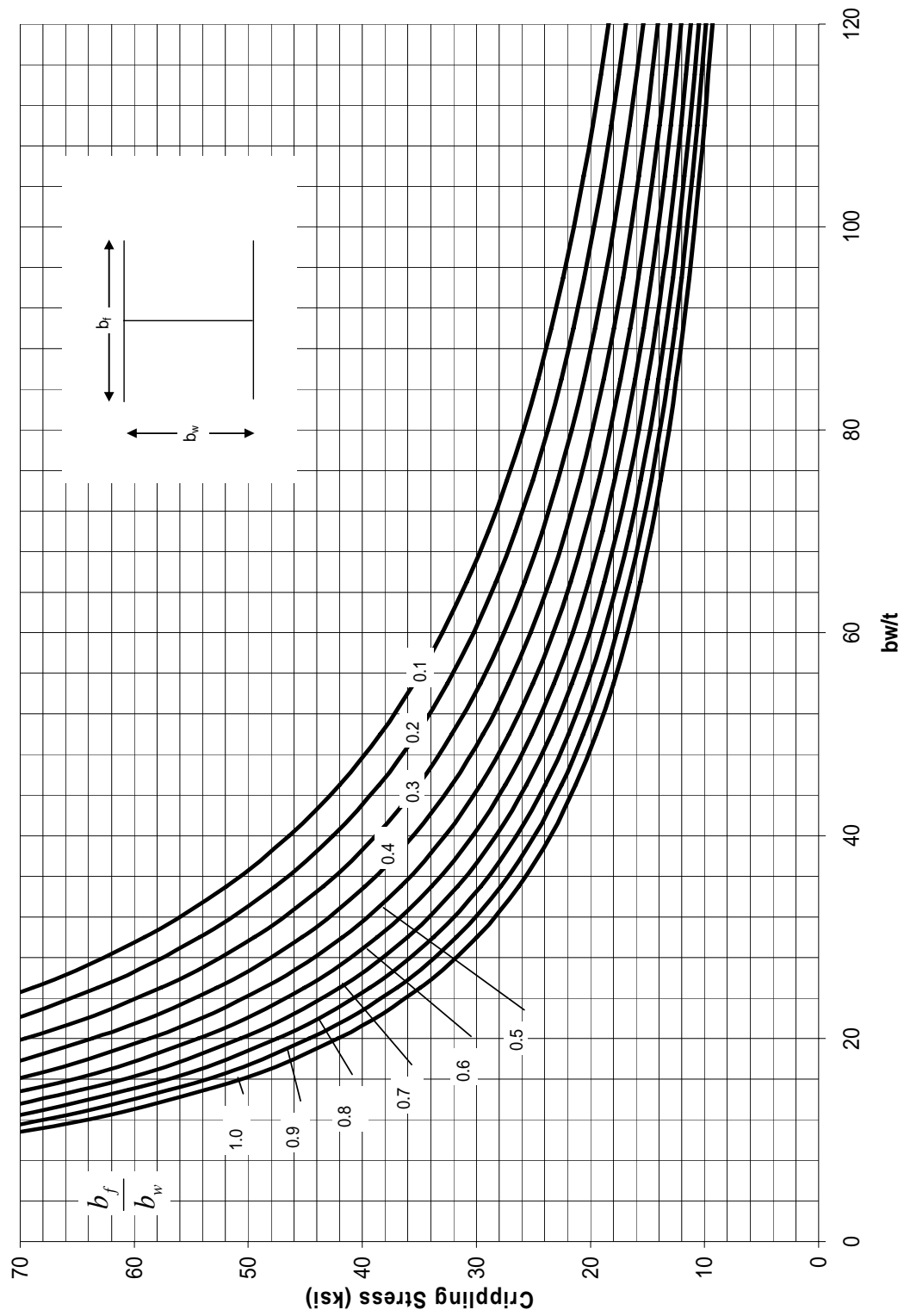


Figure B.3: Crippling of CFRP Laminate "I"-Section Beam With $E_x=14.5\text{Msi}$

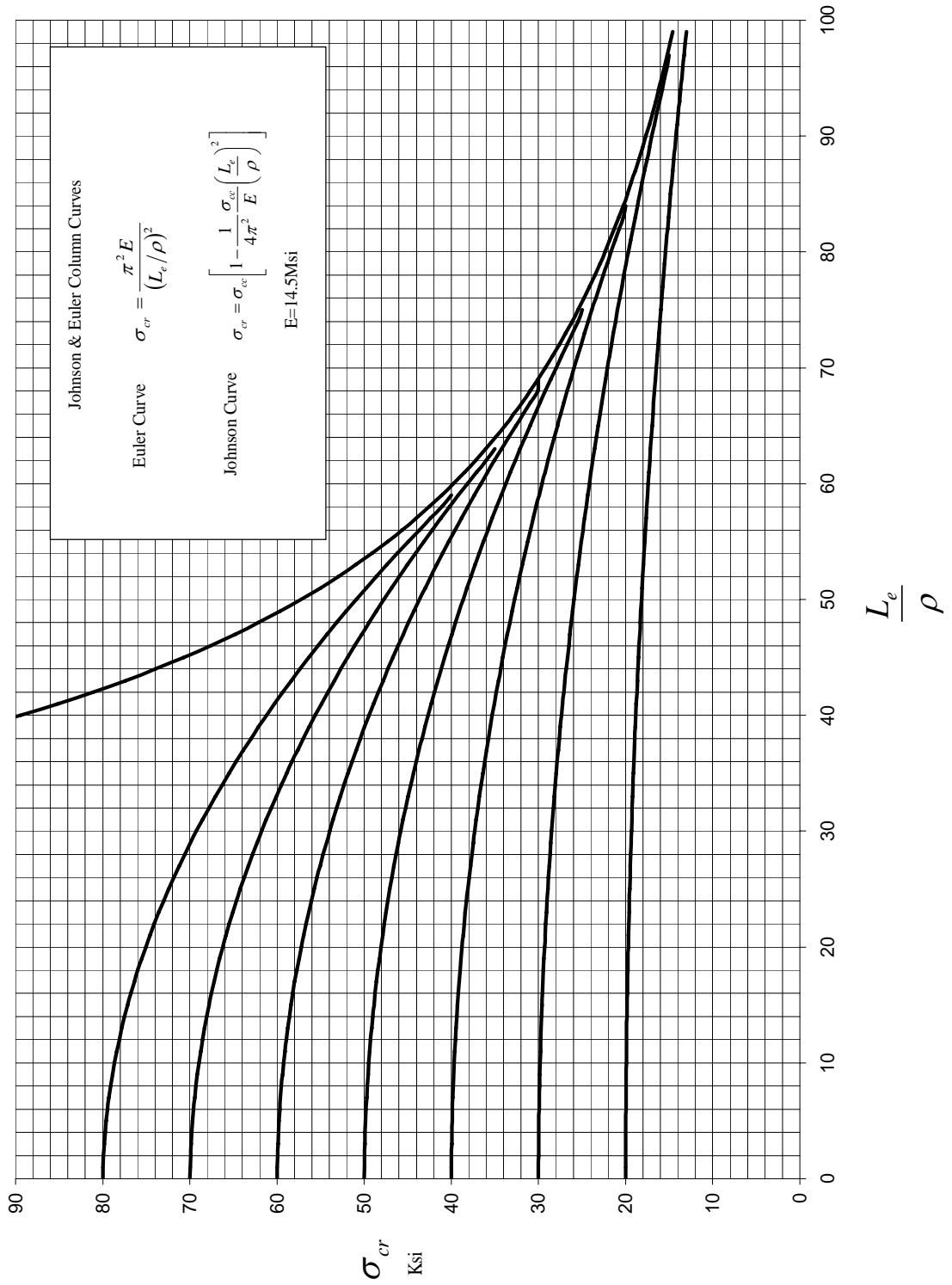


Figure B.4: Euler Column Buckling of CFRP Laminate Ex=14.5Msi

C Appendix

MIL-HDBK-5J
31 January 2003

Table 3.7.6.0(b). Design Mechanical and Physical Properties of 7075 Aluminum Alloy Sheet and Plate

Specification	AMS 4045 and AMS-QQ-A-250/12																	
	Sheet									Plate								
	T6 and T62 ^a									T651								
Form	0.008- 0.011	0.012- 0.039	0.040- 0.125	A	B	A	B	A	B	0.250- 0.499	0.500- 1.000	1.001- 2.000	2.001- 2.500	A	B	A	B	A
Temper	S	A	B	A	B	A	B	A	B	A	B	A	B	A	B	A	B	A
Thickness, in.
Basis
Mechanical Properties:																		
F_{up} , ksi:	...	76	78	78	80	78	80	77	79	77	79	76	78	75	77	71	73	66
L	...	74	76	78	80	78	80	77	80	78	80	77	79	76	78	72	74	72
LT	70 ^b	71 ^b	66 ^b	68 ^b	61 ^b
F_{cp} , ksi:	...	69	72	70	72	71	73	69	71	70	72	69	71	66	68	63	65	60
L	...	63	67	70	68	70	69	71	67	69	68	70	67	69	64	66	61	58
LT	59 ^b	61 ^b	56 ^b	58	52 ^b
F_{cp} , ksi:	...	68	71	69	71	70	72	67	69	68	70	66	68	62	64	58	60	55
L	...	71	74	72	74	73	75	71	73	72	74	71	73	68	70	65	67	61
LT	67	70	64	66	61
F_{up} , ksi:	...	46	47	47	48	47	48	43	44	44	45	44	45	44	43	42	43	39
F_{br} , ksi:	...	118	121	121	124	121	124	117	120	117	120	116	119	114	117	108	111	107
(e/D = 1.5)	...	152	156	156	160	156	160	145	148	145	148	143	147	141	145	134	137	132
F_{br} , ksi:	...	100	105	102	105	103	106	97	100	100	103	100	103	98	101	94	97	89
(e/D = 2.0)	...	117	122	119	122	121	124	114	118	117	120	117	120	113	117	109	112	104
e , percent (S-basis):	...	5	7	...	8	...	8	9	...	9	...	6	...	5	...	5	...	3
LT
E , 10 ³ ksi	...	10.3
E , 10 ³ ksi	...	10.5
G , 10 ³ ksi	...	3.9
μ	...	0.33
Physical Properties:																		
ω , lb/in. ³	...	0.101
C , K, and α	...	See Figure 3.7.6.0

a Design allowable values were based upon data obtained from testing T6 temper sheet and from testing samples of sheet, supplied in the O or F temper, which were heat treated to demonstrate response to heat treatment by suppliers. Properties obtained by the user may be lower than those listed if the material has been formed or otherwise cold worked, particularly in the annealed temper, prior to solution heat treatment.

b Caution: This specific alloy, temper, and product form exhibits poor stress-corrosion cracking resistance in this grain direction. It corresponds to an SCC resistance rating of D, as indicated in Table 3.1.2.3.1(a).

c Bearing values are "dry pin" values per Section 1.4.7.1. See Table 3.1.2.1.1.

Figure C.1: 7075 Aluminum Alloy Mechanical Properties (Ref 4)

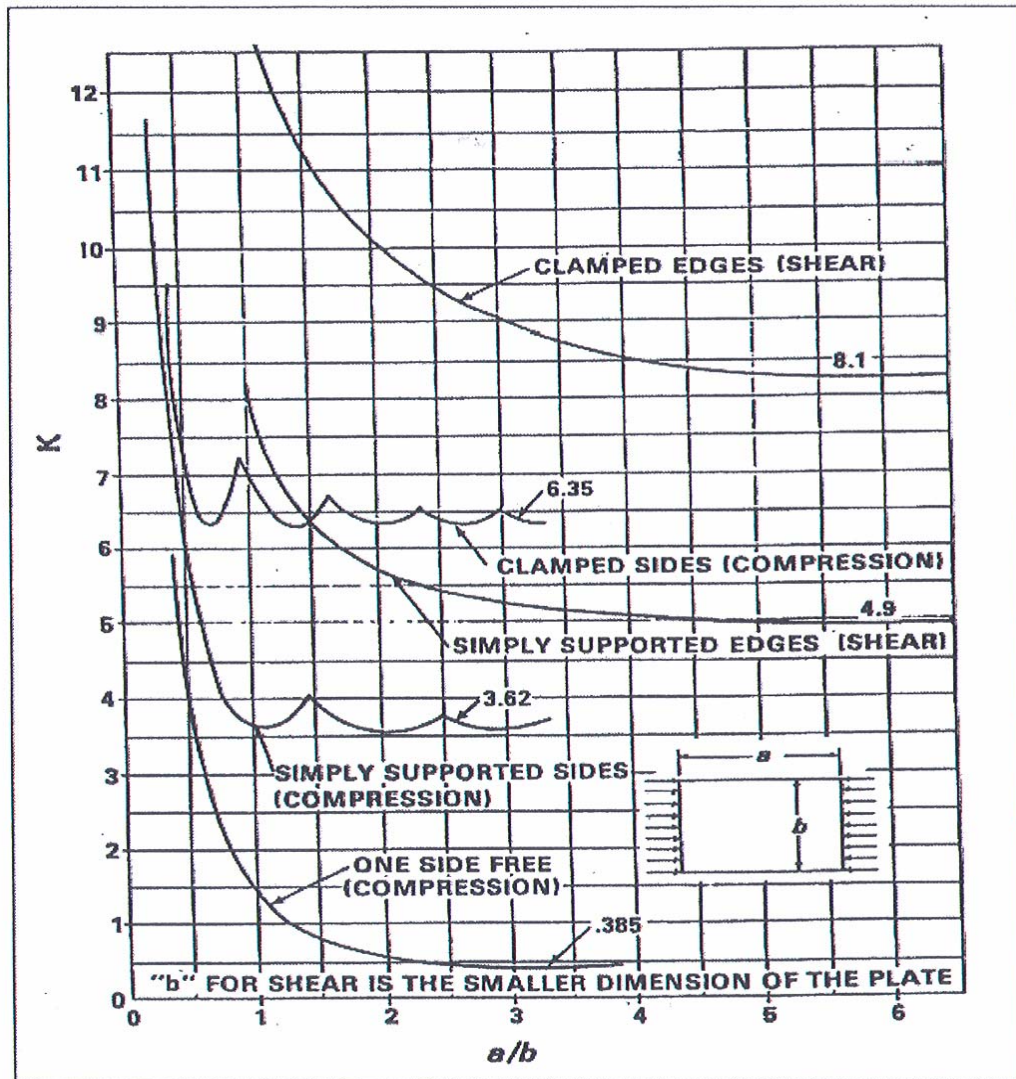


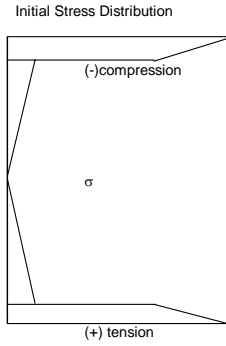
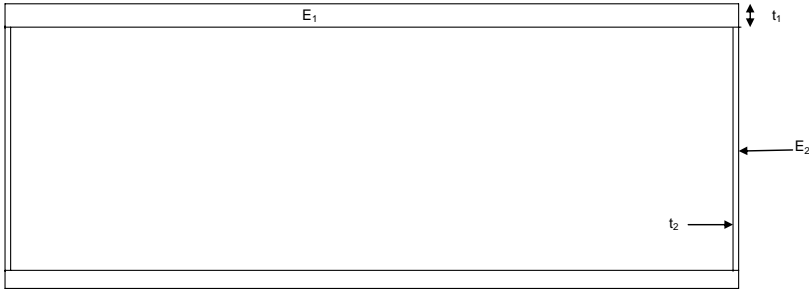
FIGURE 7.12 "K" Values for Compression and Shear Panel Buckling

Figure C.2: "K" Values for Compression and Shear Panel Buckling (Ref 7)

Example of Composite beam stress correction on Wing Box

Simplified Wing Box

(Reference 8)

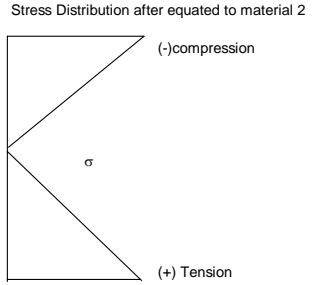
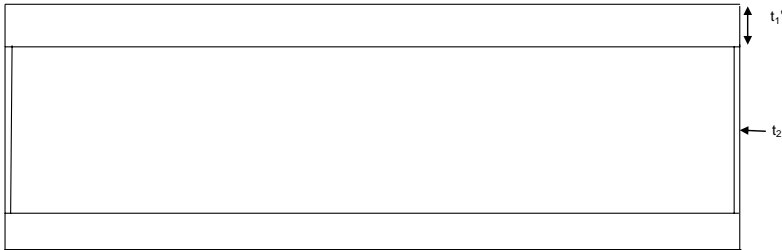


Where $E_1 > E_2$

$$n = \frac{E_1}{E_2}$$

$$t_1' = nt_1$$

Making the whole Wing box equivalent area with respect to material 2 $t_1 < t_1'$



Update centroid with new area distribution

$$\bar{y}' = \frac{\sum \tilde{y}A}{\sum A}$$

Update moment of inertial about the centroid

$$I' = \sum A'(y_i - y_c')^2$$

Update the axial stress on top skin (material 1)

$$\sigma'_x = \frac{-M(y_i - y_c')}{I_{xx}}$$

Apply transformation factor again to get actual stress in top skin (material 1)

$$\sigma_x = n\sigma'_x$$

σ_x in this example is the stress in the top skin

Figure C.3: Stiffness Correction

D Appendix

Sample Calculation

Sample Hand calculations are done to clarify the methodology used to size the fuselage structure. Fuselage section 46 is used to verify the optimization calculations. The sample hand calculations are done by treating the fuselage cross section as a thin walled tube.

Geometry and Area Distribution

Equivalent Skin Area

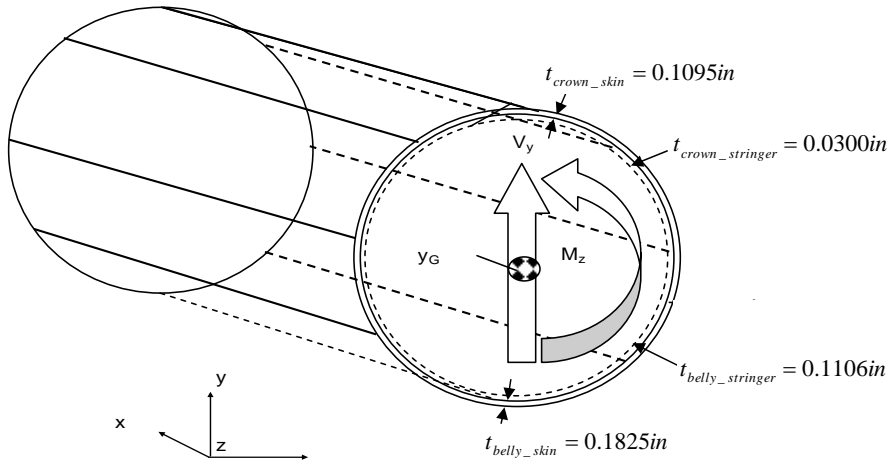


Figure D.1: Illustration of Fuselage Modeled as Idealized Tube

xt =					
0.0904	0.1049	0.1027	0.1095	0.0550	0.0550
0.0312	0.0540	0.0300	0.0300	0.0300	0.0300
0.0751	0.0885	0.1213	0.1825	0.0762	0.0597
0.0300	0.0300	0.0600	0.1106	0.0300	0.0300

Fuselage Section 46

Figure D.2: Optimized Thicknesses for Fuselage Section 46

An equivalent skin thickness is calculated to take into account the area of the stringers in addition to the skin area. Also, the equivalent skin thickness is calculated to use the equation for the center of mass, first, and the second moment of area that are derived from a thin walled tube. Figure 3.1 illustrates the fuselage analysis with the internal loads applied to a thin walled tube.

The stringer panel lengths b_i , are given in the calculations below. There are approximately 30 stringers on each the crown and belly of the fuselage of the wide body aircraft. The equivalent skin thickness is t'_{eq} . A is the calculated Area for the crown and belly of the fuselage separately.

Crown

$$b_{flange} = 0.5in$$

$$b_{web} = 1.25in$$

$$b_{cap} = 1.5in$$

$$A_{crown_stringers} = [2(0.5in) + 2(1.25in) + (1.5in)](0.03in)(30stringers) = 4.5in^2$$

$$t_{eq_crown_stringers} = \frac{4.5in^2}{\pi \frac{(19ft)(12in/ft)}{2}} = 0.01256in$$

$$t'_{eq_crown} = 0.1095in + 0.01256in = 0.1220in$$

$$A_{crown} = \pi \frac{19ft(12in/ft)}{2} (0.1220in) = 43.69in^2$$

Belly

$$A_{belly_stringers} = [2(0.5in) + 2(1.25in) + (1.5in)](0.1106in)(30stringers) = 16.59in^2$$

$$t_{eq_belly_stringers} = \frac{16.92in^2}{\pi \frac{(19ft)(12in/ft)}{2}} = 0.0463in$$

$$t'_{eq_belly} = 0.1825in + 0.0463in = 0.2288in$$

$$A_{belly} = \pi \frac{19ft(12in/ft)}{2} (0.2288in) = 81.94in^2$$

Center of Mass

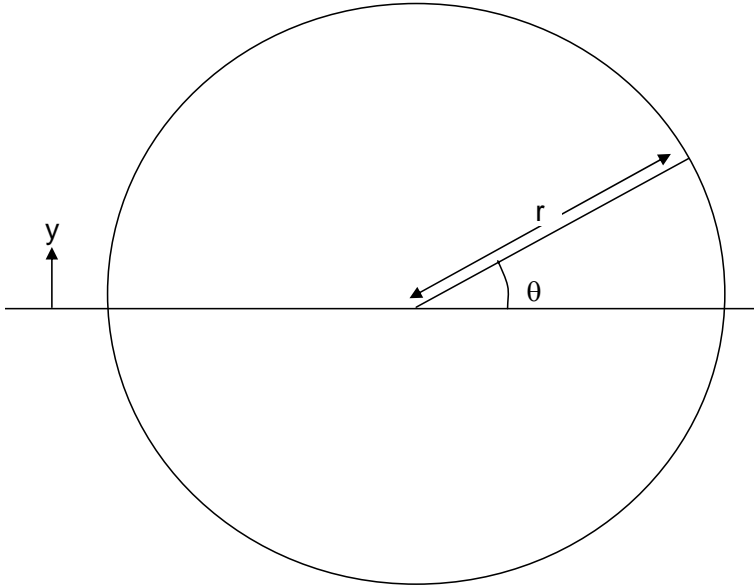


Figure D.3: Lateral Cut of Fuselage as a Idealized Tube

Below the first and second moment of area is derived assuming the area equation of a thin walled tube. The radius of a lateral cut of the fuselage is r , and is illustrated in Figure 3.3. θ is the angle from the center of the circle as illustrated in Figure 3.3. y

is the lateral distance from the center of the circle. The First Moment of Area (i.e.

$\int y dA$) is used to find the center of mass and the shear flow at the center of the

fuselage. The Moment of Inertia I_{zz} , is the Second Moment of Area (i.e. $\int y^2 dA$).

Figure 3.4 gives the center of mass given by the MATLAB code.

$$y_g = \frac{1}{A} \int y dA = \frac{\sum_{i=1}^{61} y_i a_i}{\sum_{i=1}^{61} a_i}$$

$$\int y dA = \int_0^{\pi} (r \sin \theta) (\pi r t) d\theta = r^2 t (1 - \cos \theta) \Big|_0^{\pi} = 2r^2 t$$

$$A_{half_tube} = \pi r t$$

$$y_{g_half_tube} = \frac{2r^2 t}{\pi r t} = \frac{2}{\pi} r = \frac{2}{\pi} \frac{(19 ft)(12 in/ft)}{2} = 72.57 in$$

$$y_g = \frac{A_{crown} y_{g_crown} + A_{belly} y_{g_belly}}{A_{crown} + A_{belly}} = \frac{(43.69 in^2 - 81.94 in^2)(72.57 in)}{43.69 in^2 + 81.94 in^2} = -22.09 in$$

```
yg =
-22.3896
```

Figure D.4: Center of Mass (in)

Second Moment of Area

The equation derived for the second moment of area assumes a thin walled tube of uniform thickness with its center of mass in the center of the circle. Since the actual center of mass is not in the center of the circle the equation for the second moment of

area needs to be uncoupled using the parallel axis theorem (i.e. $I_x + A(y - y_c)^2$).

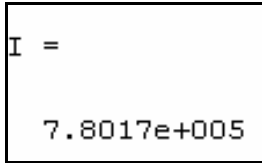
Figure 4.5 shows the second moment of area calculated by the MATLAB code.

$$I_{zz} = \int y^2 dA = \sum_{i=1}^{61} a_i (y_i - y_g)^2$$

$$\int y^2 dA = \int_0^{2\pi} (r \sin \theta)^2 r d\theta = \pi r^3 t = \frac{\pi D^3 t}{8}$$

$$I_{zz} = \frac{\pi D^3 \left(\frac{t'_{eq_crown} + t'_{eq_belly}}{2} \right)}{8} - \left(\frac{A_{crown} + A_{belly}}{2} \right) (0 - y_g)^2 =$$

$$\frac{\pi \left[(19 ft^3) \left(12 in / ft \right) \right]^3 \left(\frac{0.1220 in + 0.2288 in}{2} \right)}{8} - \left(\frac{43.69 in^2 + 81.94 in^2}{2} \right) (0 - 22.09)^2 = 785,731 in^4$$



```
I =  
  
7.8017e+005
```

Figure D.5: Second Moment of Area (in⁴)

Internal Loads

The optimized structure of fuselage section 46 is driven by load case 2 (-2g hard landing). The shear and moment values in fuselage section 46 are given below and are verified in the MATLAB code in Figure 3.6.

$$V_y = 5.92 \times 10^5 \text{ lbs}$$

$$M_z = -2.725 \times 10^8 \text{ lbs} \cdot \text{in}$$

v2 =						
	-182000	-142400	552600	592000	76200	36800
m2 =						
	68200000	112800000	-49648000	-272466000	-26000000	-10540000

Figure D.6: Internal Loads (shear(lbs), moment(lbs*in))

Internal Stress

Maximum Principle Stress in Fuselage Crown

The skin on the crown of fuselage section 46 is OHT critical, therefore the maximum principle stress in the crown of the fuselage is calculated below. It is assumed that the failure takes place at the top of the crown where the axial stress is the greatest. The top of the crown there is no shear stress so the max principle stress equals the axial stress and the minimum principle stress is the transverse tension stress from pressurization. Figure 3.7 shows the principle stresses given in the MATLAB code.

$$\sigma_{x_pressure} = \frac{Pr}{2t} = \frac{(18psi) \left(\frac{19ft \times 12in/ft}{2} \right)}{2(0.1095in)} = 9,370psi$$

$$\sigma_{y_pressure} = \frac{Pr}{t} = \frac{(18psi) \left(\frac{19ft \times 12in/ft}{2} \right)}{(0.1095in)} = 18,740psi$$

$$\sigma_{x_bending} = \frac{-M_z c}{I} = \frac{-(-2.725 \times 10^8 \text{ lb} \cdot \text{in}) \left(\frac{19 \text{ ft} \times 12 \text{ in/ft}}{2} - (-22.09 \text{ in}) \right)}{785,731 \text{ in}^4} = 47,197 \text{ psi}$$

$$\sigma_x = \sigma_{x_pressure} + \sigma_{x_bending} = 9,370 \text{ psi} + 47,197 \text{ psi} = 56,567 \text{ psi}$$

$$\sigma_y = \sigma_{y_pressure} = 18,740 \text{ psi}$$

$$\sigma_1 = \sigma_x = 56.57 \text{ ksi}$$

$$\sigma_2 = \sigma_y = 18.74 \text{ ksi}$$

```
>> max(s1_2)

ans =

σ1 → 5.7000e+004

>> max(s2_2)

ans =

σ2 → 1.8735e+004
```

Figure D.7: Maximum and Minimum Principle Stress in Crown (psi)

Minimum Principle Stress in Fuselage Belly

The minimum axial compression stress takes place at the very bottom of the belly of the fuselage. At the bottom of the fuselage there is no in-plane shear stress and pressure effects are not taken into account in the axial direction. Since there is no shear stress at the bottom of the fuselage the minimum principle stress is equal to the axial stress and the maximum principle stress is equal to the transverse tension stress

from pressurization. Figure 3.8 shows the minimum principle stress in the belly of fuselage section 46 calculated by the MATLAB code.

$$\sigma_x = \frac{-M_z c}{I} = \frac{-(-2.725 \times 10^8 \text{ lb} \cdot \text{in}) \left(\frac{19 \text{ ft} \times 12 \text{ in} / \text{ft}}{2} - (-22.09 \text{ in}) \right)}{785,731 \text{ in}^4} = -31,875 \text{ psi}$$

$$\sigma_1 = 18.74 \text{ ksi}$$

$$\sigma_2 = -31.88 \text{ ksi}$$

```
>> min(s2_2)

ans =

σ2 → -3.2000e+004
```

Figure D.8: Minimum Principle Stress in Belly (psi)

Maximum Shear Stress

There is no shear fracture or shear buckling failure in fuselage section 46 but the maximum shear stress is calculated for verification of the MATLAB code. The shear flow equation is divided by two (i.e. $\Delta q = V_y Q_z / 2I$) since there are two shear paths for a tube in pure bending. Also the very most top and bottom points of a tube have zero in-plane shear stress for a tube in pure bending. Similar to the second moment of area

the first moment of area needs to be uncoupled to account for a center of mass that is not located at the axis-symmetric center of the tube. This is shown in the calculation below. Figure 3.9 shows the max in-plane shear stress calculated in the MATLAB code. The max shear stress is located in the crown skin so the crown skin thickness

t_{crown_skin} , is used to calculate the maximum shear stress.

$$Q_x = \int_0^{\pi} y dA$$

$$Q_z = 2r^2(t'_{crown}) + A_{crown}(0 - y_g) =$$

$$2\left(\frac{19ft \times 12in/ft}{2}\right)^2 (0.1120in) + (43.69in^2)[0 - (-22.09)] = 4,136in^3$$

$$q = \frac{V_y Q_z}{2I_z} = \frac{(5.92 \times 10^5 lbs)(4,136in^3)}{(2)(785,731in^4)} = 1,558 \frac{lbs}{in}$$

$$\tau_{xy_max_crown} = \frac{q}{t_{crown_skin}} = \frac{1,558 \frac{lbs}{in}}{0.1095in} = 14,233psi$$

toux2 =						
1.0e+004 *						
Columns 1 through 7						
0.0520	0.1040	0.1556	0.2069	0.2575	0.3073	0.3561
Columns 8 through 14						
0.4039	0.4503	0.4953	0.5386	0.5802	0.6199	0.6575
Columns 15 through 21						
0.6929	0.7259	0.7565	0.7845	0.8099	0.8324	0.8521
Columns 22 through 28						
0.8688	0.8824	0.8929	0.9002	0.9042	0.9049	0.9024
Columns 29 through 35						
0.8964	0.8871	1.4669	1.4526	1.4353	1.4150	1.3917
Columns 36 through 42						
1.3655	1.3364	1.3045	1.2698	1.2323	1.1923	1.1496
Columns 43 through 49						
1.1045	1.0569	1.0071	0.9551	0.9010	0.8450	0.7871

Figure D.9: Max In-plane Shear Stress (psi)

Buckling Stability

Buckling Strength of Belly Stringers

Crippling

To evaluate the buckling stability of a hat stiffener the cross section is broken up into a series of flat plates as shown in Figure 3.10. The edges of the plates that do not deflect during local buckling are subtracted as shown in Figure 3.10. New panel widths b_1 , b_2 , and b_3 are calculated below to determine the crippling stress.

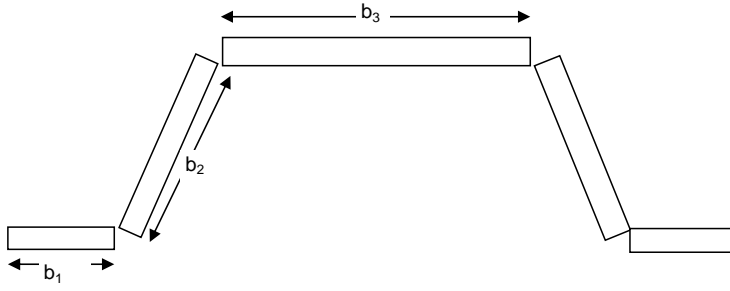


Figure D.10: Idealized Stringer Section

$$b_1 = b_f - t = 0.5in - 0.1106in = 0.3894in$$

$$b_2 = b_w - 2t = 1.25in - 2(0.1106in) = 1.0288in$$

$$b_3 = b_c - 2t = 1.5in - 2(0.1106in) = 1.2788in$$

The crippling stress is calculated for each of the hat stiffener panels. The flanges are evaluated as one edge free(OEF), and the webs and caps as no edge free(NEF)

condition. E_x and E_y are the in-plane and transverse Modulus of Elasticity

respectively. D_{11} is the in-plane flexural stiffness. \bar{E} is the Flexural Modulus of

Elasticity. $F_{cc}(= \sigma_{cc})$ is the crippling stress in the military handbook notation.

$F_{cu}(= \sigma_{cu})$ is the ultimate compression stress in military handbook notation. b is the width of the panel. t is the belly stringer thickness. The crippling stress of the hat section is a weighted average of the crippling stress of the individual panels. Figure 3.11 shows the crippling stress calculated by the MATLAB code.

$$\frac{F^{cc}}{F^{cu}} \frac{E_x}{\bar{E}} (OEF) = 0.5832 \left(\frac{b}{t} \frac{\bar{E}}{E_x} \sqrt{\frac{F_{cu}}{E_x E_y}} \right)^{-0.786}$$

$$\frac{F^{cc}}{F^{cu}} \frac{E_x}{\bar{E}} (NEF) = 0.9356 \left(\frac{b}{t} \frac{\bar{E}}{E_x} \sqrt{\frac{F_{cu}}{E_x E_y}} \right)^{-0.842}$$

where

$$\bar{E} = \frac{12(1 - \nu_{xy}^2) D_{11}}{t^3}$$

$$E_x = E_y = 8.6 \text{ msi}$$

$$F^{cu} = 70 \text{ ksi}$$

$$D_{11} = 0.09523 E_x t_{\text{stringer}}^3 + 52.12 = 0.09523 (8.6 \text{ msi}) (0.1106 \text{ in})^3 + 52.12 = 1160.11 \text{ lbs} \cdot \text{in}$$

$$\bar{E} = \frac{12(1 - 0.33^2) (1160.11 \text{ lbs} \cdot \text{in})}{(0.1106 \text{ in})^3} = 9.17 \text{ msi}$$

$$\left(\frac{F^{cc}}{F^{cu}} \right)_1 = 0.5832 \left(\frac{0.3894 \text{ in}}{0.1106 \text{ in}} \frac{9.17 \text{ msi}}{8.60 \text{ msi}} \sqrt{\frac{70 \times 10^3 \text{ psi}}{8.6 \times 10^6 \text{ psi}}} \right)^{-0.784} \left(\frac{9.17 \text{ msi}}{8.60 \text{ msi}} \right) = 1.45$$

$$\left(\frac{F^{cc}}{F^{cu}} \right)_2 = 0.9356 \left(\frac{1.0288 \text{ in}}{0.1106 \text{ in}} \frac{9.17 \text{ msi}}{8.60 \text{ msi}} \sqrt{\frac{70 \times 10^3 \text{ psi}}{8.6 \times 10^6 \text{ psi}}} \right)^{-0.842} \left(\frac{9.17 \text{ msi}}{8.60 \text{ msi}} \right) = 1.095$$

$$\left(\frac{F^{cc}}{F^{cu}} \right)_3 = 0.9356 \left(\frac{1.2788 \text{ in}}{0.1106 \text{ in}} \frac{9.17 \text{ msi}}{8.60 \text{ msi}} \sqrt{\frac{70 \times 10^3 \text{ psi}}{8.6 \times 10^6 \text{ psi}}} \right)^{-0.842} \left(\frac{9.17 \text{ msi}}{8.60 \text{ msi}} \right) = 0.912$$

$$\left(\frac{F^{cc}}{F^{cu}} \right)_{\text{Hat_Stiffener}} = \frac{2 \left[\left(\frac{F^{cc}}{F^{cu}} \right)_1 \right] b_1 + 2 \left[\left(\frac{F^{cc}}{F^{cu}} \right)_2 \right] b_2 + \left(\frac{F^{cc}}{F^{cu}} \right)_3 b_3}{2b_1 + 2b_2 + b_3}$$

$$= \frac{2(1.450)(0.3894 \text{ in}) + 2(1.095)(1.0288 \text{ in}) + (0.912)(1.2788 \text{ in})}{2(0.3894 \text{ in} + 1.0288 \text{ in}) + 1.2788 \text{ in}} = 1.105$$

$$\sigma_{cc} = F_{cc} = (1.105)(70 \text{ ksi}) = 77.37 \text{ ksi}$$

$$sccb =$$

$$\sigma_{cc} \rightarrow 7.7477e+004$$

Figure D.11: Crippling Stress of Belly Stringer

Local Center of Mass

Figure 3.12 shows the geometry of the hat stiffener. For this calculation y_i is the lateral position of the hat stiffeners individual panels center of mass. θ is the angle of the hat stiffeners webs. The hat stiffener is symmetric about its lateral center so the webs are both at the same angle. The hat stiffener center of mass is the weighted average of the individual panel's center of mass.

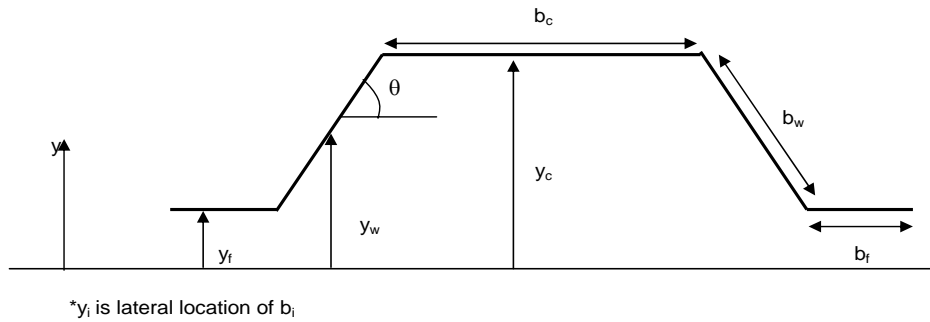


Figure D.12: Geometry of Hat Stiffener

$$y_f = 0$$

$$y_w = 0.5in$$

$$y_c = 1.0in$$

$$y_{G_hat} = \frac{2(0)(0.5in) + 2(0.5in)(1.25in) + (1.5in)(1.0in)}{2(0.5in + 1.25in) + 1.5in} = 0.55in$$

Local Second Moment of Area

The second moment of area is calculated below. It is calculated for each panel and then added together. Each panels second moment of area is the sum of their local second moment of area and the parallel axis theorem calculation with respect to the center of mass of the cross section. As in previous calculations the subscripts; f , w , and c stand for the flange, web, and cap respectively.

$$\begin{aligned} I_f &= 2 \left[\frac{1}{12} b_f t_{stringer}^3 + b_f t_{stringer} (y_f - y_{g_hat})^2 \right] = \\ &2 \left[\frac{1}{12} (0.5in)(0.1106in)^3 + (0.5in)(0.1106in)(0 - 0.55in)^2 \right] = 0.0336in^4 \\ I_w &= 2 \left[\frac{1}{24} b_w^3 t_{stringer} (1 - \cos(2\theta)) + b_w t_{stringer} (y_w - y_{g_hat})^2 \right] = \\ &2 \left[\frac{1}{24} (1.25in)^3 (0.1106in)(1 - \cos(2 \times 53^\circ)) + (1.25in)(0.1106in)(0.5in - 0.55in)^2 \right] = 0.0237in^4 \\ I_c &= \frac{1}{12} b_c t_{stringer}^3 + b_c t_{stringer} (y_c - y_{g_hat})^2 = \\ &\frac{1}{12} (1.5in)(0.1106in)^3 + (1.5in)(0.1106in)(1.0in - 0.55in)^2 = 0.0338in^4 \\ I_{hat} &= I_f + I_w + I_c = 0.0336in + 0.0237in + 0.0338in = 0.0911in^4 \end{aligned}$$

Area

$$A_{hat} = [2(b_f + b_w) + b_c] t_{stringer} = [2(0.5in + 1.25in) + 1.5in](0.1106in) = 0.553in^2$$

Radius of Gyration

$$\rho = \sqrt{\frac{I}{A}} = \sqrt{\frac{0.0911in^4}{0.5530in^2}} = 0.4058in$$

Effective Length

$$L = 20in$$

$$c = 1.5$$

$$L_e = \frac{L}{\sqrt{c}} = \frac{20in}{\sqrt{1.5}} = 16.33in$$

Actual and Critical Slenderness Ratio

$$\frac{L_e}{\rho} = \frac{16.33in}{0.4058in} = 40.24$$

$$\left(\frac{L_e}{\rho}\right)_{crit} = \pi \sqrt{\frac{2}{\sigma_{cc}/E_x}} = \pi \sqrt{\frac{2}{77.37 \times 10^3 psi / 8.60 \times 10^6 psi}} = 46.84$$

Since the critical slenderness ratio is larger than that of the stringer, the stringer will buckle in-elastically.

Stringer Buckling Strength

$$\begin{aligned}\sigma_{cr} &= \sigma_{cc} \left[1 - \frac{1}{4\pi^2} \frac{\sigma_{cc}}{E_x} \left(\frac{L_e}{\rho} \right)^2 \right] = 77.37ksi \left[1 - \frac{1}{4\pi^2} \frac{77.37 \times 10^3 psi}{8.60 \times 10^6 psi} \left(\frac{16.33in}{0.4058in} \right)^2 \right] \\ &= 48.81ksi\end{aligned}$$

Effective Width

The belly skin thickness t_{skin} is used to calculate the effective width of the belly stringers. The safety factor $S.F. = 1.5$ is used because the skin buckles at limit load.

$$w_e = (0.85)t_{skin} \frac{E_{x_skin}}{\sqrt{E_{x_stringer}}} \sqrt{\frac{1.5}{\sigma_{stiff}}} = (0.85)t_{skin} \sqrt{\frac{(1.5)E_x}{\sigma_{cr}}} = (0.85)(0.1858in) \sqrt{\frac{(1.5)8.60 \times 10^6 psi}{49.05 \times 10^3 psi}}$$

$$= 2.52in$$

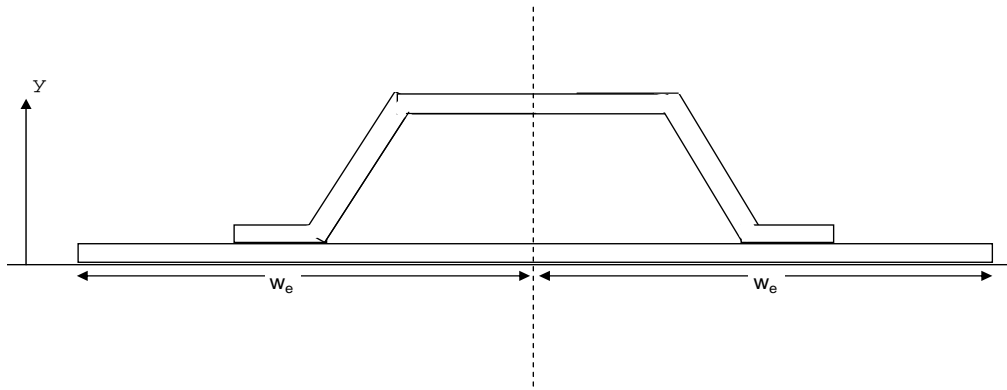


Figure D.13: Hat Stiffener Including Effective Width

Local Center of Mass Including Effective Width

$$y_{we} = 0$$

$$y'_{g_hat} = y_{g_hat} + \frac{t_{skin}}{2} = 0.55in + \frac{0.1825in}{2} = 0.6413in$$

$$y'_g = \frac{A_{hat} y'_{g_hat} + 2w_e t_{skin} y_{we}}{A_{hat} + 2w_e t_{skin}} = \frac{(0.5530in^2)(0.6413in) + 0}{0.5530in^2 + 2(2.520in)(0.1825in)} = 0.2408in$$

Local Second Moment of Area Including Effective Width

The subscript we , represent the second moment of area of the effective width of the skin.

$$\begin{aligned}
 I_{we} &= \frac{1}{12}(2)w_e t_{skin}^3 + 2w_e t_{skin} (y_{we} - y'_g)^2 \\
 &= \frac{2}{12}(2.520in)(0.1825in)^3 + 2(2.520in)(0.1825in)(0 - 0.2408in)^2 = 0.0559in^4 \\
 I'_{hat} &= I_{hat} + A_{hat} (y'_{g_hat} - y'_g)^2 = 0.0911in^4 + (0.5530in^2)(0.6413in - 0.2408in)^2 = 0.1798in^4 \\
 I' &= I'_{hat} + I_{we} = 0.0559in^4 + 0.1798in^4 = 0.2357in^4
 \end{aligned}$$

Area Including Effective Width

$$A' = A_{hat} + 2w_e t_{skin} = 0.5530in^2 + 2(2.520in)(0.1825in) = 1.4728in^2$$

Radius of Gyration Including Effective Width

$$\rho' = \sqrt{\frac{I}{A}} = \sqrt{\frac{0.2357in^4}{1.4728in^2}} = 0.40in$$

Buckling Strength Including Effective Width

$$\begin{aligned}
 \sigma_{cr} &= \sigma_{cc} \left[1 - \frac{1}{4\pi^2} \frac{\sigma_{cc}}{E_x} \left(\frac{L_e}{\rho} \right)^2 \right] = 77.37ksi \left[1 - \frac{1}{4\pi^2} \frac{77.37 \times 10^3 psi}{8.60 \times 10^6 psi} \left(\frac{16.330in}{0.400in} \right)^2 \right] = \\
 &= 47.98ksi
 \end{aligned}$$

$f_{crlb} =$ $\sigma_{cr} \longrightarrow 4.7991e+004$
--

Figure D.14: Belly Stringer Buckling Strength

Margins of Safety

Crown skin failure in OHT fracture at limit load

The OHT strength is $\sigma_{OHT} = 57ksi$.

$$M.S._{OHT} = \frac{\sigma_{OHT}}{\sigma_1} - 1 = \frac{57.00ksi}{56.57ksi} - 1 = 0.0076 \approx 0$$

Belly skin failure in OHC fracture at limit load

The OHC strength is $\sigma_{OHC} = 32ksi$.

$$M.S._{OHC} = \frac{\sigma_{OHC}}{\sigma_2} - 1 = \frac{32.00ksi}{31.88ksi} - 1 = 0.0038 \approx 0$$

Belly stringer failure in buckling at ultimate load

$$M.S._{Beam_Buckling} = \frac{\sigma_{cr}}{(1.5)\sigma_x} - 1 = \frac{47.98ksi}{(1.5)(31.88ksi)} - 1 = 0.0031 \approx 0$$

The method used for sample calculations is accurate enough to show the critical margins of safety are approximately zero. Therefore the MATLAB optimization has been verified with the sample calculations. Figure 3.15 verifies that the crown and belly skin are fracture critical, the crown stringers are not critical and are limited by minimum gauge, and the belly stringer are buckling failure critical. The fracture margin of safety equations are given in appendix B.

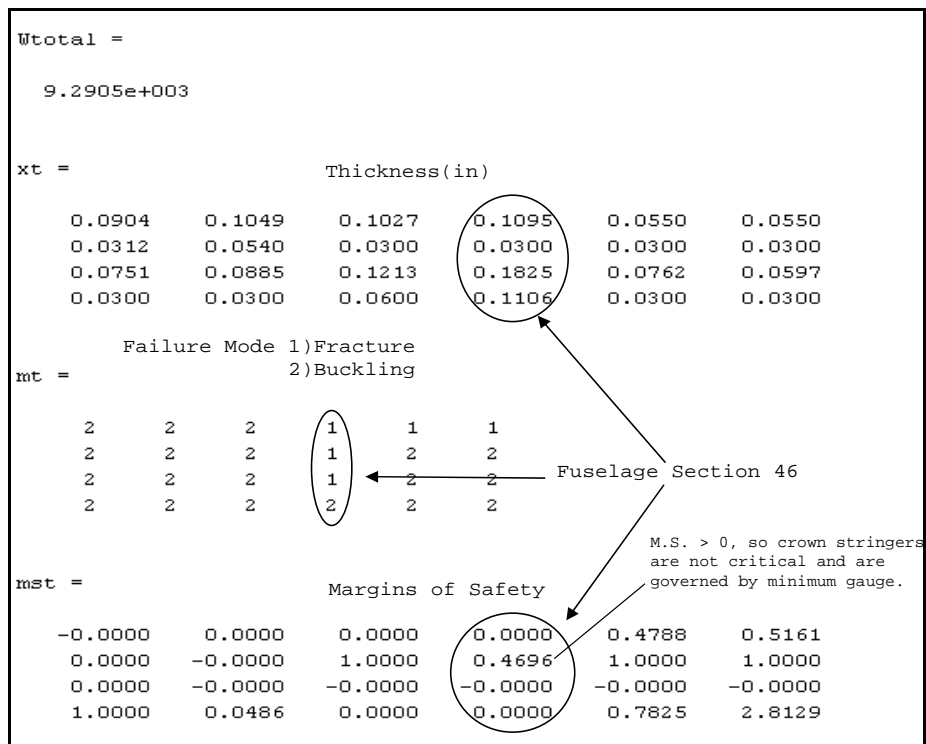


Figure D.15: Output for WB CFRP Baseline

$$\sigma_{cr} = K_c E \left(\frac{t}{b} \right)^2 \rightarrow N_{x_{cr}} = K_c E \frac{t^3}{b^2}$$

$$\tau_{cr} = K_s E \left(\frac{t}{b} \right)^2 \rightarrow N_{x_{cr}} = K_s E \frac{t^3}{b^2}$$

$$t_{skin} = \left(\frac{N_x \bar{w}}{K_c E} \right)^{\frac{1}{3}}$$

$$t_{skin} = \left(\frac{N_{xy} \bar{h}}{K_s E} \right)^{\frac{1}{3}}$$

Fuselage

Axial load from bending only

Un_pressurized

$$\sigma_{cr} = C_b E \frac{t}{r} = C_b E \frac{2t}{D}$$

$$N_{cr} = C_b E \frac{2t^2}{D}$$

$$t = \sqrt{\frac{N_x D}{2C_b E}}$$

Sensitivity Criteria

$$M.S. = \frac{\sigma_A}{\sigma_D} - 1 = 0 \rightarrow \sigma_A = \sigma_D$$

$$\sigma_D = \frac{N_x}{t}$$

$$\frac{\partial \sigma_D}{\partial t} = -\frac{N_x}{t^2}$$

$$\sigma_A = KE \left(\frac{t}{b} \right)^2 = CEt^2 \rightarrow E = \frac{\sigma_A}{Ct^2}$$

$$\frac{\partial E}{\partial t} = -2 \frac{\sigma_A}{Ct^3} = -2 \frac{N_x}{Ct^4} = \frac{2}{Ct^2} \left(\frac{\partial \sigma_D}{\partial t} \right)$$

$$C = \frac{K}{b^2}$$

$$\frac{\partial E}{\partial t} = \frac{2b^2}{Kt^2} \left(\frac{\partial \sigma_D}{\partial t} \right)$$

$$\frac{\partial E / \partial t}{\partial \sigma / \partial t} = \frac{\Delta E}{\Delta \sigma} = \frac{2}{K} \left(\frac{b}{t} \right)^2$$

Un-Stiffened Configuration Weights

WB CFRP

W.S. (%)	N _x LC1 (lb/in)	N _x LC2 (lb/in)	N _{xy} LC1 (lb/in)	t _{top_skin}	t _{bottom_skin}	t _{web}	Weight (lb)
0%	20.3	8.12	3.8	2.80	2.07	0.72	6262
11%	20.7	8.28	3.8	2.65	1.95	0.65	4804
21%	20.9	8.36	3.9	2.49	1.84	0.59	5976
37%	20.6	8.24	4.2	2.22	1.63	0.48	1726
43%	19.9	7.96	4.1	2.10	1.55	0.47	3726
58%	16.2	6.48	3.8	1.71	1.26	0.36	2216
74%	9.4	3.76	2.7	1.18	0.87	0.27	967
90%	1.9	0.76	1.0	0.54	0.40	0.15	329
Total Weight (lb)							52,011

WB Aluminum

W.S. (%)	N _x LC1 (lb/in)	N _x LC2 (lb/in)	N _{xy} LC1 (lb/in)	t _{top_skin}	t _{bottom_skin}	t _{web}	Weight (lb)
0%	19.46	7.79	3.8	3.06	2.25	0.59	12034
11%	19.97	7.99	3.9	2.89	2.13	0.53	9265
21%	20.28	8.11	3.9	2.73	2.01	0.48	11560
37%	20.05	8.02	4.2	2.43	1.79	0.40	3345
43%	19.43	7.77	4.1	2.30	1.70	0.38	7238
58%	15.92	6.37	3.8	1.88	1.38	0.30	4314
74%	9.26	3.71	2.7	1.30	0.96	0.22	1870
90%	1.76	0.71	1.0	0.58	0.43	0.12	628
Total Weight (lb)							100,509

NB CFRP

W.S. (%)	N _x LC1 (lb/in)	N _x LC2 (lb/in)	N _{xy} LC1 (lb/in)	t _{top_skin}	t _{bottom_skin}	t _{web}	Weight (lb)
0%	8.32	3.33	1.5	1.57	1.15	0.40	1498
11%	8.48	3.39	1.6	1.48	1.09	0.36	1154
21%	8.57	3.43	1.6	1.40	1.03	0.33	1441
37%	8.44	3.38	1.7	1.24	0.92	0.28	417
43%	8.16	3.26	1.7	1.18	0.87	0.26	897
58%	6.64	2.66	1.5	0.95	0.70	0.21	536
74%	3.85	1.54	1.1	0.66	0.49	0.15	235
90%	0.78	0.31	0.4	0.30	0.22	0.09	80
Total Weight (lb)							12,515

NB Aluminum

W.S. (%)	N _x LC1 (lb/in)	N _x LC2 (lb/in)	N _{xy} LC1 (lb/in)	t _{top_skin}	t _{bottom_skin}	t _{web}	Weight (lb)
0%	7.98	3.19	1.6	1.71	1.26	0.33	2879
11%	8.19	3.27	1.6	1.62	1.19	0.30	2226
21%	8.31	3.32	1.6	1.53	1.13	0.27	2786
37%	8.22	3.29	1.7	1.36	1.01	0.23	808
43%	7.96	3.19	1.7	1.29	0.95	0.21	1742
58%	6.52	2.61	1.5	1.05	0.77	0.17	1042
74%	3.80	1.52	1.1	0.73	0.54	0.12	454
90%	0.72	0.29	0.4	0.33	0.24	0.07	152
Total Weight (lb)							24,178

WB CFRP

F.S. (%)	N _x LC1 (lb/in)	N _x LC2 (lb/in)	(r/t) _{est}	C _b	t _{avg}	Weight (lb)
25%	741	-2694	268	0.18	0.426	4607
37%	1641	-3787	226	0.18	0.505	5138
52%	3323	1177	248	0.19	0.461	6479
70%	2059	6615	184	0.21	0.618	6856
83%	791	635	466	0.16	0.245	2251
100%	320	258	685	0.14	0.166	1279
Total Weight (lb)						26,610

WB AI

F.S. (%)	N _x LC1 (lb/in)	N _x LC2 (lb/in)	(r/t) _{est}	C _b	t _{avg}	Weight (lb)
25%	741	-2694	285	0.18	0.399	7711
37%	1641	-3787	254	0.20	0.449	8360
52%	3323	1177	264	0.19	0.432	10553
70%	2059	6615	192	0.20	0.594	11678
83%	791	635	497	0.16	0.230	3768
100%	320	258	731	0.14	0.156	2140
Total Weight (lb)						44,210

NB CFRP

F.S. (%)	N _x LC1 (lb/in)	N _x LC2 (lb/in)	(r/t) _{est}	C _b	t _{avg}	Weight (lb)
25%	432	-1675	245	0.20	0.319	1311
37%	957	-2312	208	0.20	0.374	1455
52%	1938	687	228	0.20	0.343	1831
70%	1201	3858	161	0.20	0.484	2011
83%	461	370	430	0.17	0.181	625
100%	186	150	657	0.16	0.119	347
Total Weight (lb)						7,580

NB AI

F.S. (%)	N _x LC1 (lb/in)	N _x LC2 (lb/in)	(r/t) _{est}	C _b	t _{avg}	Weight (lb)
25%	432	-1675	252	0.19	0.309	2273
37%	957	-2312	220	0.20	0.354	2488
52%	1938	687	240	0.20	0.324	3094
70%	1201	3858	175	0.21	0.447	3338
83%	461	370	455	0.17	0.172	1070
100%	186	150	672	0.15	0.116	606
Total Weight (lb)						12,868